

Multiwavelength Analysis of Six Luminous, Fast Blue Optical Transients

CASSIE SEVILLA ,¹ ANNA Y. Q. HO ,¹ NAYANA A.J. ,^{2,3} STEVE SCHULZE ,⁴ DANIEL A. PERLEY ,⁵
 MICHAEL BREMER,⁶ IGOR ANDREONI ,⁷ IVAN ALTUNIN,⁸ THOMAS G. BRINK ,² POONAM CHANDRA ,⁹
 PING CHEN ,^{10,11,12} ASHLEY A. CHRIMES ,^{13,14} MICHAEL W. COUGHLIN ,¹⁵ KAUSTAV K. DAS ,¹⁶ ANDREW DRAKE,¹⁶
 ALEXEI V. FILIPPENKO ,² CHRISTOFFER FREMLING ,^{17,18} JAMES FREEBURN ,^{19,20,7} AVISHAY GAL YAM ,¹²
 MARY GERHART ,² MATTHEW J. GRAHAM ,¹⁸ GEORGE HELOU ,¹⁸ K-RYAN HINDS ,⁵ NATALYA JOHNSON ,²¹
 MANSI M. KASLIWAL ,¹⁸ HARSH KUMAR ,^{22,23} RUSS R. LAHER ,²⁴ NATALIE LEBARON ,^{2,3} MAGGIE L. LI ,¹⁶
 CHANG LIU ,^{25,4,26} BEN MARGALIT ,¹⁵ YU-JING QIN ,¹ NABEEL REHEMTULLA ,^{25,4,26} SOPHIA RISIN ,²
 SAM ROSE ,¹⁸ RUPAK ROY,²⁷ BEN RUSHOLME ,²⁴ GENEVIEVE SCHROEDER ,¹ JESPER SOLLERMAN ,²⁸
 KAILAI WANG ,¹ JACOB L. WISE ,⁵ YI YANG ,^{2,29} YUHAN YAO ,^{30,2} AND WEIKANG ZHENG ,²

¹Department of Astronomy, Cornell University, Ithaca, NY 14853, USA

²Department of Astronomy, University of California, Berkeley, CA 94720-3411, USA

³Berkeley Center for Multi-messenger Research on Astrophysical Transients and Outreach (Multi-RAPTOR), University of California, Berkeley, CA 94720-3411, USA

⁴Center for Interdisciplinary Exploration and Research in Astrophysics (CIERA), Northwestern University, 1800 Sherman Ave, Evanston, IL 60201, USA

⁵Astrophysics Research Institute, Liverpool John Moores University, IC2, Liverpool Science Park, 146 Brownlow Hill, Liverpool L3 5RF, UK

⁶Institut de Radio Astronomie Millimétrique (IRAM), 300 rue de la Piscine, 38406 Saint Martin d'Hères, France

⁷Department of Physics and Astronomy, University of North Carolina at Chapel Hill, Chapel Hill, NC 27599-3255, USA

⁸Department of Physics, University of Nevada, Reno NV 89557, USA

⁹National Radio Astronomy Observatory, 520 Edgemont Road, Charlottesville, VA 22903-2475, USA

¹⁰Institute for Advanced Study in Physics, Zhejiang University, Hangzhou 310027, China

¹¹Institute for Astronomy, School of Physics, Zhejiang University, Hangzhou 310027, China

¹²Department of Particle Physics and Astrophysics, Weizmann Institute of Science, 234 Herzl St, 7610001 Rehovot, Israel

¹³European Space Agency (ESA), European Space Research and Technology Centre (ESTEC), Keplerlaan 1, 2201 AZ Noordwijk, the Netherlands

¹⁴Department of Astrophysics/IMAPP, Radboud University, PO Box 9010, 6500 GL Nijmegen, The Netherlands

¹⁵School of Physics and Astronomy, University of Minnesota, Minneapolis, MN 55455, USA

¹⁶Cahill Center for Astrophysics, California Institute of Technology, MC 249-17, 1200 E California Boulevard, Pasadena, CA, 91125, USA

¹⁷Caltech Optical Observatories, California Institute of Technology, Pasadena, CA 91125, USA

¹⁸Division of Physics, Mathematics and Astronomy, California Institute of Technology, Pasadena, CA 91125, USA

¹⁹Centre for Astrophysics and Supercomputing, Swinburne University of Technology, Victoria 3122, Australia

²⁰ARC Centre of Excellence for Gravitational Wave Discovery (OzGrav), Victoria 3122, Australia

²¹Department of Physics, Drexel University, Philadelphia, PA 19104, USA

²²Center for Astrophysics | Harvard & Smithsonian, 60 Garden Street, Cambridge, MA 02138-1516, USA

²³The NSF AI Institute for Artificial Intelligence and Fundamental Interactions, USA

²⁴IPAC, California Institute of Technology, 1200 E. California Blvd, Pasadena, CA 91125, USA

²⁵Department of Physics and Astronomy, Northwestern University, 2145 Sheridan Rd, Evanston, IL 60208, USA

²⁶NSF-Simons AI Institute for the Sky (SkAI), 172 E. Chestnut St., Chicago, IL 60611, USA

²⁷Institute of Astronomy Space and Earth Science (IASES), P 177, CIT Road, Scheme 7m, Kolkata-700054, West Bengal, India

²⁸The Oskar Klein Centre, Department of Astronomy, AlbaNova, Stockholm University, SE-106 91 Stockholm, Sweden

²⁹Department of Physics, Tsinghua University, Qinghua Yuan, Beijing 100084, China.

³⁰Miller Institute for Basic Research in Science, 206B Stanley Hall, Berkeley, CA 94720, USA

ABSTRACT

We present multiwavelength observations and analysis of six luminous fast blue optical transients (LFBOTs) discovered in Zwicky Transient Facility (ZTF) survey data. We identified these LFBOTs from their fast light-curve evolution ($t_{1/2} \leq 12$ d), blue colors at peak brightness ($g - r \leq -0.5$ mag), a visible host galaxy, high optical luminosity ($M_g < -20$), and an X-ray or radio detection. With the exception of AT2024aehp (ZTF24abygbss), these transients exhibit peaks in their 10 GHz radio light

curves at $t_{\text{rest}} \approx 50\text{--}100$ d, with peak radio luminosities ranging from $10^{38}\text{--}10^{40}$ erg s $^{-1}$. Modeling the radio emission as synchrotron radiation indicates a fast ($v = 0.1\text{--}0.3c$) shock in a dense ($n_e \approx 10^3\text{--}10^4$ cm $^{-3}$) medium. The X-ray emission varies by ≈ 2 orders of magnitude in luminosity ($10^{42}\text{--}10^{44}$ erg s $^{-1}$) at $t_{\text{rest}} \sim 20$ d. Analysis of the host-galaxy photometry and spectroscopy for each transient shows that they are predominantly nonnuclear (a few kpc offset) with star-forming host galaxies of stellar masses $10^9\text{--}10^{11} M_\odot$. Unlike all other LFBOTs to date, AT2024aehp exhibited a luminous ($M < -19$ mag) plateau in the optical light curve; spectra during this plateau phase showed a featureless blue continuum. The 6–15 GHz radio emission of AT2024aehp brightened by over an order of magnitude from $t_{\text{rest}} \approx 70$ d to $t_{\text{rest}} \approx 130$ d. The mostly consistent radio behavior between optically selected LFBOTs implies a similar circumburst medium, leading us to prefer a progenitor scenario in which mass is lost in a consistent way shortly prior to the terminal event, such as a massive star merging with a compact object.

1. INTRODUCTION

The advent of high-cadence optical surveys such as the Asteroid Terrestrial-impact Last Alert System (ATLAS; Tonry et al. 2018) and the Zwicky Transient Facility (ZTF; Bellm et al. 2019, Graham et al. 2019, Dekany et al. 2020) has led to the discovery of new classes of extragalactic transients. Some transients are referred to as fast blue optical transients (FBOTs), most famously AT2018cow (e.g., Prentice et al. 2018). FBOTs are typically defined as transients with blue colors ($g-r \leq -0.2$ mag), rapid time evolution (< 12 days above half-maximum brightness), and extragalactic nature (Drout et al. 2014; Pursiainen et al. 2018; Inserra 2019).

In this paper, we focus on a particular class of FBOT with luminous X-ray and/or radio emission, dubbed “AT2018cow-like” transients (Ho et al. 2023b) or “luminous fast blue optical transients” (LFBOTs; Metzger 2022; Klencki & Metzger 2025). There are currently eight published transients that fall under this classification (Table 1). It is theorized that the peak of their optical light curves results from shock breakout from a dense medium (Ofek et al. 2010; Pursiainen et al. 2018) or from a jet cocoon (Gottlieb et al. 2022). The radio emission is found to be consistent with synchrotron radiation emanating from the mildly relativistic shock (Margutti et al. 2019; Coppejans et al. 2020; Ho et al. 2020a). The X-ray radiation is suggested to come from a central X-ray source, separate from the synchrotron radiation that powers the radio (Margutti et al. 2019; Ho et al. 2019). For objects with high-cadence X-ray observations (AT2018cow, AT2020mrf, AT2022tsd, and AT2024wpp) it was found that the X-rays had fast variability on a timescale of minutes to days (Rivera Sandoval et al. 2018; Margutti et al. 2019; Yao et al. 2022; Ho et al. 2023c; Nayana et al. 2025; Perley et al. 2026).

Based on the first few LFBOTs discovered, Metzger (2022) argued that progenitor models must reconcile two key characteristics: a dense surrounding medium inferred from the synchrotron radiation, and a long-lived

central engine (accreting compact object) inferred from nonthermal variable X-ray emission as well as minutes-duration optical flares (Ho et al. 2023c). Some propositions include tidal disruption events (TDEs) involving an intermediate-mass black hole (Perley et al. 2019; Kuin et al. 2019; Gutiérrez et al. 2024), the direct collapse (failed explosion) of a supergiant star (Margutti et al. 2019; Perley et al. 2019; Chrimes et al. 2025), and the tidal disruption of a star by a stellar-mass black hole resulting from a merger (Metzger 2022; Klencki & Metzger 2025) or random interactions in a cluster (Kremer et al. 2021, 2023).

To determine the progenitors of LFBOTs, it is necessary to increase the number of AT2018cow-like objects with multiwavelength observations. Unfortunately, the rarity of these transients and the recency of the development of optical surveys like ZTF has limited the discovery rate. It is not enough to detect a candidate LFBOT in a high-cadence optical survey. Confirming an FBOT to be similar to AT2018cow requires broad multiwavelength follow-up campaigns that can extend up to years past their initial discovery. In this paper, we present five more LFBOTs with multiwavelength follow-up observations, as well as further radio observations on a sixth (AT2023fh), increasing the sample size by over 50%.

This paper presents optical photometry, optical spectroscopy, and observations at X-ray, radio, and millimeter wavelengths. Section 2 describes the observations and data reduction. In Section 3 we compare the data to previous LFBOTs and other extragalactic transients. In Section 4 we model the radio emission and analyze the host-galaxy properties. In Section 5 we present our conclusions.

Throughout this paper, we assume a flat Λ CDM cosmology with $H_0 = 67.4$ km s $^{-1}$ Mpc $^{-1}$ and $\Omega_m = 0.315$ (Planck Collaboration et al. 2020). All usages of t_{obs} refer to the time after the optical light curve peak in the observer frame, while t_{rest} refers to this time in the rest

frame. All dates are in UTC and all magnitudes are in AB.

2. OBSERVATIONS

The basic characteristics for all LFBOTs are listed in Table 1. The discovery details for AT2022abfc, AT2023fhn, AT2023hkw, AT2023vth, AT2024qfm, and AT2024aehp are given in Appendix A. Here we provide details on our multiwavelength follow-up observations.

2.1. Optical Photometry

After each LFBOT was identified in ZTF photometry (outlined in Appendix A), we obtained follow-up optical photometry using the Liverpool Telescope (LT; Steele et al. 2004) and the SED Machine (SEDM; Blagorodnova et al. 2018; Rigault et al. 2019; Kim et al. 2022) on the Palomar 60-inch (1.5 m) telescope (P60; Cenko et al. 2006). For AT2024aehp, we also have ultraviolet (UV) data from the *Neil Gehrels Swift Observatory* (*Swift*; Gehrels et al. 2004) Ultraviolet/Optical Telescope (Roming et al. 2005). For AT2024qfm, we also present photometry from the Alhambra Faint Object Spectrograph and Camera (ALFOSC) on the 2.56 m Nordic Optical Telescope (NOT; Djupvik & Andersen 2010), the Inamori-Magellan Areal Camera & Spectrograph (IMACS; Dressler 2010) mounted on the 6.5 m Magellan-Baade telescope, the Large Monolithic Imager (LMI) on the 4.3 m Lowell Discovery Telescope (LDT; Bida et al. 2014), and the Goodman High Throughput Spectrograph (GHTS; Clemens et al. 2004) camera on the 4.1 m Southern Astrophysical Research (SOAR) Telescope¹. We correct for Milky Way extinction using the prescription of Schlafly & Finkbeiner (2011) and assuming $R_V = 3.1$.

The optical light curves of each object are shown in Figure 1. For each object, $t_{\text{rest}} = t_{\text{obs}} = 0$ was chosen to match the peak of the transient’s optical light curve. To convert to absolute magnitude, we apply the conversion

$$M = m_{\text{obs}} - 5 \log_{10} \left(\frac{D_L}{10 \text{ pc}} \right) + 2.5 \log_{10}(1 + z). \quad (1)$$

2.2. Optical Spectroscopy

As part of our follow-up campaigns, we collected optical spectra at $t_{\text{obs}} = 4\text{--}37$ days. The dates and instruments of all spectroscopic observations are given in

Table 4 in Appendix B. We utilized the following facilities: the Gemini Multi-Object Spectrograph (GMOS; Hook et al. 2004, Gimeno et al. 2016), the Keck Low-Resolution Imaging Spectrometer (LRIS; Oke et al. 1995) on the 10 m Keck-I telescope, the Keck Cosmic Web Imager (KCWI; Morrissey et al. 2018) and the Deep Imaging Multi-Object Spectrograph (DEIMOS; Faber et al. 2003) on the 10 m Keck-II telescope, the Double Spectrograph on the Palomar 5 m telescope (DBSP; Oke & Gunn 1982), and the Binospec instrument (Fabricant et al. 2019) on the 6.5 m Multiple Mirror Telescope (MMT). As some of these spectra were taken at a time when the transient and the host galaxy’s brightness are comparable, they contain contributions from both sources.

AT2022abfc was observed using GMOS on Gemini North². This consisted of long-slit spectroscopy through a 1.0''-wide slit. The target was observed in six exposures of 450 s each at central wavelengths of 4800, 5100, and 5400 Å with the B600 grating; and at 6750, 7200, and 7650 Å with the R400 grating. The program standard star of LTT1020 was observed at the same central wavelengths at 45 s per exposure. We reduce this spectrum using DRAGONS (Labrie et al. 2023), which performs stacking of flatfields and comparison lamps, bias subtraction, and standard-star flux calibration.

For AT2023fhn, a Gemini South GMOS long-slit spectrum was taken under a target-of-opportunity (ToO) program³. The LFBOT was observed through a 1.0''-wide slit with six 450 s exposures. As with AT2022abfc, the exposures were at central wavelengths of 4800, 5100, and 5400 Å for the B600 grating, and at 6750, 7200, and 7650 Å for the R400 grating. The standard star for this observation was LTT3218, observed at the same wavelengths with an exposure length of 45 s each. Data reduction was done with DRAGONS.

The Keck-I LRIS spectrum of AT2023fhn⁴ used was obtained with a 1.0''-wide slit in “blue” and “red” optical bands. The blue band used the 400/3400 grism which covers 1300–5770 Å. The red band used the 400/8500 grating at a central wavelength of 7830 Å. We obtained four 2700 s exposures. The standard star was Feige34. Reduction was done using 1pipe (Perley 2019).

We obtained a spectrum for AT2023fhn from the DBSP on the Palomar 5 m telescope; there were three 600 s exposures on both the blue and red channels, when the target was close to the zenith (airmass of 1.06). The

² GS-2022B-Q-126; PI A. Ho

³ GS-2023A-Q-127; PI A. Ho

⁴ PI M. M. Kasliwal

¹ SOAR2024B-021; PI I. Andreoni

Table 1. LFBOT Summary

TNS name	Survey name	Redshift	RA	Dec	Offset	t_0	Ref.
			(J2000)	(J2000)	(kpc)	(UTC)	
AT2022abfc	ZTF22abvrxkk	0.212	4:51:19.200	-26:58:41.59	2.0	2022-11-21 08:15:48	This work
AT2023fhn	ZTF23aaeozpp/ATLAS23hnk	0.24	10:08:03.805	21:04:26.70	17	2023-04-12 05:22:39	[1,2]; This work
AT2023hkw	ZTF23aaaimsja	0.339	10:42:17.748	52:29:19.03	15	2023-04-30 04:08:52	This work
AT2023vth	ZTF23ableqsp	0.0747	17:56:34.403	8:02:37.30	3	2023-10-20 03:08:39	This work
AT2024qfm	ZTF24aaxhxhf/PS24hhm	0.2270	23:21:23.450	+11:56:31.99	3.7	2024-07-27 08:18:46	This work; [14]
AT2024aehp	ZTF24abygbss	0.1715	8:21:07.474	28:44:22.17	0.47	2024-12-19 10:02:49	This work
—	CSS161010	0.033	04:58:34.396	-08:18:03.95	0.28	2016-10-10 11:31:12	[3,4]
AT2018lug	ZTF18abvkwla	0.2714	02:00:15.194	+16:47:57.32	1.9	2018-09-12 09:46:48	[5]
AT2018cow	ATLAS18qqn/ZTF18abcfcoo/Gaia18bqa	0.014145	16:16:00.220	+22:16:04.91	1.7	2018-06-16 10:35:02	[6]
AT2020mr	ZTF20abfhyil/ATLAS20paa	0.1353	15:47:54.163	+44:39:07.41	1.19	2020-06-15 08:55:40	[7]
AT2020xnd	ZTF20acigmel	0.2433	22:20:02.030	-02:50:25.30	0.8	2020-10-12 04:06:03	[8]
AT2022tsd	ZTF22abftjko/PS22jvi	0.2564	03:20:10.863	+08:44:55.63	6	2022-09-07 11:21:22	[9]
AT2024wpp	GOTO24gjk/ZTF24abjjpbo/ PS24jhj/ATLAS24ond	0.0868	02:42:05.499	-16:57:22.90	5	2024-09-26 01:24:35	[10–13]

NOTE—Basic information on each LFBOT, such as position and redshift. The six LFBOTs discussed in this paper are above the line, while the rest of the known LFBOT population is shown below. t_0 is chosen to be the peak of the optical light curve. Positions of the six LFBOTs presented in the paper and AT2020xnd were determined using the methodology in Section 4.2.

References—[1] Chrmes et al. (2024a), [2] Chrmes et al. (2024b), [3] Coppejans et al. (2020), [4] Gutiérrez et al. (2024), [5] Ho et al. (2020a), [6] Prentice et al. (2018), [7] Yao et al. (2022), [8] Perley et al. (2021), [9] Ho et al. (2023c), [10] Pursiainen et al. (2025), [11] Nayana et al. (2025), [12] LeBaron et al. (2025), [13] Perley et al. (2026), [14] Nayana A.J. et al. (in prep)

slit was oriented to cover both the transient and the most likely host galaxy. Owing to high humidity, the dome was closed between the second and third exposures. The data were reduced using the official pipeline `DBSP_DRP` (Mandigo-Stoba et al. 2022), which is based on `pypeit` (Prochaska et al. 2020).

We also acquired a 1440 s spectrum of AT2023hkw with DEIMOS on the 10 m Keck-II telescope⁵. The 600ZD grating and a 1.0''-wide slit were used to produce a wavelength range of 4500–9600 Å and a spectral resolving power of $R \equiv \lambda/\Delta\lambda \approx 1300$. The slit was oriented with a position angle of 180° in order to pass through both the transient target and its host galaxy. The spectrum was reduced following standard techniques for CCD processing and spectrum extraction (Silverman et al. 2012) utilizing IRAF (Tody 1986)⁶ routines and custom Python and IDL codes⁷. Low-order polynomial fits to comparison-lamp spectra were used to calibrate the wavelength scale, and small adjustments derived from night-sky emission lines in the target frames were applied. The spectra were flux cali-

brated using observations of appropriate spectrophotometric standard stars observed on the same night, at similar airmasses, and with an identical instrument configuration.

A spectrum for AT2023vth’s host galaxy was obtained through long-slit spectroscopy with GMOS on Gemini North⁸. We used a 1.0''-wide slit in two 500 s exposures at a central wavelength of 6750 Å with the R400 grating. The standard star was G191B2B, observed with a 120 s exposure at the same central wavelength. We reduce this spectrum using the Python package DRAGONS adopting the same procedure as in AT2022abfc.

For AT2024qfm, we triggered ToO observations using GMOS on Gemini North⁹. Four 450 s exposures were taken through a 1.0''-wide slit and the R400 grating. Two exposures were at the central wavelength of 7100 Å and the other two at 7200 Å. The program standard star, BD+28 4211, was observed for at two 45 s exposures, one at each of the above central wavelengths. We obtained spectra during two classical nights using LRIS¹⁰ on the Keck-I 10 m telescope. Additional queue-based observa-

⁵ PI A. Filippenko

⁶ <https://iraf-community.github.io>

⁷ <https://github.com/ishivvers/TheKastShiv>

⁸ GN-2023B-Q-130; PI A. Chrmes

⁹ GN-2024B-Q-128, PI A. Ho

¹⁰ PI Chornock, PI Filippenko

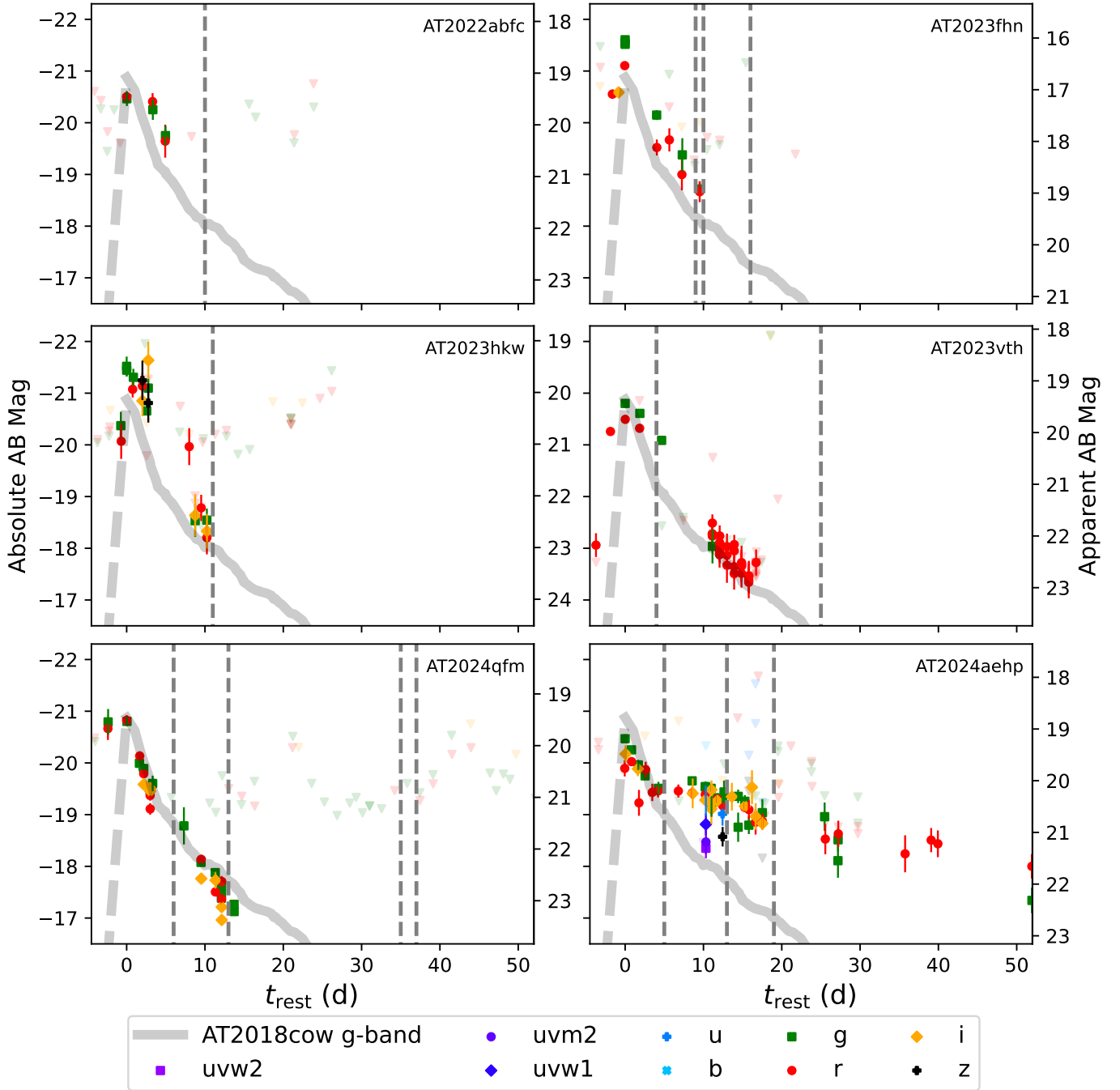


Figure 1. Optical light curves of each LFBOT (points), as well as the light curve of AT2018cow (thick gray line, where dashed lines mark the connection to the last upper limit). The left-hand ordinate values display the $E(B - V)$ corrected absolute AB magnitude (Oke & Gunn 1983) and are shared for all plots. The right-hand ordinate displays the apparent AB magnitude. Each filter has a unique marker color and style. Upside-down triangles represent 3- σ upper limits. The vertical dashed lines show when spectra of the transient and/or its host galaxy were taken. These spectra are displayed in Figure 2.

tions were collected with Binospec on the MMT¹¹. The Keck/LRIS pipeline `1pipe` is described by Perley (2019); Gemini, DOLORES, and GTC spectra were reduced us-

ing IRAF routines. MMT/Binospec spectra were reduced with standard processes using `pypeit`.

¹¹ UAO-G200-24B; PI A. A. Miller

We observed AT2024aehp using GMOS on Gemini South¹². Using a 1.0''-wide slit for long-slit spectroscopy, four exposures lasting 450s each were taken with the R400 grating. Two exposures were taken at a central wavelength of 7100 Å and the other two were at 7200 Å. The program standard star, EG21, was observed for a 45s exposure at each of the above central wavelengths. We then observed AT2024aehp with KCWI¹³. The target was near the zenith (airmass 1.1), and the sky conditions were clear. We used the large slicer and low-resolution gratings (BL, RL), which cover the wavelength range between 3650 and 8800 Å with a spectral resolution of $R \approx 1000$. The exposure time was 600s on the blue side and 3×180 s on the red side. The data were reduced using the official data-reduction pipeline. Sky subtraction, flux calibration, and telluric correction were performed using `kskywizard`¹⁴. The source spectrum was extracted using a circular aperture with a diameter of 1.3 times the full width at half-maximum intensity (FWHM) of the source in the collapsed datacube. We also obtained one epoch of long-slit spectroscopy of AT2024aehp with Binospec¹⁵. The observation consisted of 4×500 s exposures. The data were acquired with a grating of 270 lines per mm and a 1.0''-wide slit mask. The basic data processing (bias subtraction, flat fielding) was done using the Binospec pipeline (Kansky et al. 2019). The processed images were downloaded from the MMTO queue observation data archive. The spectra were reduced with IRAF, including cosmic-ray removal, wavelength calibration (using comparison-lamp frames taken on the same night as the target observation), and relative-flux calibration with archived observations of spectroscopic standards. The Binospec spectrum has wavelength coverage of 3800–9200 Å.

Spectra are shown in Figure 2. Narrow emission lines are observed from the LFBOT host galaxies, (e.g., Ca II H&K, [N II], [O II], [O III], and [S II]). The lines used to measure the redshift for each object are listed in Table 4 in Appendix B. These spectra also have a contribution from the LFBOT itself, expected to be a featureless blue continuum closely approximated by a blackbody (e.g., Margutti et al. 2019; Perley et al. 2021). The Balmer H α line is prominent in all six hosts.

2.3. *Swift* X-ray Observations

X-ray observations were obtained with the *Swift* X-ray Telescope (XRT; Burrows et al. 2005) by ToO trig-

¹² GS-2024B-Q-121 ; PI A. Ho

¹³ PI Y. Qin

¹⁴ <https://github.com/zhuyunz/KSkyWizard>

¹⁵ PI A. Gal-Yam

gers shortly after discovery of each LFBOT. Count rates for the XRT instrument were obtained from the UKSSDC *Swift* light-curve generator¹⁶. Utilizing tools from NASA HEASARC, we converted these count rates to an X-ray flux accounting for the H I column density in the Milky Way. For upper limits (all objects except AT2024qfm), we assume a power-law photon index of $\Gamma = 2$, a typical value for previous LFBOTs (Rivera Sandoval et al. 2018; Margutti et al. 2019; Bright et al. 2022; Matthews et al. 2023).

For AT2024qfm, *Swift* obtained 12 observations, from $t_{\text{obs}} \sim 8$ –133 d after the first optical detection. We visually inspected the images and discarded one observation (ID 00016748006) because the source landed on the XRT detector's hot column. The X-ray light curve shows a general decline, with the exception of one observation (ID 00016748007) which showed a significant rebrightening. This observation was extremely short, with 233 s of raw exposure but only 40s of clean data. Two source counts were detected at the position of AT2024qfm; using the Kraft et al. (1991) approach of the *Swift* tools, the implied detection significance is 99.83% (just over 3σ). Closer inspection of the data revealed no clear reason why this would be an erroneous measurement.

For purpose of comparison and for completeness, we also analyze three early *Swift* XRT observations of the LFBOT CSS161010. Late-time (100 d) observations were presented in Coppejans et al. (2020), while upper limits for these early observations were presented in Gutiérrez et al. (2024) (see their Appendix A.1). We find a very marginal (3.3σ) detection in the first epoch, and non detections in the subsequent two epochs. Our upper limits are within a factor of a few of those in Gutiérrez et al. (2024). We also show the *Chandra* detections of AT2023fnh published by Chrimes et al. (2024b), using the revised values in Nayana et al. (2025).

The *Swift* XRT observations are summarized in Table 5 in Appendix B. Five of the LFBOTs had a *Swift* non-detection, resulting in upper limits for the photon count rate and the X-ray flux. These upper limits are compared to other objects with *Swift* detections in Figure 3.

2.4. Radio and Millimeter Observations

We obtained radio observations with the National Science Foundation's Karl G. Jansky Very Large Array (VLA; Thompson et al. 1980; Perley et al. 2011), the Giant Metrewave Radio Telescope (GMRT; Swarup et al. 1991), and the Northern Extended Millimeter Array

¹⁶ UKSSDC *Swift* Light-Curve Generator

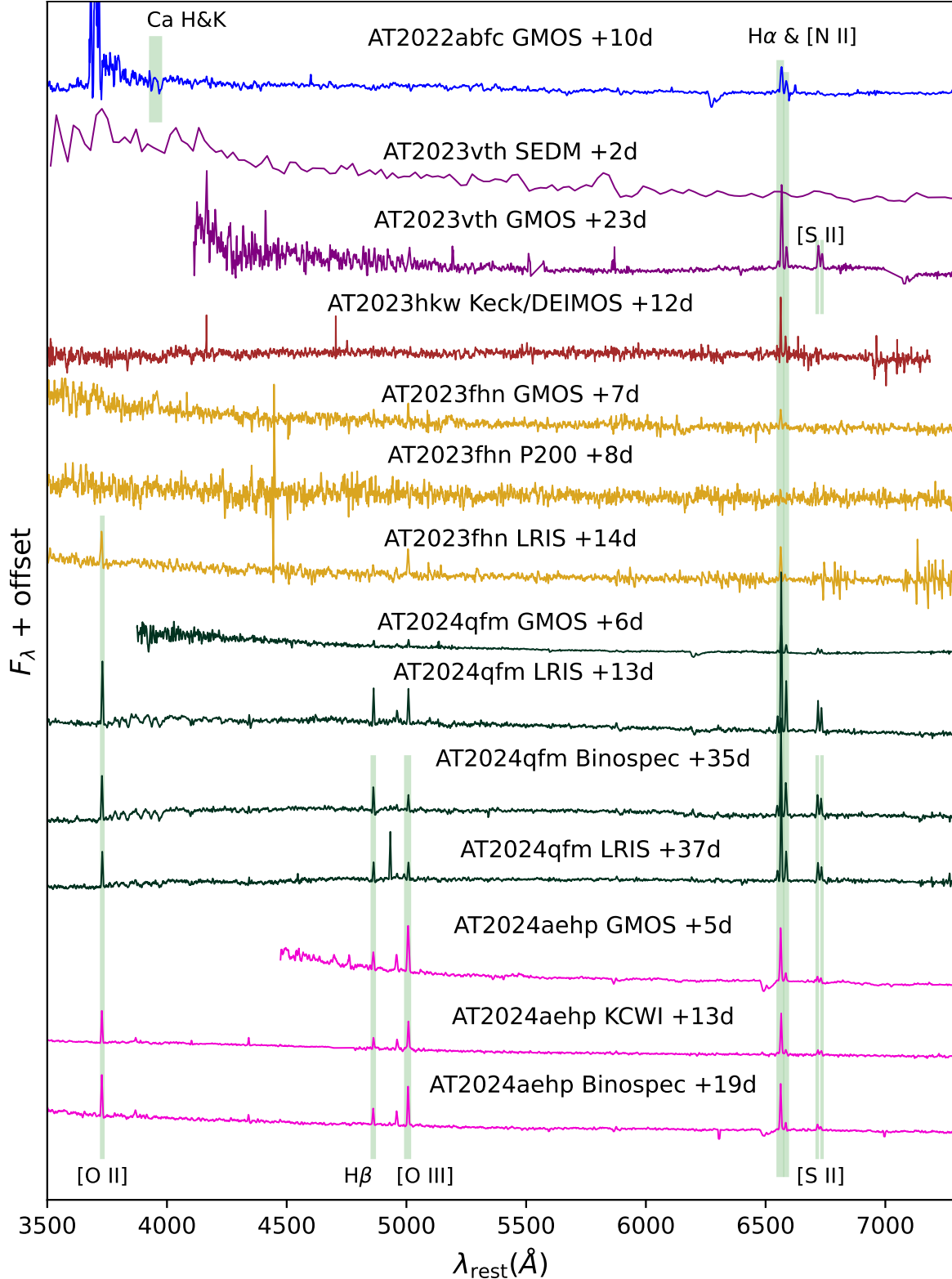


Figure 2. Spectra of each LFBOT and/or its host galaxy. For each spectrum we indicate the observer-frame epoch and instrument used. The light (dark) line is the unbinned (binned with bin size of 3 \AA) spectrum. The green shaded rectangles show galactic narrow emission lines that were used to determine a redshift. The spectra are displayed with an arbitrary vertical offset.

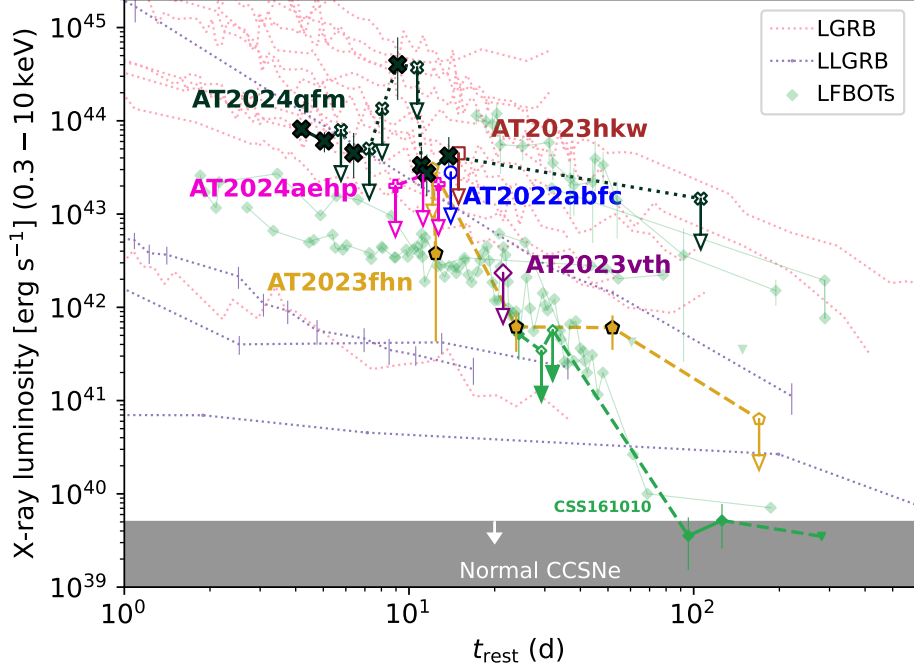


Figure 3. 0.3–10 keV X-ray light curves of the six LFBOTs in this paper, in comparison to those of other LFBOTs, gamma-ray bursts (GRBs), and low-luminosity GRBs. Open symbols with downward-facing triangles mark 3σ upper limits. Data are from Pian et al. (2000), Tiengo et al. (2004), Campana et al. (2006), Soderberg et al. (2006b), Ho et al. (2020b), Coppejans et al. (2020), Yao et al. (2022), Perley et al. (2021), Ho et al. (2022b), Perley (2023), Ho et al. (2023c), Chrimes et al. (2024a), Nayana et al. (2025), and Perley et al. (2026), as well as public *Swift* data.

(NOEMA). All of these observations are listed in Table 6 in Appendix B.

2.4.1. *VLA*

We present VLA observations for five LFBOTs¹⁷, all of which were detected. Radio data for AT2024qfm will be published by Nayana A.J. et al. in prep. Observations were obtained at mid-frequencies of 3 GHz (S-band), 6 GHz (C-band), 10 GHz (X-band), 16 GHz (Ku-band), and 33 GHz (Ka-band). Based on the behavior of past sources, 10 GHz (X-band) gives the most reliable chances of detection, so every epoch features an observation in this band. We calibrate VLA data using the automated pipeline in Common Astronomy Software Applications package version 6.5.4-9 (CASA; [Team et al. 2022](#)). We use Briggs weighting with `robust = 0.5` ([Briggs 1995](#)). When the image quality is degraded by bright artifacts from nearby luminous sources, we perform phase-only self-calibration on these other sources. Flux measurements were determined by using the Cube

Analysis and Rendering Tool (CARTA; [Comrie et al. 2021](#)). For detections, the flux density is the maximum intensity at the transient’s position, and the uncertainty is the measured root-mean square (RMS) in the background. For non-detections, we take the upper limit to be $3 \times$ RMS. The radio light curves are shown in Figure 4 and the radio spectral energy distribution (SED) evolution is shown in Figure 5.

2.4.2. *GMRT*

We also present GMRT observations of AT2022abfc, AT2023fhm, AT2023hkw, and AT2023vth. Both AT2023fhm and AT2023vth were detected. These observations were spread across three frequency bands: Band-3 (250-500 MHz), Band-4 (550-850 MHz), and Band-5 (1000-1460 MHz)¹⁸. The GMRT data were reduced through CASA and AIPS. We use Briggs weighting with `robust = 0.5`. The primary beam correction was done following the method described in the CASA documentation¹⁹. We measure the flux density using the `imfit`

¹⁷ AT2022abfc was observed under programs 22A-405 (PI D. Perley), 23A-393, 23A-422, and 23B-138; AT2023fhn under programs 23A-403 and 23B-138; AT2023vth under program 23B-138; AT2023hkw under program 23A-415; AT2024aehp under programs 24B-338 and 25A-367 (PI A. Ho)

¹⁸ AT2022abfc was observed under program ID 44_099. AT2023fhn was observed under programs 45_117 and ddtC299. AT2023hkw was observed under 45_117 and ddtC294. AT2023vth was observed under program 45_113 (PI Nayana A.J.).

¹⁹ CASA: Imaging with Custom Primary Beams

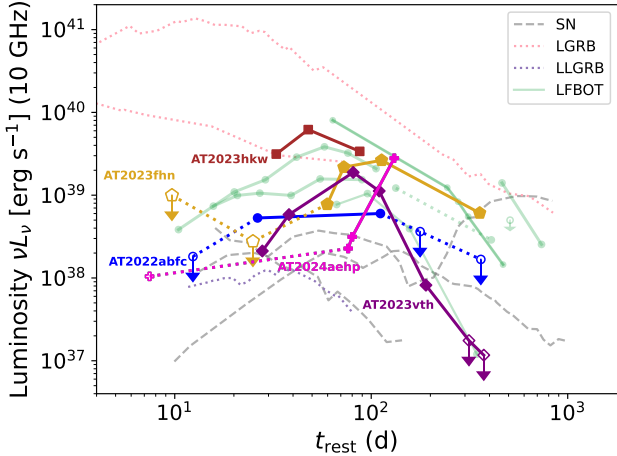


Figure 4. Radio light curves at 10 GHz of the LFBOTs with data presented in this paper, compared with other known LFBOTs, long GRBs (LGRBs), low-luminosity GRBs (LLGRBs), and core-collapse supernovae with non-relativistic ejecta (SNe). We measure time after peak light in the transient’s rest frame. Data from Kulkarni et al. (1998), Berger et al. (2003), Soderberg et al. (2006a), van der Horst et al. (2008), Soderberg et al. (2010b), Salas et al. (2013), Margutti et al. (2019), Coppejans et al. (2020), Ho et al. (2022c), Yao et al. (2022), Perley et al. (2021), Ho et al. (2023c), and Nayana et al. (2025).

method in the CASA documentation, which provides the maximum intensity for a fitted Gaussian. If the measured flux is not 3σ above the background flux RMS, we record an upper limit of $3\times$ the RMS.

2.4.3. NOEMA

We observed five LFBOTs using NOEMA²⁰ (all but AT2023hkw), at times ranging from $t = 10\text{--}100\text{ d}$, resulting in detections of three objects (AT2024aehp, AT2024qfm, AT2023vth) and non-detections of two objects (AT2022abfc, AT2023fh). The data reduction was done with Continuum and Line Interferometer Calibration (CLIC) and MAPPING, which are part of the GILDAS software package (Gildas Team 2013)²¹. Unless otherwise specified, all uncertainties are 1σ , and overall precision of the flux scale is 10% in the 3 mm band and 15% at 1.3 mm. The NOEMA data are provided in Table 6 and displayed in Figure 6.

AT2024aehp was observed on May 23, 2025 ($> 100\text{ d}$ after optical discovery; we triggered mm observations following the cm-wave detection) in the 10D configuration

under mediocre weather conditions, with MWC349 as the flux calibrator. Reduction was performed by hand and we estimate a 15% systematic calibration uncertainty for the absolute flux scale.

AT2023fh was observed on April 22, 2023 in the 12C configuration under good conditions, with LKHA101 as the flux calibrator. The image included a nearby bright source, and subtracting the contribution from the bright source did not result in a detection of AT2023fh at the phase center.

An observation of AT2022abfc was triggered on December 30, 2022; an attempt was made on January 7, 2023, but could not be carried out owing to bad weather. A successful observation was obtained on January 10 in the 12A configuration, with LKAH101 as the flux calibrator. The source was not detected, but limits were weak because the source was at high airmass and the array was in an extended configuration.

AT2023vth was first observed on November 20, 2023 in the 9C configuration, under cloudy conditions, with the flux calibrator MWC349. The source was detected, so we pursued multifrequency follow-up observations. The timing of these observations was affected by weather conditions, particularly at the highest frequencies.

NOEMA observed AT2024qfm on four dates, in compact configuration (D), with primary flux calibrator MWC349. The first observation was on August 5, 2024. The source was detected in the first three epochs.

2.5. Search for Gamma-Ray Bursts

We performed an archival search for GRB detections in the NASA General Coordinates Network Circulars²². We looked for GRBs detected within a week of the transient’s optical light-curve peak that had a localization consistent with the transient. No such GRBs were reported.

2.6. Search for X-ray Precursors

For the model by Metzger (2022) with runaway mass transfer leading up to the dynamical merger of a stripped star and compact-object companion, one might expect X-ray and UV/optical precursor emission before the LFBOT (Tsuna et al. 2024). We searched for X-ray precursor emission in the eROSITA-DE Data Release 1 (DR1). eROSITA (Predehl et al. 2021) is the soft X-ray instrument onboard the orbital observatory Spectrum-Roentgen-Gamma (SRG; Sunyaev et al. 2021). DR1 comprises data from the first six months, which ended

²⁰ Program IDs W22BT (AT2023fh and AT2022abfc), W24EW (AT2024aehp), S23BF (AT2023vth), D24AA (Director’s Discretionary Time; AT2024qfm), all PI A. Ho.

²¹ <https://www.iram.fr/IRAMFR/GILDAS>

²² <https://gcn.nasa.gov/circulars/>

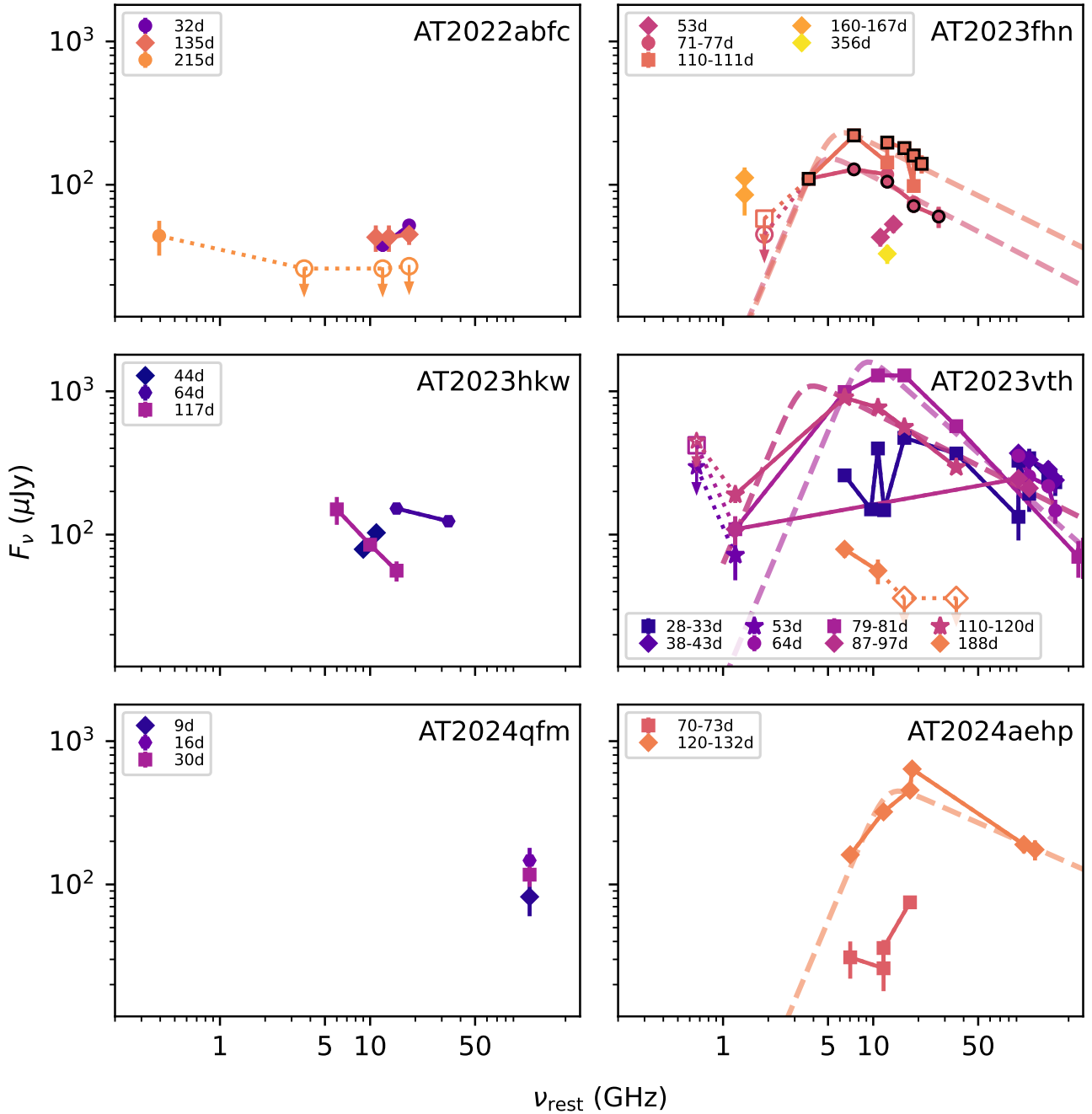


Figure 5. The radio and millimeter SED of each LFBOT at different observer-frame epochs. Observations taken within a few days are grouped into one epoch. Non-detections are signified by an unfilled marker and a downward pointing arrow. For clarity, we omit some non-detections. For epochs with sufficient data points, we display the broken power-law fit to the SED as a dashed line. Data from [Chrimes et al. \(2024a\)](#) for AT2023fhn are also displayed with a black outline.

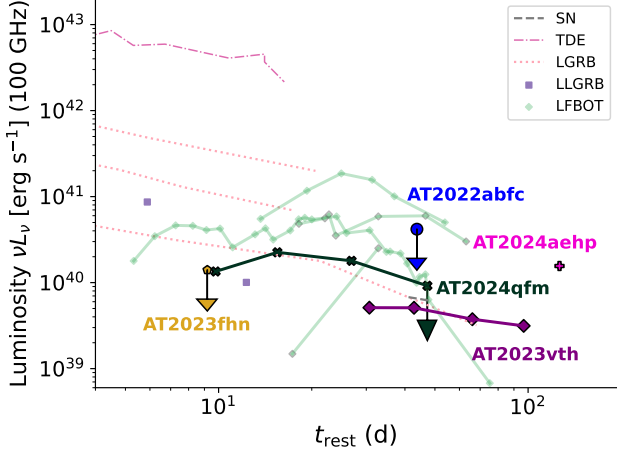


Figure 6. Millimeter-wave (100 GHz) light curves in comparison to other LFBOTs, long-duration gamma-ray bursts (LGRBs), low-luminosity GRBs (LLGRBs), and tidal disruption events (TDEs). AT2022abfc and AT2023fhn only have an upper limit. AT2023fhn has been shifted slightly to the left for clarity. Data are from Kulkarni et al. (1998); Zauderer et al. (2011); Perley (2013); Corsi et al. (2014); Laskar et al. (2016); Perley et al. (2017); Laskar et al. (2018); Margutti et al. (2019); Bright et al. (2022); Ho et al. (2023c); Nayana et al. (2025).

in June 2020 (Merloni et al. 2024; Tubín-Arenas et al. 2024).

Of the thirteen LFBOTs in Table 1, three were in the footprint of eROSITA-DE DR1: AT2022abfc, CSS161010, and AT2024wpp. For each object, we used the products from Tubín-Arenas et al. (2024) and Merloni et al. (2024) to determine if there was a detection at the source position, and if not, obtained a 0.2–2.3 keV upper limit (the most sensitive energy range for eROSITA). The closest catalogued sources were 5.5' (AT2022abfc), 3' (CSS161010), and 2' (AT2024wpp), too distant to be associated.

For AT2022abfc and AT2024wpp (the two objects for which the eROSITA observations were prior to the LFBOT), the limits are 9.1×10^{42} erg s⁻¹ corresponding to 2.7 yr pre-LFBOT, and 9.0×10^{41} erg s⁻¹ corresponding to 4.7 yr pre-LFBOT, respectively. For CSS161010, the eROSITA limit is 1.5×10^{41} erg s⁻¹, 3.4 yr after the LFBOT. The next eROSITA data release (scheduled for mid-2026) will provide more stringent upper limits (i.e., closer to the LFBOT time).

2.7. Host-Galaxy Photometry

IR and UV photometry were obtained for all LFBOT host galaxies from the Near-Earth Object Wide-field Infrared Survey Explorer mission (NEOWISE; Mainzer et al. 2011) on the *Wide-field Infrared Survey Explorer*

space telescope (*WISE*), and the *Galaxy Evolution Explorer* (*GALEX*; Martin et al. 2005), respectively. Optical photometry for the host galaxies was obtained from the Legacy Survey Data Release 10 (Dey et al. 2019). The host galaxy of AT2023vth does not have Legacy Survey optical photometry, so we used optical photometry from Pan-STARRS DR2 (PS1; Chambers et al. 2016). We also used *Hubble Space Telescope* (*HST*) photometry from Chrimis et al. (2024b) for AT2023fhn. For the photometry in all bands, we required a signal-to-noise ratio (SNR) greater than 5 for a detection.

We used the Python package `gPhoton` (Million et al. 2016) to retrieve *GALEX* near-UV and far-UV photometry for the LFBOT host galaxies. In `gPhoton`, we chose the observation with the longest exposure time and recorded the background-corrected magnitudes. We chose an aperture radius of 6.12 arcseconds for the source, and measured the background from an annulus with an inner radius of 10.8 arcseconds and an outer radius of 21.6 arcseconds. In the cases of AT2023hkw and AT2023vth, early UV-bright sources required us to use a different annulus. The inner and outer annulus radii are 10.8 and 16.2 arcseconds for AT2023hkw, and 7.2 and 10.8 arcseconds for AT2023vth. Legacy Survey and *NEOWISE* photometry was obtained with the Python package `noaodatalab`²³ version 2.20.0. Pan-STARRS DR2 *grizy* photometry was obtained from the online catalog search tool²⁴.

The host-galaxy photometry is provided in Table 7 in Appendix B.

3. OBSERVATIONAL COMPARISON

The observations presented in Section 2 show relative homogeneity in the optical (Figure 1) and radio (Figure 4) light curves. To some extent the similarity of the optical light curves to those of AT2018cow is by selection, as these objects were identified on the basis of a rapid rise and decay along with high luminosities. The rapid decline of 3–4 mag over $t_{\text{rest}} \approx 10$ d observed in AT2023fhn, AT2023vth, AT2023hkw, and AT2024qfm — very similar to AT2018cow — was not selected for. The light curve of AT2024aehp plateaued at $M = -19$ mag from 5–50 d, behavior we can rule out in AT2023vth and AT2024qfm.

The similarity between the radio light curves is less of a selection effect. Figure 4 shows that the peak νL_{ν} values mostly lie within the range of 10^{39} – 10^{40} erg s⁻¹. The time evolution for the radio emission is also fairly similar across most of the sample except for AT2024aehp. The

²³ <https://github.com/astro-datalab/datalab>

²⁴ <https://catalogs.mast.stsci.edu/panstarrs/>

luminosity gradually rises, plateaus between $t_{\text{rest}} \sim 50$ –100 d after the initial discovery, and then begins to fade. During the rise, the radio emission is typically optically thick (has a positive spectral index; Figure 5). The fade rates of the radio emission vary, and in some cases are poorly constrained (e.g., for AT2022abfc). The fast fade of AT2023vth is similar to that of CSS161010 (Coppejans et al. 2020). Similarly, the mm-wave light curves appear to peak close to $t_{\text{rest}} = 20$ –30 d (Figure 6).

The uniformity of the radio luminosity and evolution of all AT2018cow-like FBOTs is striking. Of course, the radio emission had to be sufficiently luminous to be detected in the first place, but we did not require the radio luminosity to brighten over time, nor was there a requirement about the timing of the peak. The radio behavior is in sharp contrast to CCSN radio light curves, which span over four orders of magnitude in luminosity, with peak times ranging from a few days to thousands of days (Bietenholz et al. 2021).

As with the optical light curves, AT2024aehp is the outlier in terms of radio evolution. As shown in Figure 4 and Figure 5, AT2024aehp dramatically brightens in radio luminosity at a later time than the other transients we have discussed, by over an order of magnitude in all frequencies between the $t_{\text{rest}} \sim 70$ d and $t_{\text{rest}} \sim 120$ d epochs. In contrast, the radio emission of other LFBOTs has already peaked by $t_{\text{rest}} \sim 120$ d and begun to shift to lower frequencies. We discuss AT2024aehp in more detail in Section 5.1.

We have fewer constraints on the X-ray behavior, as several of the objects only have upper limits on their luminosity (the calculated X-ray luminosity upper limits are driven mostly by their redshift, as *Swift* determined similar photon count upper limits for each non-detection). These upper limits appear to rule out X-ray emission similar to those of jetted TDEs or classical LGRBs. However, most allow for the possibility of X-ray emission similar to that of AT2018cow. The order-of-magnitude jump in X-ray luminosity seen in AT2024qfm over just two days is much more pronounced than the X-ray variability observed in past LFBOTs.

4. ANALYSIS

4.1. Radio Synchrotron Modeling

We model the SED at radio and millimeter wavelengths as the result of synchrotron emission. Synchrotron radiation with a self-absorbed component forms a broken power-law radio SED. We follow the prescription of Chevalier (1998) to derive properties of the shock and the medium it traverses, such as the shock radius, ambient magnetic field, average shock velocity, pre-shock density, and total shock energy. This is the same

procedure used in modeling the radio SEDs for other AT2018cow-like FBOTs (e.g., Margutti et al. 2019; Ho et al. 2019; Chrimes et al. 2024b; Nayana et al. 2025; Perley et al. 2026). We note that in some of these works, some equations are given in terms of angular diameter distance D_θ , but should be given in terms of luminosity distance (D_L ; private communication) as in the expressions below. We also note that the following prescription assumes a nonrelativistic shock and does not account for relativistic effects (see, e.g., Margalit & Quataert 2024; Ferguson & Margalit 2025), which become relevant for $\Gamma\beta \sim 1$.

As in Soderberg et al. (2010a), we assume equipartition of energy between protons, electrons, and the magnetic field; thus, the energy densities in electrons (ϵ_e) and magnetic fields (ϵ_B) are given by $\epsilon_e = \epsilon_B = 1/3$. If we model the source of the emission as a disk with radius R and thickness S , then its total volume is $\pi R^2 S$. We then parameterize this as equivalent to a spherical volume $4\pi f R^3/3$, where f is the filling factor. We take $f = 0.5$ as in previous LFBOT studies (Yao et al. 2022; Bright et al. 2022), but the dependences of the equations on this parameter is weak. We assume an electron power-law index of 3, following Chevalier & Fransson (2006); this is a typical value for previous LFBOTs (Coppejans et al. 2020; Ho et al. 2019, 2020a; Yao et al. 2022).

Finally, we verify that the self-absorption frequency is less than the cooling frequency, which is defined as the frequency where the electrons have lost an amount of energy equal to their total energy through synchrotron cooling. We use Equation (C13) of Ho et al. (2022c), which gives the ratio between the self-absorption and cooling frequencies, and confirm that the self-absorption frequency is lower for all cases.

Under these assumptions, Equations (13) and (14) from Chevalier (1998) reduce to these expressions for the shock radius and magnetic field:

$$R_p = 8.8 \times 10^{15} \left(\frac{\epsilon_e}{\epsilon_B} \right)^{-1/19} \left(\frac{f}{0.5} \right)^{-1/19} \left(\frac{F_p}{(1+z) \text{ Jy}} \right)^{9/19} \times \left(\frac{D_L}{\text{Mpc}} \right)^{18/19} \left(\frac{\nu_p}{5 \text{ GHz}} \right)^{-1} \text{ cm}, \quad (2)$$

$$B = 0.58 \left(\frac{\epsilon_e}{\epsilon_B} \right)^{-4/19} \left(\frac{f}{0.5} \right)^{-4/19} \left(\frac{F_p}{(1+z) \text{ Jy}} \right)^{-2/19} \times \left(\frac{D_L}{\text{Mpc}} \right)^{-4/19} \left(\frac{\nu_p}{5 \text{ GHz}} \right) \text{ G}, \quad (3)$$

where D_L is the luminosity distance, ν_p is the peak frequency of the radio SED in the frame of the transient, and F_p is the flux density at ν_p .

Following Ho et al. (2019), this can then be combined into an equation for total energy $U = U_B/\epsilon_B$:

$$\begin{aligned} U &= \frac{B^2}{8\pi} \frac{4\pi f R^3}{3} \frac{1}{\epsilon_B} \\ &= 1.9 \times 10^{46} \left(\frac{1}{\epsilon_B} \right) \left(\frac{\epsilon_e}{\epsilon_B} \right)^{-11/19} \left(\frac{f}{0.5} \right)^{8/19} \\ &\quad \times \left(\frac{F_p}{(1+z) \text{ Jy}} \right)^{23/19} \left(\frac{D_L}{\text{Mpc}} \right)^{46/19} \left(\frac{\nu_p}{5 \text{ GHz}} \right)^{-1} \text{ erg.} \end{aligned} \quad (4)$$

We estimate the average velocity as $R/(t_{\text{obs}}/(1+z)) = R/t_{\text{rest}} = \Gamma\beta c$, where $\beta = v/c$ and Γ is the Lorentz factor.

Following Chrimes et al. (2024b), we derive formulas for the CSM electron number density n_e and the wind density \dot{M}/v_w . This assumes the CSM resulted from a spherical stellar wind with mass-loss rate \dot{M} and wind velocity v_w , where $\dot{M}/v_w = 4\pi m_p R^2 n_e$ and m_p is the proton mass. Thus,

$$\begin{aligned} n_e &= 1.02 \frac{1}{\epsilon_B} \left(\frac{\epsilon_e}{\epsilon_B} \right)^{-6/19} \left(\frac{f}{0.5} \right)^{-6/19} \left(\frac{F_p}{(1+z) \text{ Jy}} \right)^{-22/19} \\ &\quad \times \left(\frac{D_L}{\text{Mpc}} \right)^{-44/19} \left(\frac{\nu_p}{5 \text{ GHz}} \right)^4 \left(\frac{t_{\text{rest}}}{\text{days}} \right)^2 \text{ cm}^{-3}, \end{aligned} \quad (5)$$

$$\begin{aligned} \frac{\dot{M}}{v_w} \left(\frac{1000 \text{ km s}^{-1}}{10^{-4} M_{\odot} \text{ yr}^{-1}} \right) &= 2.5 \times 10^{-5} \left(\frac{1}{\epsilon_B} \right) \left(\frac{\epsilon_e}{\epsilon_B} \right)^{-8/19} \\ &\quad \times \left(\frac{f}{0.5} \right)^{-8/19} \left(\frac{F_p}{(1+z) \text{ Jy}} \right)^{-4/19} \\ &\quad \times \left(\frac{D_L}{\text{Mpc}} \right)^{-8/19} \left(\frac{\nu_p}{5 \text{ GHz}} \right)^2 \\ &\quad \times \left(\frac{t_{\text{rest}}}{\text{days}} \right)^2. \end{aligned} \quad (6)$$

The peak frequency and flux density of the SED at a given epoch are measured by fitting a smoothed broken-power law of the form

$$F(\nu) = F_p \left((\nu/\nu_p)^{-sa_1} + (\nu/\nu_p)^{-sa_2} \right)^{-1/s}. \quad (7)$$

We choose $s = 1$ for the smoothness parameter, as was done in previous LFBOT studies (Bright et al. 2022; Chrimes et al. 2024a; Nayana et al. 2025). We also set

$a_1 = 5/2$ to fix the power-law slope of the self-absorbed half of the SED, as required by Chevalier's formulation. When an epoch involves observations from multiple observations, we impose a 10% error floor on the flux density. A fit is performed only when we have detections on either side of the SED's peak. The best-fit parameters from the broken power-law fit are provided in Table 8 in Appendix B. If we are unable to perform a broken power-law fit, we use the values at the detection closest to the peak's implied location in place of the frequency and flux density at peak, and calculations based on these values will instead set limits on the synchrotron parameters. The inferred synchrotron parameters are listed in Table 9 in Appendix B, and the results are displayed in Figure 7. This includes epochs where we do fit a broken-power law and have point estimates for parameters, and epochs where we can only constrain the peak's location and place limits on parameters instead. We find that the implied CSM densities for these six LFBOTs are comparable to those derived in the literature for previous LFBOTs, with values of $10\text{--}100 \text{ cm}^{-3}$ at radii of 10^{17} cm .

4.2. Host Galaxy Offsets

Using the expanded sample of 13 LFBOTs, we also examine the distribution of their offsets from their host-galaxy nuclei. For AT2023fhn, we used the localization from *HST* imaging presented by Chrimes et al. (2024b). For AT2024qfm, we use the localization from the ZTF data as we do not present radio data for that object in this paper. For the other objects, including AT2020xnd (which did not have a published offset) we obtained the transient's position from a Gaussian fit in the image of the LFBOT's brightest radio detection. We measure the host galaxy's position from Legacy Survey Data Release 10, except for AT2023vth's host which was measured from Pan-STARRS Data Release 2. These offsets are recorded in Table 1.

In Figure 8, we display the cumulative distribution of all LFBOT offsets in kpc compared with other classes of extragalactic explosive transients. The offset distribution appears to be intermediate to that of CCSNe and that of LGRBs and SLSNe, although we caution that the number of objects is small.

4.3. Host-Galaxy Properties

We used the Python package `prospector` (Leja et al. 2017; Johnson et al. 2021)²⁵ to derive properties such

²⁵ <https://github.com/bd-j/prospector>

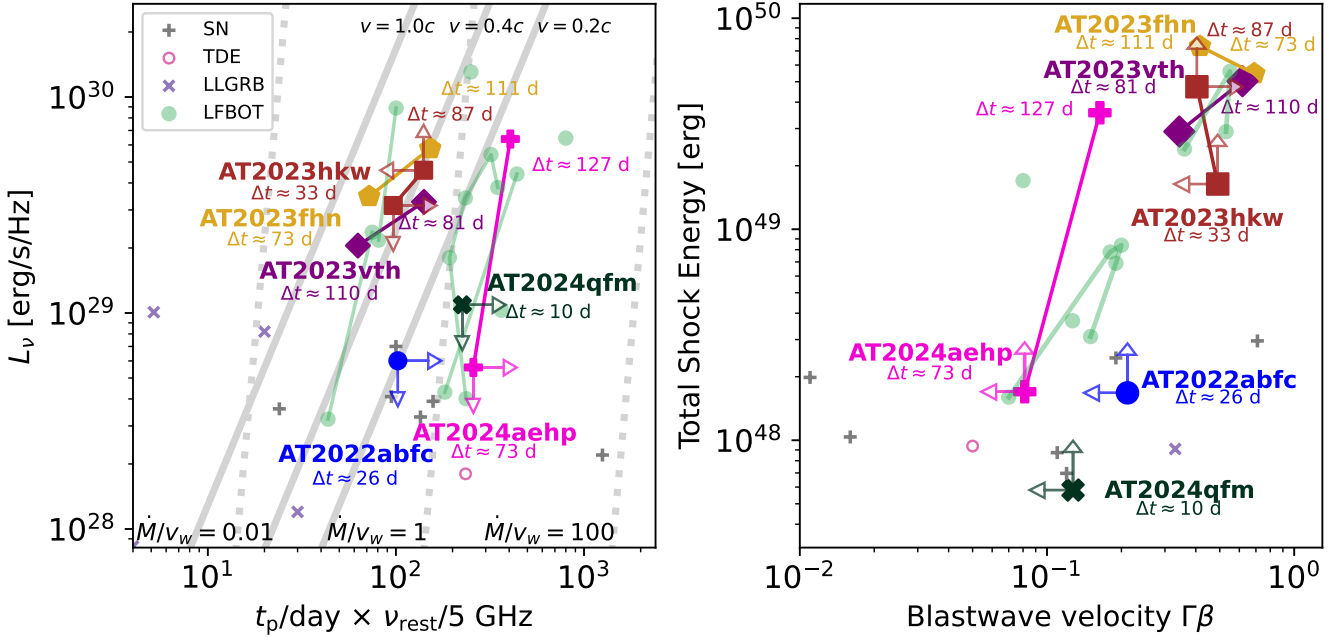


Figure 7. Inferred parameters from our synchrotron self-absorption modeling. Some epochs do not include the self-absorption peak and merely constrain its location; the corresponding upper limits on parameters are marked with arrows. Values for other objects are obtained from Ho et al. (2019) and Ho et al. (2023c); and Perley et al. (2026) for AT2024wpp. We label each object and the observer-frame time after peak light. *Left:* Luminosity density at ν_p versus peak frequency and time after explosion. We also display lines of constant shock velocity and \dot{M}/v_w , where $v_w = 1000 \text{ km s}^{-2}$ and \dot{M} is in units of $10^{-4} M_\odot \text{ yr}^{-1}$. *Right:* Total shock energy derived from Equation 4 against shock velocity in terms of $\Gamma\beta$.

Table 2. Host-Galaxy Properties

Object	Mass ($\log M/M_\odot$)	Metallicity ($\log Z/Z_\odot$)	Age (Gyr)	SFR ($M_\odot \text{ yr}^{-1}$)	Host Extinction (τ)
AT2022abfc	$10.80^{+0.02}_{-0.04}$	0.05	$1.0^{+0.1}_{-0.2}$	$4.3^{+0.6}_{-0.6}$	$0.83^{+0.04}_{-0.04}$
AT2023fhn	$10.07^{+0.06}_{-0.06}$	-0.27	$0.7^{+0.5}_{-0.2}$	$7.7^{+1.4}_{-1.1}$	$0.59^{+0.05}_{-0.05}$
AT2023hkw	$10.7^{+0.1}_{-0.1}$	0.03	$2.7^{+1.2}_{-0.8}$	$2.8^{+1.3}_{-0.8}$	$0.22^{+0.17}_{-0.14}$
AT2023vth	$8.95^{+0.03}_{-0.04}$	-0.60	$0.62^{+0.13}_{-0.07}$	$0.24^{+0.04}_{-0.03}$	$0.0035^{+0.0055}_{-0.0026}$
AT2024qfm	$10.2^{+0.2}_{-0.1}$	-0.20	$4.4^{+5.0}_{-3.1}$	$3.3^{+1.1}_{-1.1}$	$0.60^{+0.14}_{-0.13}$
AT2024aehp	$8.9^{+0.1}_{-0.1}$	-0.60	$0.8^{+0.3}_{-0.3}$	$1.6^{+0.2}_{-0.2}$	$0.63^{+0.05}_{-0.05}$

NOTE—Results of our `prospector` host-galaxy fits. Metallicities were not determined by the fitting process, but by using a preliminary run at $\log Z/Z_\odot = -0.2$, and then converting the mass estimate to a metallicity using Gallazzi et al. (2005). For the host galaxy extinction, we report the `dust2` parameter. FSPS defines this parameter as the optical depth τ in an extinction factor of $e^{-\tau}$ at the wavelength of 5500 Å.

as stellar mass and star-formation rate (SFR) from the host-galaxy photometry (Table 7). The best-fit photometry and spectroscopy from `prospector` are displayed in Figure 9, and the fitted host-galaxy properties are listed in Table 2. We show the median host-galaxy masses and SFRs in Figure 10.

The `prospector` package utilizes the Flexible Stellar Population Synthesis²⁶ (FSPS) package to model the emission from each galaxy given a set of parameters for the galaxy’s composition and stellar population. We used the package to fit observations to the modeled

²⁶ <https://dfm.io/python-fps/current/>

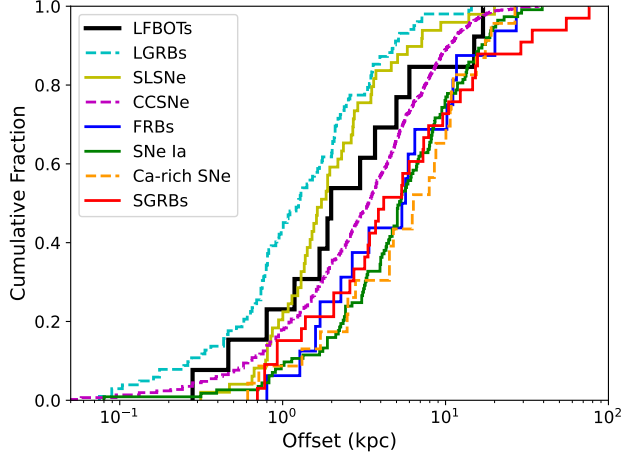


Figure 8. The cumulative distribution of host-galaxy offsets for LFBOTs, as well as fast radio bursts (FRBs; Bhandari et al. 2022), LGRBs (Blanchard et al. 2016; Lyman et al. 2017), short GRBs (SGRBs; Fong et al. 2022), CCSNe (Kelly & Kirshner 2012; Schulze et al. 2021), Type Ia SNe (Wang et al. 2013), SLSNe (Lunnan et al. 2015; Schulze et al. 2021), and Ca-rich transients (De et al. 2020). The offsets for previous LFBOTs are from Prentice et al. (2018); Coppejans et al. (2020); Ho et al. (2020a); Yao et al. (2022); Chrimes et al. (2024b).

spectrum using `dynesty`²⁷. The basic parametric star-formation history template is adopted along with the parameters for nebular emission. We chose the Chabrier initial mass function (Chabrier 2003), the Calzetti dust attenuation model (Calzetti et al. 2000), and a star-formation history of the form $te^{-t/\tau}$. A model was first run with a fixed metallicity of $\log(Z/Z_{\odot}) = -0.2$. Then, we used the median mass and the mass-metallicity relation of Gallazzi et al. (2005) to fix the metallicity to a more accurate value, and ran a final model. Our host-galaxy properties derived for the host of AT2023fhm agree with Chrimes et al. (2024a) to within $1-\sigma$ for host-galaxy mass and $2-\sigma$ for SFR.

The host galaxies of our LFBOTs are all star-forming galaxies. Whereas several previous events were in low-mass dwarf galaxies (Ho et al. 2020a; Coppejans et al. 2020; Chrimes et al. 2024b; Margutti et al. 2019), the host galaxies of four of our new LFBOTs have higher masses (10^{10} – $10^{11} M_{\odot}$, Figure 10). However, our selection criteria for identifying LFBOT candidates do require there to be a visible host galaxy (to avoid contamination by dwarf novae), so a bias to higher mass galaxies is to be expected.

²⁷ <https://github.com/joshspeagle/dynesty>

To compare the *intrinsic* distribution of host-galaxy mass to that of CCSNe, we used the untargeted sample of 150 CCSN host galaxies from Taggart & Perley (2021) as representative of the true CCSN host galaxy population. For each of the thirteen LFBOT host galaxies, we calculate the minimum absolute magnitude for it to have been detected by the Legacy Survey at that redshift, which corresponds to the apparent magnitude cutoff of $m_r \leq 23$. Then, for each CCSN host galaxy, we apply a weight equal to the proportion of the thirteen cutoffs that the CCSN host galaxy would pass. We do not account for any systematic differences in host galaxy properties between those at redshift $z \approx 0.01$ as in the Taggart sample, and those at $z \approx 0.1$ – 0.2 as with most of the LFBOTs. We plot the Gaussian kernel density estimation (KDE) for the weighted distribution of CCSN host-galaxy masses Figure 11 as a dotted red line. The Gaussian KDE for the LFBOT host-galaxy masses is shown in black. We repeated the exercise for SLSNe, which are known to have a preference for lower galaxy masses than regular CCSNe (Taggart & Perley 2021).

We use the `Ecume` package (Roux de Bezieux 2024) in the programming language `R` (R Core Team 2025) to perform a Kolmogorov-Smirnov (KS) test comparing the distribution of LFBOT host-galaxy masses with the weighted CCSN and SLSN populations, with the results displayed in Table 3. These simulations imply that the LFBOT host-galaxy population is consistent with both the populations of CCSN and SLSN host galaxies at a significance of $\alpha = 0.05$ ($p < 0.05$ would mean the distributions are different at 95% confidence). The SLSN host-galaxy distributions appears especially similar to that of LFBOTs. However, the SLSNe are subdivided into SLSNe-I and SLSNe-II. These two classes are markedly different, and this is reflected in their host-galaxy masses—SLSN-I host galaxies are clustered around $\log(M/M_{\odot}) \approx 8$ while SLSN-II hosts are $\log(M/M_{\odot}) \approx 9$ – 10 . Despite the visible differences, the sample sizes of SLSN-I and SLSN-II hosts are too small to find a statistically significant difference at $\alpha = 0.05$.

5. DISCUSSION

5.1. Implications for Progenitors

The consistent radio light curves imply consistent properties of the surrounding medium on scales of $\sim 10^{16}$ – 10^{17} cm. The radio behavior favors progenitor theories that can explain the presence of a dense ambient medium that is fairly similar from event to event. This is hard to reconcile with a TDE scenario, as discussed in previous work (e.g., Margutti et al. 2019; Perley et al. 2026). Difficulties also arise in the massive-star core-

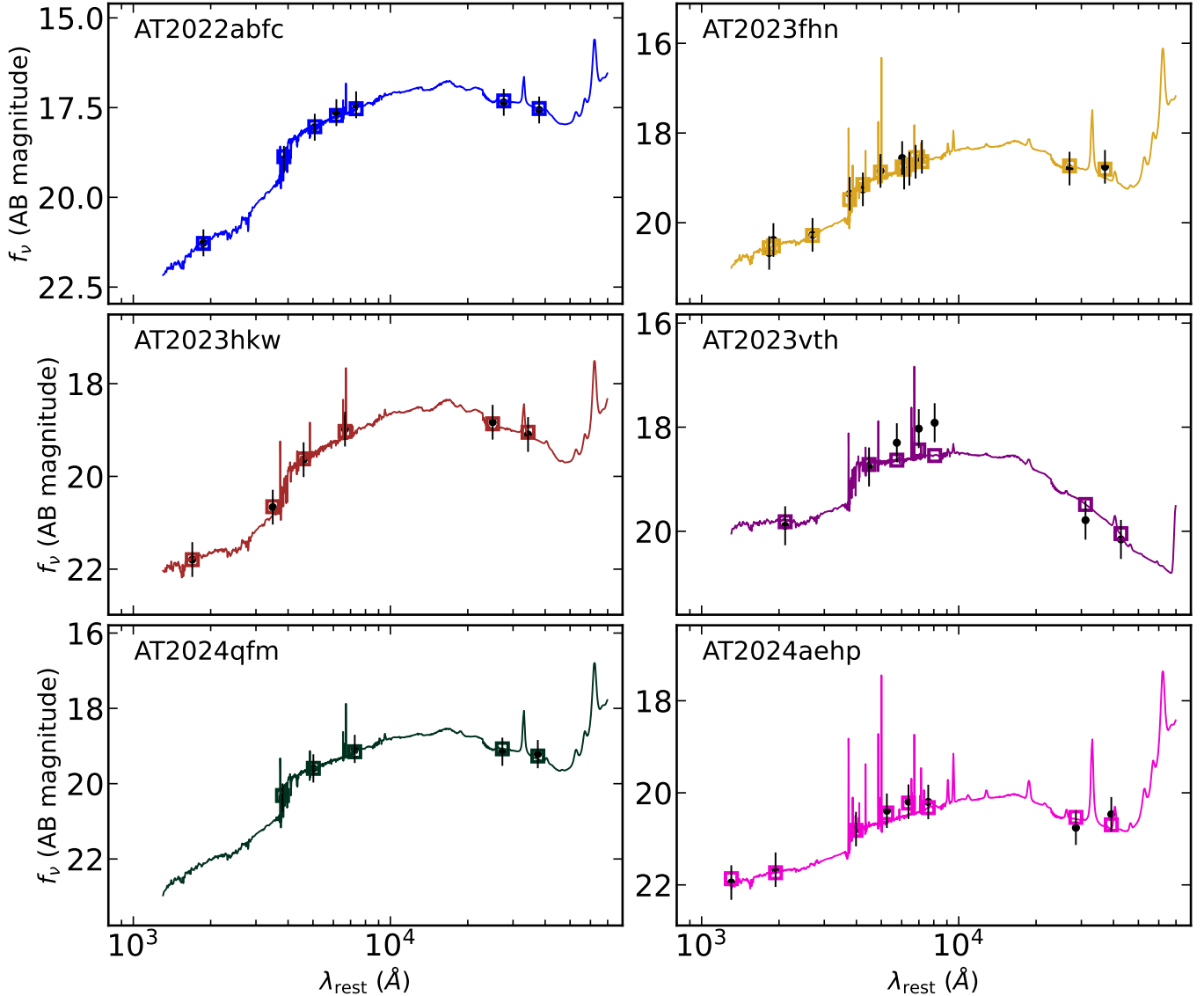


Figure 9. Best-fit host-galaxy spectra and photometry from `prospector` (color) as well as the input photometry (black circles with error bars). Note that the parameters reported in Table 2 are the median, 16th percentile, and 84th percentile. The best-fit host galaxy spectra displayed here corresponds to the maximum-likelihood parameters, which are not necessarily the median parameters. The abscissa displays rest-frame wavelength.

Table 3. Kolmogorov-Smirnov Test for Host-Galaxy Masses

Comparison Population	<i>p</i> -value
CCSN	0.43
SLSN	0.96
SLSN-I	0.07
SLSN-II	0.39

NOTE—Results of a two-tailed Kolmogorov-Smirnov test between the LFBOT host-galaxy mass distribution, and the host-galaxy mass distributions of four populations (CCSN, SLSN, SLSN-I, SLSN-II).

collapse model: the stars that we usually suspect to be the progenitors of luminous explosions and energetic SNe are not expected to undergo significant mass loss in such a consistent way just prior to the explosion (indeed, SN radio light curves are highly diverse). On the other hand, progenitor models involving mergers (e.g., Metzger 2022; Tsuna & Lu 2025; Klencki & Metzger 2025) naturally explain the dense medium as material ejected from the merger.

AT2024aehp has several characteristics that distinguish it from the other LFBOTs in this paper. Its optical light curve exhibited a plateau beginning five

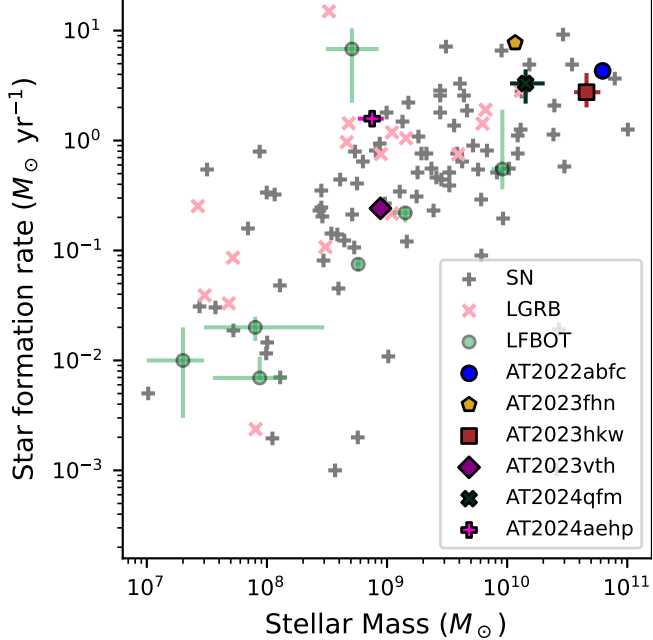


Figure 10. Median mass and SFR for each LFBOT’s host galaxy in comparison to the host galaxies of other energetic transients. Colored lines show error bars, though they may be smaller than the marker for some points.

days after peak light. Its radio emission displayed a substantial rebrightening over 100 days after its discovery. Out of all the LFBOTs discussed, AT2024aehp is one of the closest to the nucleus of its host galaxy, with a projected distance within 1 kpc. The properties of AT2024aehp are reminiscent of TDEs. TDEs also exhibit late-time radio brightening (Horesh et al. 2021; Cendes et al. 2024) and have a slower optical light-curve decay, following $t^{-5/3}$ (Evans & Kochanek 1989). While known TDEs have optical rises lasting weeks (Blagorodnova et al. 2017), a TDE from an intermediate-mass black hole could have a much shorter rise (Kuin et al. 2019; Perley et al. 2019; Gutiérrez et al. 2024). Indeed, the transient AT2024puz—which produced luminous optical/UV evolving on a ≈ 20 d timescale as well as luminous (10^{44} erg s $^{-1}$) X-ray emission—was posited to be an object intermediate between LFBOTs and TDEs (Soomalwar et al. 2025). Observations of AT2024aehp are ongoing, and a detailed analysis of this transient will be presented in future work.

5.2. Considerations for Future Work

From our work discovering and performing multiwavelength observations of LFBOTs, we have identified areas to improve on for future analysis, summarized below.

Observations – The optical light curve plateau of AT2024aehp motivates long-term (> 10 d) optical monitoring of LFBOTs. As shown in Figure 1, this extended

follow-up was not present in our sample’s early LFBOTs, which limits our ability to constrain the presence of a similar plateau. We should also aim to detect an AT2024aehp-like late radio brightening at $t_{\text{rest}} \sim 120$ d. This requires an epoch of radio observations around 10 GHz at this time, even if we expect any early radio emission to have already faded.

Another gap in our follow-up observations is the lack of X-ray detections for most of these LFBOTs. *Swift* observations were not sensitive enough to rule out levels of X-ray emission that have already been detected in previous LFBOTs such as CSS161010 (Coppejans et al. 2020) and AT2018cow (Perley et al. 2019). Going forward, deeper *Chandra* observations should be obtained for each object, as was done in, e.g., AT2023fhn (Chrimes et al. 2024a).

Modeling – The models we use in this paper’s analysis could be improved upon or have assumptions that could be relaxed to explore a wider range of parameter space.

We use the model of Chevalier (1998) to derive properties of the shock and ambient medium from our radio and millimeter observations. This formulation requires assuming that certain conditions hold, such as the equipartition of energy, a non-thermal electron energy distribution, and that the shock is spherical and nonrelativistic. The nonrelativistic assumption will introduce some inaccuracies, as we calculate some values of $\Gamma\beta$ that are greater than 0.5. We also assume values for the filling factor f , ϵ_e , ϵ_B , and the electron power-law index, and our results do depend on these parameters. A future analysis could relax some of these assumptions or fit for parameters that we set to be fixed. Some of these flaws can be inferred from our fitting results. According to Chevalier (1998), the broken power-law fit should have a $\nu^{5/2}$ dependence in the optically thick regime and a $\nu^{-(p-1)/2}$ dependence in the optically thin regime, where p is the electron power-law index. We assume $p = 3$, so the optically thin dependence should be as ν^{-1} . However, for most epochs we do not have enough detections to confirm a $\nu^{5/2}$ dependence in the optically thick regime (Figure 5). In addition, from the results shown in Table 8, the observed slopes in the optically thin regime are not all consistent with ν^{-1} . Work has already been done to extend this model to account for thermal electrons (Margalit & Quataert 2021) and relativistic effects (Margalit & Quataert 2024; Ferguson & Margalit 2025). Generalizing and refining the synchrotron model would help obtain more rigorous estimates of shock and ambient medium parameters.

In our `prospector` fits for the LFBOT host-galaxy properties, we used a single prescription for the SFH, dust model, and initial mass function, but a future anal-

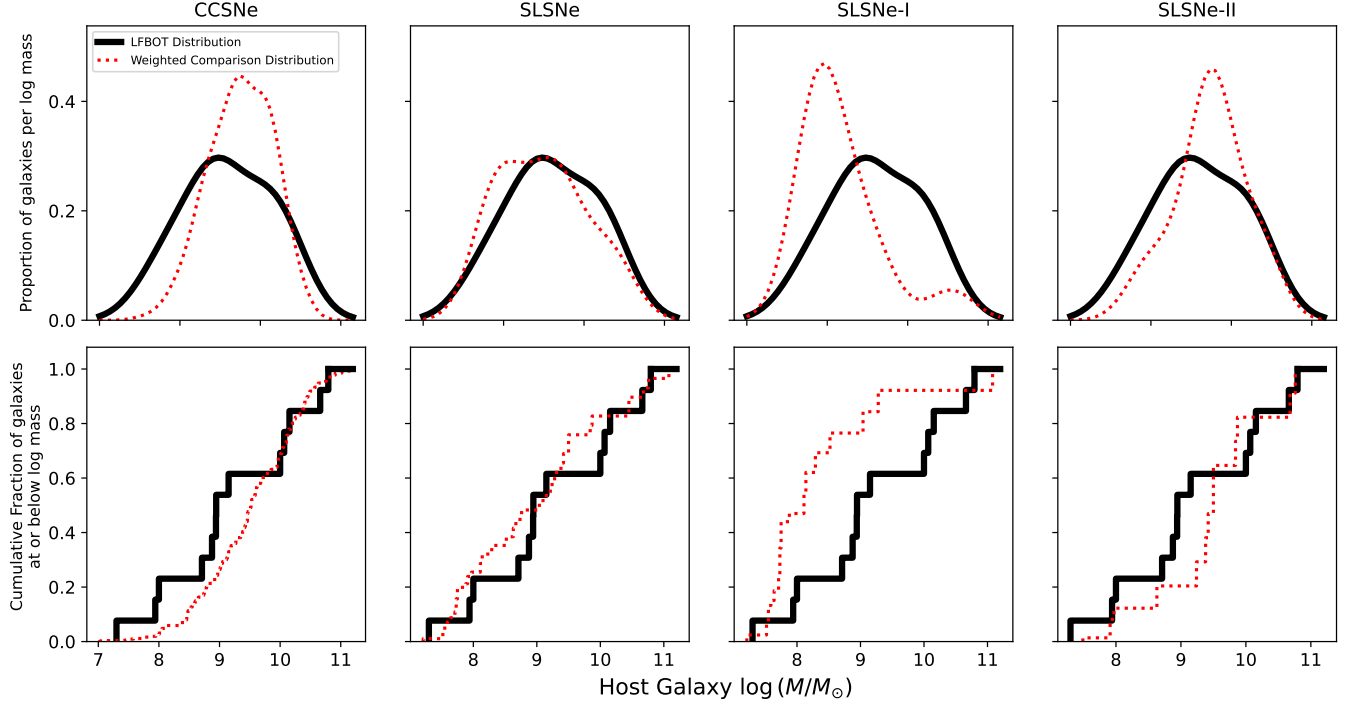


Figure 11. Gaussian KDEs for the LFBOT host-galaxy masses (black) in comparison to the Gaussian KDEs for each of the weighted mass distributions from the [Taggart & Perley \(2021\)](#) CCSN/SLSN host-galaxy population (dashed red).

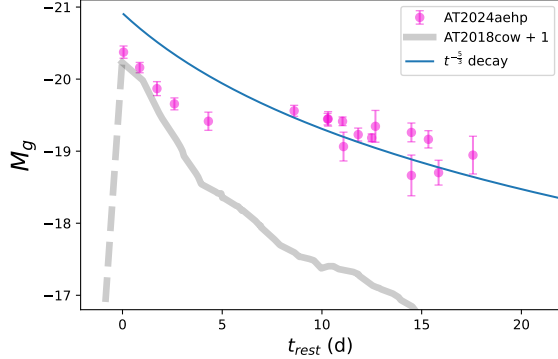


Figure 12. Optical g -band light curves for AT2024aehp (pink points) and AT2018cow (gray line). AT2018cow represents a typical LFBOT light curve. We also show a best fit of a $t^{-5/3}$ decay to the AT2024aehp light curve. The time axis is measured in the rest frame of each transient, where $t_{\text{rest}} = 0$ refers to the peak of the optical light curve.

ysis should ensure that results are robust to different choices for these parameters. In particular, we use a parametric SFH, but models with a non-parametric SFH could produce vastly different results. We also omit the spectra when performing our fits, as it is difficult to standardize spectra from different observing conditions, processed through different software, and possessing different levels of contamination from the transient itself. This required us to use the mass-metallicity relation in

[Gallazzi et al. \(2005\)](#) to fix a metallicity in our models. While we are confident these have produced a good metallicity estimate, incorporating a host-galaxy spectrum obtained after the transient faded would produce a more accurate result.

Selection Bias – Our analysis in Section 4.3 demonstrates the techniques we can use to study LFBOTs now that we have obtained a larger sample size. Proper statistical analysis and comparisons of transient populations require us to account for observational biases in the construction of our samples. The biases introduced by our requirements that LFBOTs have a visible host galaxy and a radio or X-ray detection are not trivial to remove. We must also do the same for any other transient samples that we compare with the LFBOT sample. Ensuring that a sample is representative is especially difficult for rarer classes of transients. While we did account for some bias in our LFBOT sample in our study on host-galaxy masses, we did not perform any such correction for our analysis of host-galaxy offsets. Representative samples of a variety of transient classes in larger numbers and a broader span of redshifts will be necessary to rigorously perform this type of analysis.

Future Surveys – The development of the Vera C. Rubin Observatory ([Ivezić et al. 2019](#)) and its deep, wide-field optical imaging survey is expected to increase the transient discovery rate by orders of magnitude. This

would cause the number of known LFBOTs to increase significantly, paving the way for more robust and rigorous analysis. The results presented in this paper inform how to best handle each new LFBOT discovery and serve as a blueprint for statistical analysis of an expanded LFBOT sample. Furthermore, Rubin data, along with the advent of high-cadence wide-field UV surveys such as the Ultraviolet Transient Astronomy Satellite (ULTRASAT; Shvartzvald et al. 2024) and the Ultraviolet Explorer (UVEX; Kulkarni et al. 2021), will enable LFBOTs to be identified and followed up much earlier in their evolution.

6. SUMMARY

We presented multiwavelength data—including optical photometry, optical spectroscopy, *Swift* X-ray observations, and VLA/NOEMA/uGMRT radio observations—of six LFBOTs (AT2022abfc, AT2023fhn, AT2023hkw, AT2023vth, AT2024qfm, and AT2024aehp) at redshifts spanning $z = 0.0747\text{--}0.339$. We identified all of these objects on the basis of fast light-curve evolution in ZTF survey data, and confirmed their similarity to the prototype AT2018cow via radio detections. Five of the six LFBOTs (all except AT2023fhn) are presented here for the first time. Our work increases the known number of LFBOTs by 50%.

The optical light curves of four events fade by 3–4 mag over $t_{\text{rest}} \approx 10$ d, similarly to AT2018cow. A fifth event, AT2024aehp, exhibited a plateau at $M \approx -19$ mag over tens of days, after an initial fast decline. The optical spectra do not show any clear features from the transients themselves, including a spectrum of AT2024aehp during its plateau phase.

The X-ray luminosity of AT2024qfm is among the highest of all LFBOTs to date, at $10^{44} \text{ erg s}^{-1}$ at $t_{\text{rest}} \approx 1$ week. The X-rays also appeared to show a brightening by an order of magnitude over just a few days. *Swift* X-ray observations of the other objects resulted in non-detections that were not deep enough to rule out emission identical to AT2018cow itself. AT2023fhn was detected by Chandra at similar levels to AT2018cow (Chrimes et al. 2024b; Nayana et al. 2025).

The 10 GHz radio light curves peak at $t_{\text{rest}} \approx 50\text{--}100$ d, with peak luminosities primarily in the range of $10^{39}\text{--}10^{40} \text{ erg s}^{-1}$. During the rise, the emission appears to be self-absorbed, confirmed by multi-band VLA observations for all objects, as well as by NOEMA 100 GHz detections for AT2024qfm and AT2023vth. We measured basic shock parameters using a simple equipartition analysis, and found—as for previous LFBOTs—fast but sub-relativistic shock speeds. The exception to the radio behavior is AT2024aehp, which, starting

at $t_{\text{rest}} \approx 70$ d, displayed rapid brightening. This late-time brightening is reminiscent of TDEs. Observations of AT2024aehp are ongoing, and will be presented in future work.

For all objects, we measured the offset of the transient position from the host-galaxy nucleus, as well as the basic host-galaxy properties (e.g., stellar mass, star formation rate or SFR). Combining our results with all literature objects, for a total sample of 13 objects, we find that the offset distribution appears intermediate to CCSNe and SLSNe. We find that the host galaxy masses and SFRs trace the full CCSN sequence, and that—even correcting for the fact that we are biased towards detecting LFBOTs in higher-mass galaxies, due to our requirement of a host-galaxy detection—the intrinsic mass distribution appears to be consistent with both SLSNe and CCSNe.

The similar radio light curves imply a similar circum-burst medium for LFBOTs, and therefore a progenitor scenario that can produce a consistent medium timed with the terminal event, such as the merger of a massive star with a compact object. This argument was made when the sample size of LFBOTs was much smaller (Metzger 2022), but here we confirm it with a much larger number of events.

Future LFBOT studies would benefit from longer-term optical monitoring (to confirm or rule out the presence of a plateau as observed in AT2024aehp), deeper X-ray observations (i.e., with *Chandra*), and selection in other bands of the electromagnetic spectrum to mitigate some of the biases present here. Deep optical imaging from the Rubin Observatory, as well as high-cadence UV surveys such as ULTRASAT, will enable LFBOTs to be discovered and followed up much earlier in their evolution.

7. ACKNOWLEDGEMENTS

We thank Dusán Tubín for assistance using the eROSITA upper limit service; Ryan Chornock for providing a AT2024qfm LRIS spectrum; and Raffaella Margutti and Joe Bright for useful discussions.

C.S. and A.Y.Q.H. acknowledge support in part from National Aeronautics and Space Administration (NASA) grant 80NSSC24K0377, an LSST Scialog Early Science grant from the Research Corporation for Science Advancement, and *Hubble Space Telescope* (*HST*) grant HST-GO-17477.006-A. M.W.C. acknowledges support from the U.S. National Science Foundation (NSF) with grant numbers PHY-2409481, PHY-2308862, and PHY-2117997. A.V.F.’s group at UC Berkeley received financial assistance from the Christopher R. Redlich Fund, as well as donations from Gary and Cynthia Bengier,

Clark and Sharon Winslow, Alan Eustace and Kathy Kwan, William Draper, Timothy and Melissa Draper, Briggs and Kathleen Wood, Sanford Robertson (W.Z. is a Bengier-Winslow-Eustace Specialist in Astronomy, T.G.B. is a Draper-Wood-Robertson Specialist in Astronomy, Y.Y. was a Bengier-Winslow-Robertson Fellow in Astronomy), and numerous other donors. A.G.Y.'s research is supported by ISF, IMOS and BSF grants, as well as the André Deloro Institute for Space and Optics Research, the Center for Experimental Physics, a WIS-MIT Sagol grant, the Norman E Alexander Family M Foundation ULTRASAT Data Center Fund, and Yeda-Sela; A.G.Y. is the incumbent of the The Arlyn Imberman Professorial Chair. C.L. is supported by DoE award # DE-SC0025599. B.M. is supported in part by the National Science Foundation under grant number AST-2508620. N.R. is supported by a Northwestern University Presidential Fellowship Award. Zwicky Transient Facility and MMT Observatory access for N.R. was supported by Northwestern University and the Center for Interdisciplinary Exploration and Research in Astrophysics (CIERA). This work is supported by the U.S. NSF under Cooperative Agreement PHY-2019786 (The NSF AI Institute for Artificial Intelligence and Fundamental Interactions; <http://iaifi.org/>).

We thank the staff of the various observatories at which data were obtained.

Based in part on observations obtained with the Samuel Oschin Telescope 48-inch and the 60-inch Telescope at the Palomar Observatory as part of the Zwicky Transient Facility project. ZTF is supported by the National Science Foundation under Grants No. AST-1440341, AST-2034437, and currently Award #2407588. ZTF receives additional funding from the ZTF partnership. Current members include Caltech, USA; Caltech/IPAC, USA; University of Maryland, USA; University of California, Berkeley, USA; University of Wisconsin at Milwaukee, USA; Cornell University, USA; Drexel University, USA; University of North Carolina at Chapel Hill, USA; Institute of Science and Technology, Austria; National Central University, Taiwan, and OKC, University of Stockholm, Sweden. Operations are conducted by Caltech's Optical Observatory (COO), Caltech/IPAC, and the University of Washington at Seattle, USA.

SED Machine is based upon work supported by the National Science Foundation under Grant No. 1106171.

Some of the data presented herein were obtained at W. M. Keck Observatory, which is a private 501(c)3 non-profit organization operated as a scientific partnership among the California Institute of Technology, the University of California, and NASA. The Observatory was made possible by the generous financial support of the

W. M. Keck Foundation. This research has made use of the Keck Observatory Archive (KOA), which is operated by the W. M. Keck Observatory and the NASA Exoplanet Science Institute (NExSci), under contract with NASA. This work was enabled by observations made from the Gemini North telescope, located within the Maunakea Science Reserve and adjacent to the summit of Maunakea. We are grateful for the privilege of observing the Universe from a place that is unique in both its astronomical quality and its cultural significance. The authors wish to recognize and acknowledge the very significant cultural role and reverence that the summit of Maunakea has always had within the indigenous Hawaiian community. We are most fortunate to have the opportunity to conduct observations from this mountain.

This research has made use of the NASA/IPAC Extragalactic Database (NED), which is funded by NASA and operated by the California Institute of Technology, as well as data and software provided by the High Energy Astrophysics Science Archive Research Center (HEASARC), which is a service of the Astrophysics Science Division at NASA/GSFC.

The Liverpool Telescope is operated on the island of La Palma by Liverpool John Moores University in the Spanish Observatorio del Roque de los Muchachos of the Instituto de Astrofísica de Canarias with financial support from the UK Science and Technology Facilities Council.

Observations reported here were obtained in part at the MMT Observatory, a joint facility of the Smithsonian Institution and the University of Arizona. Based in part on observations made with the Nordic Optical Telescope, owned in collaboration by the University of Turku and Aarhus University, and operated jointly by Aarhus University, the University of Turku and the University of Oslo, representing Denmark, Finland and Norway, the University of Iceland and Stockholm University at the Observatorio del Roque de los Muchachos, La Palma, Spain, of the Instituto de Astrofísica de Canarias. The NOT data were obtained under program ID P68-501.

These results made use of the Lowell Discovery Telescope (LDT) at Lowell Observatory. Lowell is a private, nonprofit institution dedicated to astrophysical research and public appreciation of astronomy and operates the LDT in partnership with Boston University, the University of Maryland, the University of Toledo, Northern Arizona University and Yale University. The Large Monolithic Imager was built by Lowell Observatory using funds provided by the U.S. NSF (AST-1005313). This paper includes data gathered with the 6.5 m Magellan Telescopes located at Las Campanas Observatory, Chile. Based in part on observations ob-

tained at the Southern Astrophysical Research (SOAR) telescope, which is a joint project of the Ministério da Ciência, Tecnologia e Inovações (MCTI/LNA) do Brasil, the U.S. NSF's NOIRLab, the University of North Carolina at Chapel Hill (UNC), and Michigan State University (MSU).

Based in part on observations processed using DRAGONS (Data Reduction for Astronomy from Gemini Observatory North and South), obtained at the international Gemini Observatory, program of NSF NOIRLab, which is managed by the Association of Universities for Research in Astronomy (AURA) under a cooperative agreement with the U.S. NSF on behalf of the Gemini Observatory partnership: the U.S. NSF (United States), National Research Council (Canada), Agencia Nacional de Investigación y Desarrollo (Chile), Ministerio de Ciencia, Tecnología e Innovación (Argentina), Ministério da Ciência, Tecnologia, Inovações e Comunicações (Brazil), and Korea Astronomy and Space Science Institute (Republic of Korea).

The National Radio Astronomy Observatory is a facility of the U.S. NSF operated under cooperative agreement by Associated Universities, Inc. This work is based on observations carried out under project numbers D24AA, W22BT and S23BF with the IRAM NOEMA Interferometer. IRAM is supported by INSU/CNRS (France), MPG (Germany) and IGN (Spain). GMRT is run by the National Centre for Radio Astrophysics of the Tata Institute of Fundamental Research.

We acknowledge the use of public data from the *Swift* data archive. This research is based on observations made with the *Galaxy Evolution Explorer* and the *Neil Gehrels Swift Observatory*, obtained from the MAST data archive at the Space Telescope Science Institute, which is operated by the Association of Universities for Research in Astronomy, Inc., under NASA contract NAS 5-26555.

The Pan-STARRS1 Surveys (PS1) and the PS1 public science archive have been made possible through contributions by the Institute for Astronomy, the University of Hawaii, the Pan-STARRS Project Office, the Max-Planck Society and its participating institutes, the Max Planck Institute for Astronomy, Heidelberg and the Max Planck Institute for Extraterrestrial Physics, Garching, The Johns Hopkins University, Durham University, the University of Edinburgh, the Queen's University Belfast, the Harvard-Smithsonian Center for Astrophysics, the Las Cumbres Observatory Global Telescope Network Incorporated, the National Central University of Taiwan, the Space Telescope Science Institute, NASA under grant #NNX08AR22G issued through the Planetary Science Division of the NASA Science Mission Di-

rectorate, NSF grant AST-1238877, the University of Maryland, Eotvos Lorand University (ELTE), the Los Alamos National Laboratory, and the Gordon and Betty Moore Foundation.

The Legacy Surveys consist of three individual and complementary projects: the Dark Energy Camera Legacy Survey (DECaLS; Proposal ID #2014B-0404; PIs D. Schlegel and A. Dey), the Beijing-Arizona Sky Survey (BASS; NOAO Prop. ID #2015A-0801; PIs Zhou Xu and Xiaohui Fan), and the Mayall z-band Legacy Survey (MzLS; Prop. ID #2016A-0453; PI A. Dey). DECaLS, BASS and MzLS together include data obtained, respectively, at the Blanco telescope, Cerro Tololo Inter-American Observatory, NSF's NOIRLab; the Bok telescope, Steward Observatory, University of Arizona; and the Mayall telescope, Kitt Peak National Observatory, NOIRLab. Pipeline processing and analyses of the data were supported by NOIRLab and the Lawrence Berkeley National Laboratory (LBNL). The Legacy Surveys project is honored to be permitted to conduct astronomical research on Iolkam Du'ag (Kitt Peak), a mountain with particular significance to the Tohono O'odham Nation.

NOIRLab is operated by the Association of Universities for Research in Astronomy (AURA) under a cooperative agreement with the U.S. LBNL is managed by the Regents of the University of California under contract to the U.S. Department of Energy.

This project used data obtained with the Dark Energy Camera (DECam), which was constructed by the Dark Energy Survey (DES) collaboration. Funding for the DES Projects has been provided by the U.S. Department of Energy, the U.S. NSF, the Ministry of Science and Education of Spain, the Science and Technology Facilities Council of the United Kingdom, the Higher Education Funding Council for England, the National Center for Supercomputing Applications at the University of Illinois at Urbana-Champaign, the Kavli Institute of Cosmological Physics at the University of Chicago, Center for Cosmology and Astro-Particle Physics at the Ohio State University, the Mitchell Institute for Fundamental Physics and Astronomy at Texas A&M University, Financiadora de Estudos e Projetos, Fundacao Carlos Chagas Filho de Amparo, Financiadora de Estudos e Projetos, Fundacao Carlos Chagas Filho de Amparo a Pesquisa do Estado do Rio de Janeiro, Conselho Nacional de Desenvolvimento Cientifico e Tecnologico and the Ministerio da Ciencia, Tecnologia e Inovacao, the Deutsche Forschungsgemeinschaft and the Collaborating Institutions in the Dark Energy Survey. The Collaborating Institutions are Argonne National Laboratory, the University of California at Santa Cruz, the Univer-

sity of Cambridge, Centro de Investigaciones Energeticas, Medioambientales y Tecnologicas-Madrid, the University of Chicago, University College London, the DES-Brazil Consortium, the University of Edinburgh, the Eidgenossische Technische Hochschule (ETH) Zurich, Fermi National Accelerator Laboratory, the University of Illinois at Urbana-Champaign, the Institut de Ciències de l'Espai (IEEC/CSIC), the Institut de Fisica d'Altes Energies, Lawrence Berkeley National Laboratory, the Ludwig Maximilians Universitat Munchen and the associated Excellence Cluster Universe, the University of Michigan, NSF's NOIRLab, the University of Nottingham, the Ohio State University, the University of Pennsylvania, the University of Portsmouth, SLAC National Accelerator Laboratory, Stanford University, the University of Sussex, and Texas A&M University.

BASS is a key project of the Telescope Access Program (TAP), which has been funded by the National Astronomical Observatories of China, the Chinese Academy of Sciences (the Strategic Priority Research Program “The Emergence of Cosmological Structures” Grant # XDB09000000), and the Special Fund for Astronomy from the Ministry of Finance. The BASS is also supported by the External Cooperation Program of Chinese Academy of Sciences (Grant # 114A11KYSB20160057), and Chinese National Natural Science Foundation (grant #12120101003, #11433005).

The Legacy Surveys imaging of the DESI footprint is supported by the Director, Office of Science, Office of High Energy Physics of the U.S. Department of Energy under Contract No. DE-AC02-05CH1123, by the National Energy Research Scientific Computing Center, a DOE Office of Science User Facility under the same

contract; and by the U.S. NSF, Division of Astronomical Sciences under Contract No. AST-0950945 to NOAO.

This publication makes use of data products from the *Near-Earth Object Wide-field Infrared Survey Explorer (NEOWISE)*, which is a joint project of the Jet Propulsion Laboratory/California Institute of Technology and the University of California, Los Angeles. *NEOWISE* is funded by NASA.

This work is based on data from eROSITA, the soft X-ray instrument aboard SRG, a joint Russian-German science mission supported by the Russian Space Agency (Roskosmos), in the interests of the Russian Academy of Sciences represented by its Space Research Institute (IKI), and the Deutsches Zentrum für Luft- und Raumfahrt (DLR). The SRG spacecraft was built by Lavochkin Association (NPOL) and its subcontractors, and is operated by NPOL with support from the Max Planck Institute for Extraterrestrial Physics (MPE). The development and construction of the eROSITA X-ray instrument was led by MPE, with contributions from the Dr. Karl Remeis Observatory Bamberg & ECAP (FAU Erlangen-Nuernberg), the University of Hamburg Observatory, the Leibniz Institute for Astrophysics Potsdam (AIP), and the Institute for Astronomy and Astrophysics of the University of Tübingen, with the support of DLR and the Max Planck Society. The Argelander Institute for Astronomy of the University of Bonn and the Ludwig Maximilians Universität Munich also participated in the science preparation for eROSITA.

Facilities: Blanco (DECaLS), Bok (BASS), DCT (LMI), GALEX, Gemini:North, Gemini:South, GMRT, IRAM:NOEMA, Keck:I (LRIS), Keck:II (KCWI, DEIMOS), Liverpool:2m, Magellan:Baade (IMACS), Mayall (MzLS), MMT (Binospec), NOT (ALFOSC), PO:1.2m, PO:1.5m, Sloan, SOAR (GHTS), Swift, VLA, NEOWISE

REFERENCES

Andreoni, I., Coughlin, M. W., Kool, E. C., et al. 2021, ApJ, 918, 63, doi: [10.3847/1538-4357/ac0bc7](https://doi.org/10.3847/1538-4357/ac0bc7)

Bellm, E. C., Kulkarni, S. R., Graham, M. J., et al. 2019, PASP, 131, 018002, doi: [10.1088/1538-3873/aaecbe](https://doi.org/10.1088/1538-3873/aaecbe)

Berger, E., Kulkarni, S. R., Pooley, G., et al. 2003, Nature, 426, 154, doi: [10.1038/nature01998](https://doi.org/10.1038/nature01998)

Bhandari, S., Heintz, K. E., Aggarwal, K., et al. 2022, AJ, 163, 69, doi: [10.3847/1538-3881/ac3aec](https://doi.org/10.3847/1538-3881/ac3aec)

Bida, T. A., Dunham, E. W., Massey, P., & Roe, H. G. 2014, in Society of Photo-Optical Instrumentation Engineers (SPIE) Conference Series, Vol. 9147, Ground-based and Airborne Instrumentation for Astronomy V, ed. S. K. Ramsay, I. S. McLean, & H. Takami, 91472N, doi: [10.1117/12.2056872](https://doi.org/10.1117/12.2056872)

Bietenholz, M. F., Bartel, N., Argo, M., et al. 2021, ApJ, 908, 75, doi: [10.3847/1538-4357/abcccd9](https://doi.org/10.3847/1538-4357/abcccd9)

Blagorodnova, N., Gezari, S., Hung, T., et al. 2017, ApJ, 844, 46, doi: [10.3847/1538-4357/aa7579](https://doi.org/10.3847/1538-4357/aa7579)

Blagorodnova, N., Neill, J. D., Walters, R., et al. 2018, PASP, 130, 035003, doi: [10.1088/1538-3873/aaa53f](https://doi.org/10.1088/1538-3873/aaa53f)

Blanchard, P. K., Berger, E., & Fong, W.-f. 2016, *ApJ*, 817, 144, doi: [10.3847/0004-637X/817/2/144](https://doi.org/10.3847/0004-637X/817/2/144)

Briggs, D. S. 1995, PhD thesis, New Mexico Institute of Mining and Technology

Bright, J. S., Margutti, R., Matthews, D., et al. 2022, *ApJ*, 926, 112, doi: [10.3847/1538-4357/ac4506](https://doi.org/10.3847/1538-4357/ac4506)

Burrows, D. N., Hill, J. E., Nousek, J. A., et al. 2005, *SSRv*, 120, 165, doi: [10.1007/s11214-005-5097-2](https://doi.org/10.1007/s11214-005-5097-2)

Calzetti, D., Armus, L., Bohlin, R. C., et al. 2000, *ApJ*, 533, 682, doi: [10.1086/308692](https://doi.org/10.1086/308692)

Campana, S., Mangano, V., Blustin, A. J., et al. 2006, *Nature*, 442, 1008, doi: [10.1038/nature04892](https://doi.org/10.1038/nature04892)

Cendes, Y., Berger, E., Alexander, K. D., et al. 2024, *ApJ*, 971, 185, doi: [10.3847/1538-4357/ad5541](https://doi.org/10.3847/1538-4357/ad5541)

Cenko, S. B., Fox, D. B., Moon, D.-S., et al. 2006, *PASP*, 118, 1396, doi: [10.1086/508366](https://doi.org/10.1086/508366)

Chabrier, G. 2003, *PASP*, 115, 763, doi: [10.1086/376392](https://doi.org/10.1086/376392)

Chambers, K. C., Magnier, E. A., Metcalfe, N., et al. 2016, arXiv e-prints, arXiv:1612.05560, doi: [10.48550/arXiv.1612.05560](https://doi.org/10.48550/arXiv.1612.05560)

Chevalier, R. A. 1998, *ApJ*, 499, 810, doi: [10.1086/305676](https://doi.org/10.1086/305676)

Chevalier, R. A., & Fransson, C. 2006, *ApJ*, 651, 381, doi: [10.1086/507606](https://doi.org/10.1086/507606)

Chrimes, A., Jonker, P., Levan, A., Coppejans, D., & Malesani, D. B. 2023, Transient Name Server AstroNote, 105, 1

Chrimes, A. A., Coppejans, D. L., Jonker, P. G., et al. 2024a, *A&A*, 691, A329, doi: [10.1051/0004-6361/202451172](https://doi.org/10.1051/0004-6361/202451172)

Chrimes, A. A., Jonker, P. G., Levan, A. J., & Mummery, A. 2025, arXiv e-prints, arXiv:2510.03402, doi: [10.48550/arXiv.2510.03402](https://doi.org/10.48550/arXiv.2510.03402)

Chrimes, A. A., Jonker, P. G., Levan, A. J., et al. 2024b, *MNRAS*, 527, L47, doi: [10.1093/mnrasl/slad145](https://doi.org/10.1093/mnrasl/slad145)

Clemens, J. C., Crain, J. A., & Anderson, R. 2004, in Society of Photo-Optical Instrumentation Engineers (SPIE) Conference Series, Vol. 5492, Ground-based Instrumentation for Astronomy, ed. A. F. M. Moorwood & M. Iye, 331–340, doi: [10.1117/12.550069](https://doi.org/10.1117/12.550069)

Comrie, A., Wang, K.-S., Hsu, S.-C., et al. 2021, CARTA: The Cube Analysis and Rendering Tool for Astronomy, 2.0.0, Zenodo, doi: [10.5281/zenodo.3377984](https://doi.org/10.5281/zenodo.3377984)

Coppejans, D. L., Margutti, R., Terreran, G., et al. 2020, *ApJL*, 895, L23, doi: [10.3847/2041-8213/ab8cc7](https://doi.org/10.3847/2041-8213/ab8cc7)

Corsi, A., Ofek, E. O., Gal-Yam, A., et al. 2014, *ApJ*, 782, 42, doi: [10.1088/0004-637X/782/1/42](https://doi.org/10.1088/0004-637X/782/1/42)

Coughlin, M. W., Bloom, J. S., Nir, G., et al. 2023, *ApJS*, 267, 31, doi: [10.3847/1538-4365/acdee1](https://doi.org/10.3847/1538-4365/acdee1)

De, K., Kasliwal, M. M., Tzanidakis, A., et al. 2020, *ApJ*, 905, 58, doi: [10.3847/1538-4357/abb45c](https://doi.org/10.3847/1538-4357/abb45c)

Dekany, R., Smith, R. M., Riddle, R., et al. 2020, *PASP*, 132, 038001, doi: [10.1088/1538-3873/ab4ca2](https://doi.org/10.1088/1538-3873/ab4ca2)

Dey, A., Schlegel, D. J., Lang, D., et al. 2019, *AJ*, 157, 168, doi: [10.3847/1538-3881/ab089d](https://doi.org/10.3847/1538-3881/ab089d)

Djupvik, A. A., & Andersen, J. 2010, in *Astrophysics and Space Science Proceedings*, Vol. 14, Highlights of Spanish Astrophysics V, ed. J. M. Diego, L. J. Goicoechea, J. I. González-Serrano, & J. Gorgas, 211, doi: [10.1007/978-3-642-11250-8_21](https://doi.org/10.1007/978-3-642-11250-8_21)

Dressler, A. 2010, Enhanced Performance for the IMACS F/4 Camera Upgrade, NSF Award Number 1038894. Directorate for Mathematical and Physical Sciences, Division Of Astronomical Sciences. 2010.

Drout, M. R., Chornock, R., Soderberg, A. M., et al. 2014, *ApJ*, 794, 23, doi: [10.1088/0004-637X/794/1/23](https://doi.org/10.1088/0004-637X/794/1/23)

Duev, D. A., Mahabal, A., Masci, F. J., et al. 2019, *MNRAS*, 489, 3582, doi: [10.1093/mnras/stz2357](https://doi.org/10.1093/mnras/stz2357)

Evans, C. R., & Kochanek, C. S. 1989, *ApJL*, 346, L13, doi: [10.1086/185567](https://doi.org/10.1086/185567)

Faber, S. M., Phillips, A. C., Kibrick, R. I., et al. 2003, in Society of Photo-Optical Instrumentation Engineers (SPIE) Conference Series, Vol. 4841, Instrument Design and Performance for Optical/Infrared Ground-based Telescopes, ed. M. Iye & A. F. M. Moorwood, 1657–1669, doi: [10.1117/12.460346](https://doi.org/10.1117/12.460346)

Fabricant, D., Fata, R., Epps, H., et al. 2019, *Publications of the Astronomical Society of the Pacific*, 131, 075004, doi: [10.1088/1538-3873/ab1d78](https://doi.org/10.1088/1538-3873/ab1d78)

Ferguson, R., & Margalit, B. 2025, arXiv e-prints, arXiv:2509.16313, doi: [10.48550/arXiv.2509.16313](https://doi.org/10.48550/arXiv.2509.16313)

Fong, W.-f., Nugent, A. E., Dong, Y., et al. 2022, *ApJ*, 940, 56, doi: [10.3847/1538-4357/ac91d0](https://doi.org/10.3847/1538-4357/ac91d0)

Forster, F., Bauer, F. E., Pignata, G., et al. 2024, Transient Name Server Discovery Report, 2024-2624, 1

Fremling, C. 2022, Transient Name Server Discovery Report, 2022-3387, 1

—. 2023a, Transient Name Server Discovery Report, 2023-775, 1

—. 2023b, Transient Name Server Discovery Report, 2023-981, 1

—. 2023c, Transient Name Server Discovery Report, 2023-2714, 1

Fulton, M., Chen, T. W., Smartt, S. J., et al. 2024, Transient Name Server AstroNote, 206, 1

Gallazzi, A., Charlot, S., Brinchmann, J., White, S. D. M., & Tremonti, C. A. 2005, *MNRAS*, 362, 41, doi: [10.1111/j.1365-2966.2005.09321.x](https://doi.org/10.1111/j.1365-2966.2005.09321.x)

Gehrels, N., Chincarini, G., Giommi, P., et al. 2004, *ApJ*, 611, 1005, doi: [10.1086/422091](https://doi.org/10.1086/422091)

Gildas Team. 2013, GILDAS: Grenoble Image and Line Data Analysis Software, Astrophysics Source Code Library, record ascl:1305.010

Gillanders, J. H., Huber, M., Chambers, K., et al. 2024, Transient Name Server AstroNote, 210, 1

Gimeno, G., Roth, K., Chiboucas, K., et al. 2016, in Society of Photo-Optical Instrumentation Engineers (SPIE) Conference Series, Vol. 9908, Ground-based and Airborne Instrumentation for Astronomy VI, ed. C. J. Evans, L. Simard, & H. Takami, 99082S, doi: [10.1117/12.2233883](https://doi.org/10.1117/12.2233883)

Gottlieb, O., Tchekhovskoy, A., & Margutti, R. 2022, MNRAS, 513, 3810, doi: [10.1093/mnras/stac910](https://doi.org/10.1093/mnras/stac910)

Graham, M. J., Kulkarni, S. R., Bellm, E. C., et al. 2019, PASP, 131, 078001, doi: [10.1088/1538-3873/ab006c](https://doi.org/10.1088/1538-3873/ab006c)

Gutiérrez, C. P., Mattila, S., Lundqvist, P., et al. 2024, ApJ, 977, 162, doi: [10.3847/1538-4357/ad89a5](https://doi.org/10.3847/1538-4357/ad89a5)

Ho, A. Y. Q. 2023a, Transient Name Server AstroNote, 174, 1

—. 2023b, Transient Name Server AstroNote, 173, 1

—. 2023c, Transient Name Server AstroNote, 317, 1

Ho, A. Y. Q., & Bremer, M. 2023, Transient Name Server AstroNote, 318, 1

Ho, A. Y. Q., Liu, C., Andreoni, I., et al. 2023a, Transient Name Server AstroNote, 93, 1

Ho, A. Y. Q., Liu, C., Chen, P., et al. 2022a, Transient Name Server AstroNote, 275, 1

Ho, A. Y. Q., Phinney, E. S., Ravi, V., et al. 2019, ApJ, 871, 73, doi: [10.3847/1538-4357/aaf473](https://doi.org/10.3847/1538-4357/aaf473)

Ho, A. Y. Q., Perley, D. A., Kulkarni, S. R., et al. 2020a, ApJ, 895, 49, doi: [10.3847/1538-4357/ab8bcf](https://doi.org/10.3847/1538-4357/ab8bcf)

Ho, A. Y. Q., Perley, D. A., Beniamini, P., et al. 2020b, ApJ, 905, 98, doi: [10.3847/1538-4357/abc34d](https://doi.org/10.3847/1538-4357/abc34d)

Ho, A. Y. Q., Perley, D. A., Yao, Y., et al. 2022b, ApJ, 938, 85, doi: [10.3847/1538-4357/ac8bd0](https://doi.org/10.3847/1538-4357/ac8bd0)

Ho, A. Y. Q., Margalit, B., Bremer, M., et al. 2022c, ApJ, 932, 116, doi: [10.3847/1538-4357/ac4e97](https://doi.org/10.3847/1538-4357/ac4e97)

Ho, A. Y. Q., Perley, D. A., Gal-Yam, A., et al. 2023b, ApJ, 949, 120, doi: [10.3847/1538-4357/acc533](https://doi.org/10.3847/1538-4357/acc533)

Ho, A. Y. Q., Perley, D. A., Chen, P., et al. 2023c, Nature, 623, 927, doi: [10.1038/s41586-023-06673-6](https://doi.org/10.1038/s41586-023-06673-6)

Hook, I. M., Jørgensen, I., Allington-Smith, J. R., et al. 2004, PASP, 116, 425, doi: [10.1086/383624](https://doi.org/10.1086/383624)

Horesh, A., Cenko, S. B., & Arcavi, I. 2021, Nature Astronomy, 5, 491, doi: [10.1038/s41550-021-01300-8](https://doi.org/10.1038/s41550-021-01300-8)

Inserra, C. 2019, Nature Astronomy, 3, 697, doi: [10.1038/s41550-019-0854-4](https://doi.org/10.1038/s41550-019-0854-4)

Ivezić, Ž., Kahn, S. M., Tyson, J. A., et al. 2019, ApJ, 873, 111, doi: [10.3847/1538-4357/ab042c](https://doi.org/10.3847/1538-4357/ab042c)

Johnson, B. D., Leja, J., Conroy, C., & Speagle, J. S. 2021, ApJS, 254, 22, doi: [10.3847/1538-4365/abef67](https://doi.org/10.3847/1538-4365/abef67)

Kansky, J., Chilingarian, I., Fabricant, D., et al. 2019, PASP, 131, 075005, doi: [10.1088/1538-3873/ab1ceb](https://doi.org/10.1088/1538-3873/ab1ceb)

Kelly, P. L., & Kirshner, R. P. 2012, ApJ, 759, 107, doi: [10.1088/0004-637X/759/2/107](https://doi.org/10.1088/0004-637X/759/2/107)

Kim, Y.-L., Rigault, M., Neill, J. D., et al. 2022, PASP, 134, 024505, doi: [10.1088/1538-3873/ac50a0](https://doi.org/10.1088/1538-3873/ac50a0)

Klencki, J., & Metzger, B. D. 2025, arXiv e-prints, arXiv:2510.09745, doi: [10.48550/arXiv.2510.09745](https://doi.org/10.48550/arXiv.2510.09745)

Kraft, R. P., Burrows, D. N., & Nousek, J. A. 1991, ApJ, 374, 344, doi: [10.1086/170124](https://doi.org/10.1086/170124)

Kremer, K., Lu, W., Piro, A. L., et al. 2021, ApJ, 911, 104, doi: [10.3847/1538-4357/abeb14](https://doi.org/10.3847/1538-4357/abeb14)

Kremer, K., Mockler, B., Piro, A. L., & Lombardi, J. C. 2023, MNRAS, 524, 6358, doi: [10.1093/mnras/stad2239](https://doi.org/10.1093/mnras/stad2239)

Kuin, N. P. M., Wu, K., Oates, S., et al. 2019, MNRAS, 487, 2505, doi: [10.1093/mnras/stz053](https://doi.org/10.1093/mnras/stz053)

Kulkarni, S. R., Frail, D. A., Wieringa, M. H., et al. 1998, Nature, 395, 663, doi: [10.1038/27139](https://doi.org/10.1038/27139)

Kulkarni, S. R., Harrison, F. A., Grefenstette, B. W., et al. 2021, arXiv e-prints, arXiv:2111.15608, doi: [10.48550/arXiv.2111.15608](https://doi.org/10.48550/arXiv.2111.15608)

Labrie, K., Simpson, C., Cardenes, R., et al. 2023, Research Notes of the American Astronomical Society, 7, 214, doi: [10.3847/2515-5172/ad0044](https://doi.org/10.3847/2515-5172/ad0044)

Laskar, T., Alexander, K. D., & Berger, E. 2016, GRB Coordinates Network, 20328, 1

Laskar, T., Berger, E., Chornock, R., et al. 2018, GRB Coordinates Network, 23519, 1

LeBaron, N., Margutti, R., Chornock, R., et al. 2025, arXiv e-prints, arXiv:2509.00951, doi: [10.48550/arXiv.2509.00951](https://doi.org/10.48550/arXiv.2509.00951)

Leja, J., Johnson, B. D., Conroy, C., van Dokkum, P. G., & Byler, N. 2017, ApJ, 837, 170, doi: [10.3847/1538-4357/aa5ffe](https://doi.org/10.3847/1538-4357/aa5ffe)

Li, M. L., Ho, A. Y. Q., Filippenko, A. V., et al. 2023, Transient Name Server AstroNote, 114, 1

Lunnan, R., Chornock, R., Berger, E., et al. 2015, ApJ, 804, 90, doi: [10.1088/0004-637X/804/2/90](https://doi.org/10.1088/0004-637X/804/2/90)

Lyman, J. D., Levan, A. J., Tanvir, N. R., et al. 2017, MNRAS, 467, 1795, doi: [10.1093/mnras/stx220](https://doi.org/10.1093/mnras/stx220)

Mahabal, A., Rebba Pragada, U., Walters, R., et al. 2019, PASP, 131, 038002, doi: [10.1088/1538-3873/aaf3fa](https://doi.org/10.1088/1538-3873/aaf3fa)

Mainzer, A., Bauer, J., Grav, T., et al. 2011, ApJ, 731, 53, doi: [10.1088/0004-637X/731/1/53](https://doi.org/10.1088/0004-637X/731/1/53)

Mandigo-Stoba, M. S., Fremling, C., & Kasliwal, M. 2022, The Journal of Open Source Software, 7, 3612, doi: [10.21105/joss.03612](https://doi.org/10.21105/joss.03612)

Margalit, B., & Quataert, E. 2021, ApJL, 923, L14, doi: [10.3847/2041-8213/ac3d97](https://doi.org/10.3847/2041-8213/ac3d97)

—. 2024, ApJ, 977, 134, doi: [10.3847/1538-4357/ad8b47](https://doi.org/10.3847/1538-4357/ad8b47)

Margutti, R., Nayana, A. J., & Sears, H. 2024, The Astronomer's Telegram, 16748, 1

Margutti, R., Metzger, B. D., Chornock, R., et al. 2019, ApJ, 872, 18, doi: [10.3847/1538-4357/aafa01](https://doi.org/10.3847/1538-4357/aafa01)

Martin, D. C., Fanson, J., Schiminovich, D., et al. 2005, ApJL, 619, L1, doi: [10.1086/426387](https://doi.org/10.1086/426387)

Masci, F. J., Laher, R. R., Rusholme, B., et al. 2019, PASP, 131, 018003, doi: [10.1088/1538-3873/aae8ac](https://doi.org/10.1088/1538-3873/aae8ac)

Matthews, D., Margutti, R., Metzger, B. D., et al. 2023, Research Notes of the American Astronomical Society, 7, 126, doi: [10.3847/2515-5172/acdde1](https://doi.org/10.3847/2515-5172/acdde1)

Merloni, A., Lamer, G., Liu, T., et al. 2024, A&A, 682, A34, doi: [10.1051/0004-6361/202347165](https://doi.org/10.1051/0004-6361/202347165)

Metzger, B. D. 2022, ApJ, 932, 84, doi: [10.3847/1538-4357/ac6d59](https://doi.org/10.3847/1538-4357/ac6d59)

Million, C., Fleming, S. W., Shiao, B., et al. 2016, ApJ, 833, 292, doi: [10.3847/1538-4357/833/2/292](https://doi.org/10.3847/1538-4357/833/2/292)

Morrissey, P., Matuszewski, M., Martin, D. C., et al. 2018, ApJ, 864, 93, doi: [10.3847/1538-4357/aad597](https://doi.org/10.3847/1538-4357/aad597)

Munoz-Arcibia, A., Pignata, G., Bauer, F. E., et al. 2024, Transient Name Server Discovery Report, 2024-4959, 1

Nayana, A. J., Margutti, R., Wiston, E., et al. 2025, arXiv e-prints, arXiv:2509.00952, doi: [10.48550/arXiv.2509.00952](https://doi.org/10.48550/arXiv.2509.00952)

Ofek, E. O., Rabinak, I., Neill, J. D., et al. 2010, ApJ, 724, 1396, doi: [10.1088/0004-637X/724/2/1396](https://doi.org/10.1088/0004-637X/724/2/1396)

Oke, J. B., & Gunn, J. E. 1982, PASP, 94, 586, doi: [10.1086/131027](https://doi.org/10.1086/131027)

—. 1983, ApJ, 266, 713, doi: [10.1086/160817](https://doi.org/10.1086/160817)

Oke, J. B., Cohen, J. G., Carr, M., et al. 1995, PASP, 107, 375, doi: [10.1086/133562](https://doi.org/10.1086/133562)

Patterson, M. T., Bellm, E. C., Rusholme, B., et al. 2019, PASP, 131, 018001, doi: [10.1088/1538-3873/aae904](https://doi.org/10.1088/1538-3873/aae904)

Perley, D. 2023, in American Astronomical Society Meeting Abstracts, Vol. 241, American Astronomical Society Meeting Abstracts, 252.05

Perley, D. A. 2013, GRB Coordinates Network, 14494, 1

—. 2019, PASP, 131, 084503, doi: [10.1088/1538-3873/ab215d](https://doi.org/10.1088/1538-3873/ab215d)

Perley, D. A., Schulze, S., & de Ugarte Postigo, A. 2017, GRB Coordinates Network, 22252, 1

Perley, D. A., Mazzali, P. A., Yan, L., et al. 2019, MNRAS, 484, 1031, doi: [10.1093/mnras/sty3420](https://doi.org/10.1093/mnras/sty3420)

Perley, D. A., Ho, A. Y. Q., Yao, Y., et al. 2021, MNRAS, 508, 5138, doi: [10.1093/mnras/stab2785](https://doi.org/10.1093/mnras/stab2785)

Perley, D. A., Ho, A. Y. Q., McGrath, Z., et al. 2026, arXiv e-prints, arXiv:2601.03337. <https://arxiv.org/abs/2601.03337>

Perley, R. A., Chandler, C. J., Butler, B. J., & Wrobel, J. M. 2011, ApJL, 739, L1, doi: [10.1088/2041-8205/739/1/L1](https://doi.org/10.1088/2041-8205/739/1/L1)

Pian, E., Amati, L., Antonelli, L. A., et al. 2000, ApJ, 536, 778, doi: [10.1086/308978](https://doi.org/10.1086/308978)

Planck Collaboration, Aghanim, N., Akrami, Y., et al. 2020, A&A, 641, A6, doi: [10.1051/0004-6361/201833910](https://doi.org/10.1051/0004-6361/201833910)

Predehl, P., Andritschke, R., Arefiev, V., et al. 2021, A&A, 647, A1, doi: [10.1051/0004-6361/202039313](https://doi.org/10.1051/0004-6361/202039313)

Prentice, S. J., Maguire, K., Smartt, S. J., et al. 2018, ApJL, 865, L3, doi: [10.3847/2041-8213/aadd90](https://doi.org/10.3847/2041-8213/aadd90)

Prochaska, J. X., Hennawi, J. F., Westfall, K. B., et al. 2020, Journal of Open Source Software, 5, 2308, doi: [10.21105/joss.02308](https://doi.org/10.21105/joss.02308)

Pursiainen, M., Childress, M., Smith, M., et al. 2018, Monthly Notices of the Royal Astronomical Society, 481, 894, doi: [10.1093/mnras/sty2309](https://doi.org/10.1093/mnras/sty2309)

Pursiainen, M., Killestein, T. L., Kuncarayakti, H., et al. 2025, MNRAS, 537, 3298, doi: [10.1093/mnras/staf232](https://doi.org/10.1093/mnras/staf232)

R Core Team. 2025, R: A Language and Environment for Statistical Computing, R Foundation for Statistical Computing, Vienna, Austria. <https://www.R-project.org/>

Rigault, M., Neill, J. D., Blagorodnova, N., et al. 2019, A&A, 627, A115, doi: [10.1051/0004-6361/201935344](https://doi.org/10.1051/0004-6361/201935344)

Rivera Sandoval, L. E., Maccarone, T. J., Corsi, A., et al. 2018, MNRAS, 480, L146, doi: [10.1093/mnrasl/sly145](https://doi.org/10.1093/mnrasl/sly145)

Roming, P. W. A., Kennedy, T. E., Mason, K. O., et al. 2005, SSRv, 120, 95, doi: [10.1007/s11214-005-5095-4](https://doi.org/10.1007/s11214-005-5095-4)

Roux de Bezieux, H. 2024, Ecume: Equality of 2 (or k) Continuous Univariate and Multivariate Distributions, doi: [10.32614/CRAN.package.Ecume](https://doi.org/10.32614/CRAN.package.Ecume)

Salas, P., Bauer, F. E., Stockdale, C., & Prieto, J. L. 2013, MNRAS, 428, 1207, doi: [10.1093/mnras/sts104](https://doi.org/10.1093/mnras/sts104)

Schlafly, E. F., & Finkbeiner, D. P. 2011, ApJ, 737, 103, doi: [10.1088/0004-637X/737/2/103](https://doi.org/10.1088/0004-637X/737/2/103)

Schroeder, G., Chen, P., Sollerman, J., et al. 2025, Transient Name Server AstroNote, 3, 1

Schroeder, G., & Ho, A. Y. Q. 2025, Transient Name Server AstroNote, 99, 1

Schulze, S., Yaron, O., Sollerman, J., et al. 2021, ApJS, 255, 29, doi: [10.3847/1538-4365/abff5e](https://doi.org/10.3847/1538-4365/abff5e)

Sevilla, J., Ho, A. Y. Q., & Srinivasaragavan, G. 2024, Transient Name Server AstroNote, 386, 1

Sevilla, J., Li, M. L., & Ho, A. Y. Q. 2023, Transient Name Server AstroNote, 297, 1

Shoval, N., Horesh, A., Hughes, A., et al. 2025, Transient Name Server AstroNote, 189, 1

Shvartzvald, Y., Waxman, E., Gal-Yam, A., et al. 2024, ApJ, 964, 74, doi: [10.3847/1538-4357/ad2704](https://doi.org/10.3847/1538-4357/ad2704)

Silverman, J. M., Foley, R. J., Filippenko, A. V., et al. 2012, MNRAS, 425, 1789, doi: [10.1111/j.1365-2966.2012.21270.x](https://doi.org/10.1111/j.1365-2966.2012.21270.x)

Soderberg, A. M., Brunthaler, A., Nakar, E., Chevalier, R. A., & Bietenholz, M. F. 2010a, ApJ, 725, 922, doi: [10.1088/0004-637X/725/1/922](https://doi.org/10.1088/0004-637X/725/1/922)

Soderberg, A. M., Chevalier, R. A., Kulkarni, S. R., & Frail, D. A. 2006a, ApJ, 651, 1005, doi: [10.1086/507571](https://doi.org/10.1086/507571)

Soderberg, A. M., Kulkarni, S. R., Nakar, E., et al. 2006b, Nature, 442, 1014, doi: [10.1038/nature05087](https://doi.org/10.1038/nature05087)

Soderberg, A. M., Chakraborti, S., Pignata, G., et al. 2010b, Nature, 463, 513, doi: [10.1038/nature08714](https://doi.org/10.1038/nature08714)

Somalwar, J. J., Ravi, V., Margutti, R., et al. 2025, arXiv e-prints, arXiv:2505.11597, doi: [10.48550/arXiv.2505.11597](https://doi.org/10.48550/arXiv.2505.11597)

Steele, I. A., Smith, R. J., Rees, P. C., et al. 2004, in Society of Photo-Optical Instrumentation Engineers (SPIE) Conference Series, Vol. 5489, Ground-based Telescopes, ed. J. Oschmann, Jacobus M., 679–692, doi: [10.1117/12.551456](https://doi.org/10.1117/12.551456)

Sunyaev, R., Arefiev, V., Babushkin, V., et al. 2021, A&A, 656, A132, doi: [10.1051/0004-6361/202141179](https://doi.org/10.1051/0004-6361/202141179)

Swarup, G., Ananthakrishnan, S., Kapahi, V. K., et al. 1991, Current Science, 60, 95

Tachibana, Y., & Miller, A. A. 2018, PASP, 130, 128001, doi: [10.1088/1538-3873/aae3d9](https://doi.org/10.1088/1538-3873/aae3d9)

Taggart, K., & Perley, D. A. 2021, MNRAS, 503, 3931, doi: [10.1093/mnras/stab174](https://doi.org/10.1093/mnras/stab174)

Team, T. C., Bean, B., Bhatnagar, S., et al. 2022, Publications of the Astronomical Society of the Pacific, 134, 114501, doi: [10.1088/1538-3873/ac9642](https://doi.org/10.1088/1538-3873/ac9642)

Thompson, A. R., Clark, B. G., Wade, C. M., & Napier, P. J. 1980, ApJS, 44, 151, doi: [10.1086/190688](https://doi.org/10.1086/190688)

Tiengo, A., Mereghetti, S., Ghisellini, G., Tavecchio, F., & Ghirlanda, G. 2004, A&A, 423, 861, doi: [10.1051/0004-6361:20041027](https://doi.org/10.1051/0004-6361:20041027)

Tody, D. 1986, in Society of Photo-Optical Instrumentation Engineers (SPIE) Conference Series, Vol. 627, Instrumentation in astronomy VI, ed. D. L. Crawford, 733, doi: [10.1117/12.968154](https://doi.org/10.1117/12.968154)

Tonry, J. L., Denneau, L., Heinze, A. N., et al. 2018, PASP, 130, 064505, doi: [10.1088/1538-3873/aabadf](https://doi.org/10.1088/1538-3873/aabadf)

Tsuna, D., & Lu, W. 2025, ApJ, 986, 84, doi: [10.3847/1538-4357/addr158](https://doi.org/10.3847/1538-4357/addr158)

Tsuna, D., Wu, S. C., Fuller, J., Dong, Y., & Piro, A. L. 2024, The Open Journal of Astrophysics, 7, 82, doi: [10.33232/001c.123897](https://doi.org/10.33232/001c.123897)

Tubín-Arenas, D., Krumpe, M., Lamer, G., et al. 2024, A&A, 682, A35, doi: [10.1051/0004-6361/202346773](https://doi.org/10.1051/0004-6361/202346773)

van der Horst, A. J., Kamble, A., Resmi, L., et al. 2008, A&A, 480, 35, doi: [10.1051/0004-6361:20078051](https://doi.org/10.1051/0004-6361:20078051)

van der Walt, S., Crellin-Quick, A., & Bloom, J. 2019, The Journal of Open Source Software, 4, 1247, doi: [10.21105/joss.01247](https://doi.org/10.21105/joss.01247)

Wang, X., Wang, L., Filippenko, A. V., Zhang, T., & Zhao, X. 2013, Science, 340, 170, doi: [10.1126/science.1231502](https://doi.org/10.1126/science.1231502)

Yao, Y., Ho, A. Y. Q., Medvedev, P., et al. 2022, ApJ, 934, 104, doi: [10.3847/1538-4357/ac7a41](https://doi.org/10.3847/1538-4357/ac7a41)

Zackay, B., Ofek, E. O., & Gal-Yam, A. 2016, ApJ, 830, 27, doi: [10.3847/0004-637X/830/1/27](https://doi.org/10.3847/0004-637X/830/1/27)

Zauderer, B. A., Berger, E., Soderberg, A. M., et al. 2011, Nature, 476, 425, doi: [10.1038/nature10366](https://doi.org/10.1038/nature10366)

APPENDIX

A. IDENTIFICATION IN ZTF SURVEY DATA

ZTF observations of the six LFBOTs in this paper occurred during Phase II (ZTF-II), which was divided into public (50%), partnership (30%), and Caltech (20%) observing time. ZTF uses three filters: $ztf-g$, $ztf-r$, and $ztf-i$. For comparison with other photometry, we denote these as g , r , and i . ZTF data products are processed by the IPAC ZTF pipeline (Masci et al. 2019), which uses image subtraction following the methods of Zackay et al. (2016). Detections more significant than 5σ are distributed as alerts in the Avro format (Patterson et al. 2019). These alerts are filtered using machine-learning real-bogus metrics (Mahabal et al. 2019; Duev et al. 2019), host-galaxy classifiers (Tachibana & Miller 2018), and inspection of light-curve properties. For ZTF-II, the collaboration used the Fritz marshal (van der Walt et al. 2019; Duev et al. 2019) to coordinate detection, analysis, and follow-up observations of transients. The Fritz marshal uses the open-source software package SkyPortal (Coughlin et al. 2023).

A.1. *AT2022abfc/ZTF22abvrxkk*

AT2022abfc was first detected by ZTF on November 21, 2022 (MJD = 59904.344; Fremling 2022). ZTF non-detections prior to the first observation and ZTF detections over the next five days confirmed a rise faster than 1 mag day^{-1} and a fade rate of 0.2 mag day^{-1} . The transient's fast evolution led to follow-up multiwavelength observations. A Gemini South spectrum²⁸ taken December 1, 2022 showed narrow H α emission and Ca II H&K absorption lines at $z = 0.212$, implying a peak absolute magnitude of -20.7 . A radio follow-up campaign with the VLA²⁹ began with a detection at 10 GHz on December 6 (Ho et al. 2022a). Subsequent radio observations showed a brightening of the radio emission. The transient's fast evolution, high luminosity, and radio emission led to its classification as an LFBOT.

A.2. *AT2023fhn/ZTF23aaezpp*

The discovery narrative for AT2023fhn has already been published by Chrimes et al. (2024b); we reiterate it here for convenience. ZTF first detected AT2023fhn on April 10, 2023 (MJD = 60044.204; Fremling 2023a). Its light curve showed a fast fade of 0.2 mag day^{-1} and blue optical colors ($g - r \approx -0.5 \text{ mag}$). A possible host

galaxy's photometric redshift implied an absolute optical magnitude of $M_g < -20$, motivating follow-up observations. On April 20, a spectrum obtained by the DBSP on the Palomar 5m telescope yielded H α , N II, and S II emission lines at $z = 0.24$, confirming an absolute magnitude of $M_g = -21.5$ (Ho et al. 2023a). The transient was subsequently detected at X-ray and radio wavelengths, respectively by *Chandra* on April 25 (Chrimes et al. 2023) and the VLA (10 GHz) on June 15 (Ho 2023a). The blue colors, fast fading, high luminosity, and detected emission throughout the electromagnetic spectrum confirmed it as an LFBOT. The *Chandra* X-ray detections and a subset of this transient's VLA radio observations are already published by Chrimes et al. (2024a).

A.3. *AT2023hkw/ZTF23aaaimsja*

ZTF first detected AT2023hkw on May 1, 2023 (MJD = 60065.199; Fremling 2023b). The transient was flagged for fast evolution from a rise rate greater than 1 mag day^{-1} and a fade rate of $\sim 0.2 \text{ mag day}^{-1}$. This resulted in follow-up spectroscopy on May 12 using DEMOS at the Keck Observatory³⁰ (Li et al. 2023), using 1440s of exposure time. The spectrum showed narrow H α and [N II] emission lines from the host galaxy at $z = 0.339$, implying an absolute magnitude of $M_g = -21$. It was also detected by the VLA at 10 GHz on June 14 (Ho 2023b). It was classified as an LFBOT from its luminosity, fast evolution, and radio emission.

A.4. *AT2023vth/ZTF23ableqsp*

ZTF first detected AT2023vth on October 18, 2023 (MJD = 60235.116; Fremling 2023c). It had a fast rise of 1 mag day^{-1} , a fast fade of $0.25 \text{ mag day}^{-1}$, and blue colors with $g - r \approx -0.4 \text{ mag}$ (Sevilla et al. 2023), making it a promising LFBOT candidate. Optical spectroscopy taken on November 12 revealed narrow H α , [N II], and [S II] emission lines from the host galaxy at $z = 0.0747$, which implied an absolute magnitude of $M_g \approx -20$ (Ho et al. 2023a). The VLA detected radio emission at 10 GHz on November 17 (Ho 2023c) and NOEMA found millimeter emission at 100 GHz on November 20 (Ho & Bremer 2023). The presence of multiwavelength emission solidified the transient's LFBOT classification. We also obtained deep late-time VLT observations that will be reported in a separate paper (Wise et al., in prep.).

²⁸ PI Ho; Program ID GS-2022B-Q-126

²⁹ PI D. Perley; Program ID 22A-405

³⁰ PI A. Filippenko

A.5. AT2024qfm/ZTF24aaxhxhf

AT2024qfm was first detected by ZTF on July 24, 2024 (MJD = 60515.41; Forster et al. 2024). The most recent non-detection was 0.98 d prior at $g > 19.27$ mag. The source was detected again three nights later as part of the ZTF public survey, resulting in the first alert. Over the following two nights the source exhibited significant fading of 0.3 mag day^{-1} . SDSS pre-imaging showed a galaxy at the transient's position with photometric redshift $z = 0.190 \pm 0.054$, implying a high luminosity of $M < -20$ mag. The rapid fading, host-galaxy counterpart, and high luminosity led the transient to be flagged by the daily scanner on July 27.

The rapid fading flagged several fast-transient pipelines including Fastfinder (Fulton et al. 2024) and ZTFReST (Andreoni et al. 2021). The rapid fading was publicly reported by Fastfinder (Fulton et al. 2024). The transient itself was reported to the Transient Name Server (TNS³¹) by the Automatic Learning for the Rapid Classification of Events (ALeRCE) broker (Forster et al. 2024).

On August 1, a redshift of $z = 0.2270$ was determined by Gillanders et al. (2024) and an X-ray detection was reported by Margutti et al. (2024). On August 2, we obtained a long-slit spectrum of AT 2024qfm with GMOS on Gemini-North under a ToO program³² and confirmed the reported redshift. A VLA radio observation was also obtained³³, the radio data will be published as part of a separate paper (Nayana A. J. et al., in prep.). Finally, we obtained 100 GHz observations using NOEMA, which resulted in a detection. The fast optical light curve, and high luminosities at millimeter and X-ray wavelengths, all confirmed the LFBOT nature of this source. We also obtained deep late-time GTC/HIPERCAM observations that will be reported in a separate paper (Wise et al., in prep.).

A.6. AT2024aehp/ZTF24abygbss

AT2024aehp was first detected by ZTF on December 19, 2024 (MJD = 60663.36; Munoz-Arancibia et al. 2024). The most recent non-detection was 3 d prior. ZTF photometry over the next two nights revealed a fade rate of 0.2 mag day^{-1} , causing the transient to be flagged by the daily scanner on December 21. The fast fading and possible high peak luminosity from the photometric redshift of the host galaxy (SDSS $z_{\text{ph}} = 0.17 \pm 0.09$) motivated us to trigger follow-up observa-

tions. We acquired spectroscopy of the candidate using GMOS on Gemini South on December 23, 2024³⁴. The spectrum shows narrow H α , [N II], and [S II] emission lines that correspond to $z = 0.170$. We reported the rapid evolution and high luminosity (Sevilla et al. 2024).

Radio and X-ray observations initially resulted in non-detections, and the optical light curve flattened out in a way uncharacteristic of LFBOTs (Schroeder et al. 2025). A subsequent radio epoch at 86 days after peak light resulted in a detection and confirmation of a positive spectral index, suggesting a link with AT2018cow-like LFBOTs (Schroeder & Ho 2025). Then, another epoch at 141 days showed brightening in all radio bands by almost an order of magnitude, which is unprecedented compared to the radio emission of other LFBOTs. This paper focuses on the early observations of AT2024aehp, and the interesting late-time behavior will be examined in separate work.

B. DATA TABLES

In this section we provide tables of optical spectroscopy (Table 4), X-ray observations (Table 5), radio observations (Table 6), and host-galaxy photometry (Table 7). We also give our broken power-law fits to the radio SEDs (Table 8) and the resulting synchrotron parameters (Table 9). Finally, we list the optical photometry for each transient in Table 10.

³¹ <https://www.wis-tns.org/>

³² GN-2024B-Q-128; PI A. Ho

³³ Project ID VLA/23B-138; PI A. Ho

³⁴ GN-2024B-Q-128; PI A. Ho

Table 4. Optical Spectroscopy

Object	UTC Date	t_{obs} (days)	Redshift	Telescope/Inst.	Lines Detected
AT2022abfc	20221201	10	0.212	Gemini-S/GMOS	Ca H&K, Mg I
AT2023fhn	20230419	7	0.24	Gemini-S/GMOS	$\text{H}\alpha$, [N II]
AT2023fhn	20230420	8	0.24	P200/DBSP	$\text{H}\alpha$
AT2023fhn	20230426	14	0.24	Keck-I/LRIS	$\text{H}\alpha$, [N II], [S II]
AT2023hkw	20230512	12	0.339	Keck-II/DEIMOS	$\text{H}\alpha$, [N II]
AT2023vth	20231022	2	0.0747	P200/DBSP	$\text{H}\alpha$, [N II]
AT2023vth	20231112	23	0.0747	Gemini-N/GMOS	$\text{H}\alpha$, [N II], [S II]
AT2024qfm	20240802	6	0.227	Gemini-N/GMOS	$\text{H}\alpha$, [N II], [S II]
AT2024qfm	20240809	13	0.227	Keck-I/LRIS	[O II]
AT2024qfm	20240831	35	0.227	MMT/Binospec	$\text{H}\alpha$, $\text{H}\beta$, [O II], [O III], [N II], [S II]
AT2024qfm	20240902	37	0.227	Keck-I/LRIS	$\text{H}\alpha$, $\text{H}\beta$, [O II], [O III], [N II], [S II]
AT2024aehp	20241224	5	0.1715	Gemini-S/GMOS	$\text{H}\alpha$, $\text{H}\beta$, [O III], [N II], [S II]
AT2024aehp	20250101	13	0.1715	Keck-II/KCWI	$\text{H}\alpha$, $\text{H}\beta$, [O II], [O III], [N II], [S II]
AT2024aehp	20250107	19	0.1715	MMT/Binospec	$\text{H}\alpha$, $\text{H}\beta$, [O II], [O III], [N II], [S II]

Table 5. *Swift* XRT Observations

Object	UTC Date	t_{obs} (days)	Flux (10^{-13} erg cm $^{-2}$ s $^{-1}$)	Count Rate (10^{-3} s $^{-1}$)	n_{H} (10^{20} cm $^{-2}$)	L_{X} (10^{43} erg s $^{-1}$)	Photon Index
AT2022abfc	20221208	17	< 2	< 6	2.49	< 3	—
AT2023fhn	20230425	13	< 1.7	< 5	2.26	< 4	—
AT2023hkw	20230521	21	< 1.1	< 3.5	1.05	< 4.5	—
AT2023vth	20231110	21	< 1.9	< 3.4	22.6	< 0.23	—
AT2024qfm	20240801	5	5.0 ± 0.8	13 ± 2	3.83	8.2 ± 1.3	$2.1_{-0.5}^{+0.8}$
AT2024qfm	20240802	6	3.7 ± 0.9	10 ± 2	—	6.1 ± 1.5	$1.5_{-0.9}^{+1.6}$
AT2024qfm	20240803	7	< 4.9	< 12	—	< 7.9	—
AT2024qfm	20240803	7.5	$2.8_{-1.3}^{+1.8}$	7_{-3}^{+5}	—	$4.5_{-2.1}^{+2.9}$	$2.9_{-2.9}^{+3.3}$
AT2024qfm	20240805	9	< 3.1	< 8	—	< 5.0	—
AT2024qfm	20240807	11	25_{-14}^{+24}	63_{-35}^{+60}	—	40_{-23}^{+38}	— *
AT2024qfm	20240809	13	< 23	< 58	—	< 37	—
AT2024qfm	20240809	13.5	$2.0_{-0.9}^{+1.2}$	$5_{-2.4}^{+3.2}$	—	$3.3_{-1.4}^{+2.0}$	— *
AT2024qfm	20240810	14	$1.7_{-0.7}^{+1.0}$	$4_{-2.7}^{+1.9}$	—	$2.7_{-1.2}^{+1.6}$	$-0.3_{-1.8}^{+1.5}$
AT2024qfm	20240813	17	$2.6_{-1.1}^{+1.5}$	7_{-3}^{+4}	—	$4.2_{-1.9}^{+2.5}$	— *
AT2024qfm	20241204	130	< 0.9	< 2	—	< 1.5	—
AT2024aehp	20241231	12	< 2.3	< 6.2	2.83	< 2.0	—
AT2024aehp	20250103	15	< 3.0	< 7.9	—	< 2.6	—
AT2024aehp	20250105	17	< 2.4	< 6.3	—	< 2.1	—
CSS161010	20161103	24	$1.8_{-0.9}^{+1.4}$	$4.5_{-2.3}^{+3.4}$	4.7	$4.8_{-2.4}^{+3.6} \times 10^{-2}$	— *
CSS161010	20161108	29	< 1.2	< 2.9	—	$< 3.4 \times 10^{-2}$	—
CSS161010	20161111	32	< 2.0	< 5.0	—	$< 5.7 \times 10^{-2}$	—

NOTE—AT2022abfc values are from Ho et al. (2022a), AT2023fhn measurements obtained from Chrimes et al. (2024b), n_{H} for CSS161010 obtained from Coppejans et al. (2020). To convert flux to count rate, we assume a photon power-law index of $\Gamma = 2$ for all measurements. t is determined from the middle of the observation period. n_{H} is the same for all observations of a given object.

*Too few counts for a spectral index.

Table 6. Radio and Millimeter Observations

Name	UTC Date	t_{obs} (days)	Band	ν (GHz)	Config.	f_{ν} (μJy)
AT2022abfc	20221206	15	X	10	VLA-C	< 13
AT2022abfc	20221206	15	X	9	VLA-C	< 17
AT2022abfc	20221206	15	X	11	VLA-C	< 19
AT2022abfc	20221223	32	Ku	10	VLA-C	52 ± 3
AT2022abfc	20221223	32	X	10	VLA-C	38 ± 4
AT2022abfc	20230110	53	1	86	NOEMA-12A	< 348
AT2022abfc	20230405	135	Ku	10	VLA-B	45 ± 7
AT2022abfc	20230405	135	X	10	VLA-B	43 ± 9
AT2022abfc	20230601	192	3	0.45	GMRT	< 150
AT2022abfc	20230622	214	5	1.37	GMRT	44 ± 12
AT2022abfc	20230623	215	3	0.45	GMRT	< 165
AT2022abfc	20230624	216	Ku	10	VLA-BnA- >A	< 27
AT2022abfc	20230624	216	S	3	VLA-BnA- >A	< 26
AT2022abfc	20230624	216	X	10	VLA-BnA- >A	< 26
AT2022abfc	20240202	438	X	10	VLA-C	< 12
AT2022abfc	20240202	438	X	9	VLA-C	< 17
AT2022abfc	20240202	438	X	11	VLA-C	< 19
AT2023fhn	20230422	10	1	86	NOEMA-C	< 90
AT2023fhn	20230511	29	X	9	VLA-B	< 19
AT2023fhn	20230511	29	X	11	VLA-B	< 20
AT2023fhn	20230615	64	X	9	VLA-BnA	43 ± 6
AT2023fhn	20230615	64	X	11	VLA-BnA	53 ± 7
AT2023fhn	20230709	88	Ku	10	VLA-A	75 ± 7
AT2023fhn	20230709	88	X	10	VLA-A	118 ± 6
AT2023fhn	20230825	135	Ku	10	VLA-A	98 ± 9
AT2023fhn	20230825	135	X	10	VLA-A	143 ± 7
AT2023fhn	20230910	151	4	0.65	GMRT	< 300
AT2023fhn	20230910	151	5	1.37	GMRT	< 180
AT2023fhn	20231026	197	5	1.37	GMRT	85 ± 24
AT2023fhn	20231103	205	4	0.65	GMRT	< 231
AT2023fhn	20231127	229	4	0.65	GMRT	< 210
AT2023fhn	20231127	229	5	1.37	GMRT	112 ± 20
AT2023fhn	20240624	440	X	10	VLA-B	33 ± 5
AT2023hkw	20230614	44	X	9	VLA-BnA	79 ± 6
AT2023hkw	20230614	44	X	11	VLA-BnA	103 ± 7
AT2023hkw	20230704	64	Ka	33	VLA-A	124 ± 11
AT2023hkw	20230704	64	Ku	10	VLA-A	152 ± 7
AT2023hkw	20230826	117	C	6	VLA-A	74 ± 7
AT2023hkw	20230826	117	X	10	VLA-A	85 ± 8
AT2023hkw	20230826	117	Ku	10	VLA-A	56 ± 9
AT2023hkw	20230831	122	4	0.65	GMRT	< 100
AT2023hkw	20230831	122	5	1.37	GMRT	< 100
AT2023hkw	20230902	124	3	0.45	GMRT	< 210
AT2023hkw	20231028	180	5	1.37	GMRT	< 270
AT2023hkw	20231102	185	4	0.65	GMRT	< 780

Table 6 *continued*

Table 6 (*continued*)

Name	UTC Date	t_{obs} (days)	Band	ν (GHz)	Config.	f_{ν} (μJy)
AT2023hkw	20231103	186	3	0.45	GMRT	< 570
AT2023hkw	20231127	210	4	0.65	GMRT	< 360
AT2023hkw	20231127	210	5	1.37	GMRT	< 120
AT2023vth	20231117	28	X	9	VLA-D	150 ± 8
AT2023vth	20231117	28	X	11	VLA-D	148 ± 7
AT2023vth	20231120	31	1	86	NOEMA-C	358 ± 48
AT2023vth	20231120	31	1	102	NOEMA-C	350 ± 56
AT2023vth	20231123	34	2	136	NOEMA-C	264 ± 38
AT2023vth	20231123	34	2	152	NOEMA-C	241 ± 46
AT2023vth	20231128	39	C	6	VLA-D	259 ± 10
AT2023vth	20231128	39	Ka	33	VLA-D	368 ± 10
AT2023vth	20231128	39	Ku	10	VLA-D	473 ± 5
AT2023vth	20231128	39	X	10	VLA-D	399 ± 7
AT2023vth	20231203	44	1	86	NOEMA-10an	395 ± 40
AT2023vth	20231203	44	1	102	NOEMA-10an	349 ± 42
AT2023vth	20231203	44	2	102	NOEMA-10an	294 ± 41
AT2023vth	20231203	44	2	151.74	NOEMA-10an	241 ± 45
AT2023vth	20231216	57	4	0.65	GMRT	< 297
AT2023vth	20231216	57	5	1.37	GMRT	72 ± 24
AT2023vth	20231228	69	1	86	NOEMA-C	359 ± 34
AT2023vth	20231228	69	1	102	NOEMA-C	257 ± 38
AT2023vth	20231228	69	2	102	NOEMA-C	226 ± 24
AT2023vth	20231228	69	2	151.74	NOEMA-C	147 ± 28
AT2023vth	20240111	83	3	216	NOEMA-12C ant	N/A
AT2023vth	20240111	83	3	232	NOEMA-12C ant	N/A
AT2023vth	20240113	85	C	6	VLA-D	989 ± 9
AT2023vth	20240113	85	Ka	33	VLA-D	571 ± 10
AT2023vth	20240113	85	Ku	10	VLA-D	1290 ± 6
AT2023vth	20240113	85	X	10	VLA-D	1290 ± 6
AT2023vth	20240113	85	3	216	NOEMA-12C ant	75 ± 26
AT2023vth	20240113	85	3	232	NOEMA-12C ant	95 ± 30
AT2023vth	20240120	92	4	0.65	GMRT	< 420
AT2023vth	20240122	94	5	1.37	GMRT	109 ± 20
AT2023vth	20240130	102	1	86	NOEMA	249 ± 21
AT2023vth	20240130	102	1	102	NOEMA	215 ± 21
AT2023vth	20240213	116	C	6	VLA-C	903 ± 9
AT2023vth	20240213	116	Ka	33	VLA-C	295 ± 9
AT2023vth	20240213	116	Ku	10	VLA-C	562 ± 10
AT2023vth	20240213	116	X	10	VLA-C	769 ± 9
AT2023vth	20240222	125	4	0.65	GMRT	< 450
AT2023vth	20240224	127	5	1.37	GMRT	190 ± 24
AT2023vth	20240509	202	C	6	VLA-B	79 ± 10
AT2023vth	20240509	202	Ka	33	VLA-B	< 36
AT2023vth	20240509	202	Ku	10	VLA-B	46 ± 10
AT2023vth	20240509	202	X	10	VLA-B	56 ± 11
AT2024qfm	20240802	6	X	10	VLA-A	< 15
AT2024qfm	20240805	9	1	94	NOEMA	88 ± 22

Table 6 *continued*

Table 6 (*continued*)

Name	UTC Date	t_{obs} (days)	Band	ν (GHz)	Config.	f_{ν} (μJy)
AT2024qfm	20240812	16	1	94	NOEMA	147 ± 33
AT2024qfm	20240826	30	1	94	NOEMA	117 ± 21
AT2024qfm	20240920	55	1	94	NOEMA	< 60
AT2024aehp	20241227	8	X	10	VLA-A	< 12
AT2024aehp	20250311	82	X	10	VLA-D	26 ± 8
AT2024aehp	20250315	86	C	6	VLA-D	31 ± 9
AT2024aehp	20250315	86	X	10	VLA-D	36 ± 5
AT2024aehp	20250315	86	Ku	15	VLA-D	75 ± 6
AT2024aehp	20250509	141	C	6	VLA-D	161 ± 7
AT2024aehp	20250509	141	X	10	VLA-D	321 ± 4
AT2024aehp	20250509	141	Ku	15	VLA-D	455 ± 6
AT2024aehp	20250517	149	—	15.5	AMI	639**
AT2024aehp	20250523	155	1	86	NOEMA	191 ± 25
AT2024aehp	20250523	155	1	102	NOEMA	175 ± 28

NOTE—All radio and millimeter observations of each LFBOT. Listed frequencies are in the observer frame. We require $\text{SNR} > 3$ for a detection. Otherwise, we list the 3σ upper limits for a non-detection.

*This measurement was binned together with a GMRT Band-5 observation on June 1.

**This measurement was obtained from [Shoval et al. \(2025\)](#) and did not report a flux error or RMS.

Table 7. Host-Galaxy Photometry

Object	GALEX		Legacy/Pan-STARRS				NEOWISE		
	FUV	NUV	<i>g</i>	<i>r</i>	<i>i</i>	<i>z</i>	<i>w1</i>	<i>w2</i>	<i>w3</i>
AT2022abfc	—	21.550	19.057	18.124	17.698	17.464	17.356	17.568	15.875
AT2023fhn	—	20.913	19.452	18.912	18.606	18.566	18.796	18.755	—
AT2023hkw	—	21.898	20.706	19.669	—	18.996	18.833	19.097	—
AT2023vth	—	21.601	19.430	18.774	18.370	18.179	19.809	20.170	—
AT2024qfm	—	—	20.530	19.706	—	19.135	19.156	19.218	—
AT2024aehp	22.158	21.902	20.881	20.454	20.240	20.232	20.761	20.468	—

NOTE—Photometry used in our `prospector` host-galaxy fits. Empty columns represent non-detections or detections with $\text{SNR} < 5$. The middle columns represent photometry in the Legacy Survey *griz* filters, or the Pan-STARRS *griz* filters if the host galaxy was outside the SDSS footprint. Not listed is *HST* photometry for AT2023fhn from [Chrimes et al. \(2024a\)](#) that was also used in the fit.

Table 8. Radio SED Broken Power-law Fit Parameters

Object	Observer Frame Epoch (days)	Rest Frame Epoch (days)	ν_{obs} (GHz)	F_{obs} (μJy)	a_2
AT2023fhn	88–96	71–77	4.0 ± 0.3	232 ± 14	-0.69 ± 0.08
AT2023fhn	137–138	110–111	5.5 ± 0.3	387 ± 14	-0.87 ± 0.08
AT2023vth	86–87	80–81	8.5 ± 0.6	$(2.6 \pm 0.2) \times 10^3$	-1.06 ± 0.06
AT2023vth	104–129	97–120	2.7 ± 0.2	$(1.50 \pm 0.13) \times 10^3$	-0.55 ± 0.04
AT2024aehp	140–155	120–132	12.8 ± 1.1	$(7.8 \pm 0.9) \times 10^2$	-0.67 ± 0.09

NOTE—Results of a broken power-law fit (Equation 7). The values for the fitted peak frequency and flux density is measured in the observer’s frame.

Table 9. Inferred Parameters from Synchrotron Self-Absorption Modeling

Object	t_{rest} (days)	ν_p (rest) (GHz)	R (10^{16} cm)	B (G)	v/c	Energy (10^{48} erg)	n_e (10^3 cm $^{-3}$)	\dot{M} ($10^{-4} M_{\odot}$ /yr)	$m_p n_e R^3$ ($10^{-5} M_{\odot}$)
AT2022abfc	26	> 19	< 1.4	> 1.49	< 0.21	< 1.7	> 5.2	> 0.35	> 1.3
AT2023fhn	73	5.0 ± 0.4	13.0 ± 1.1	0.32 ± 0.03	0.57 ± 0.05	55 ± 6	0.022 ± 0.007	0.12 ± 0.02	4.1 ± 1.7
AT2023fhn	111	6.8 ± 0.4	12.0 ± 0.7	0.41 ± 0.02	0.38 ± 0.02	74 ± 5	0.10 ± 0.03	0.47 ± 0.06	15.2 ± 4.5
AT2023hkw	33	> 15	< 4.2	> 0.95	< 0.44	< 16	> 0.40	> 0.22	> 2.4
AT2023hkw	87	> 8.0	< 9.2	> 0.5	< 0.37	< 47	> 0.16	> 0.43	> 10.3
AT2023vth	81	9.1 ± 0.7	7.1 ± 0.6	0.58 ± 0.04	0.32 ± 0.03	31 ± 3	0.31 ± 0.09	0.49 ± 0.07	9.4 ± 3.6
AT2023vth	110	2.9 ± 0.2	17.6 ± 1.3	0.19 ± 0.01	0.53 ± 0.04	50 ± 6	0.010 ± 0.003	0.10 ± 0.01	4.7 ± 1.6
AT2024qfm	10	> 115	< 0.3	> 8.32	< 0.13	< 0.58	> 449	> 1.48	> 1.3
AT2024aehp	73	> 18	< 1.5	> 1.36	< 0.08	< 1.7	> 30	> 2.22	> 9.2
AT2024aehp	127	15.0 ± 1.3	5.5 ± 0.5	0.91 ± 0.08	0.16 ± 0.02	34 ± 5	3.1 ± 1.1	3.0 ± 0.5	44 ± 20

NOTE—The shock parameters we derive using Equations 2–6 for the various epochs of radio observations of each LFBOT. When we can only constrain the peak of the radio SED by observing one side of the broken-power law, we calculate limits on these parameters using the observation closest to where the peak would be. The right-most column is an estimate of the total mass swept up by the shock assuming a constant n_e .

Table 10. Optical Photometry

Object	UTC Time	t_{rest} (days)	Facility	Filter	mag
AT2022abfc	20221114 08:31	-6	P48/ZTF	<i>r</i>	> 19.68
AT2022abfc	20221114 10:40	-6	P48/ZTF	<i>g</i>	> 19.65
AT2022abfc	20221115 09:09	-5	P48/ZTF	<i>r</i>	> 20.40
AT2022abfc	20221115 10:08	-5	P48/ZTF	<i>g</i>	> 20.19
AT2022abfc	20221116 08:19	-4	P48/ZTF	<i>r</i>	> 19.36
AT2022abfc	20221117 08:01	-3	P48/ZTF	<i>g</i>	> 19.69
AT2022abfc	20221117 08:48	-3	P48/ZTF	<i>r</i>	> 19.53
AT2022abfc	20221118 08:04	-2	P48/ZTF	<i>g</i>	> 20.51
AT2022abfc	20221118 09:32	-2	P48/ZTF	<i>r</i>	> 20.13
AT2022abfc	20221119 09:34	-2	P48/ZTF	<i>g</i>	> 19.71
AT2022abfc	20221120 08:01	-1	P48/ZTF	<i>r</i>	> 20.35
AT2022abfc	20221121 08:15	0	P48/ZTF	<i>r</i>	19.46 ± 0.11
AT2022abfc	20221121 09:03	0	P48/ZTF	<i>g</i>	19.49 ± 0.14
AT2022abfc	20221125 08:32	3	P48/ZTF	<i>r</i>	19.55 ± 0.16
AT2022abfc	20221125 09:32	3	P48/ZTF	<i>g</i>	19.71 ± 0.20
AT2022abfc	20221127 07:32	5	P48/ZTF	<i>r</i>	20.32 ± 0.32
AT2022abfc	20221127 08:29	5	P48/ZTF	<i>g</i>	20.21 ± 0.19
AT2022abfc	20221201 09:15	8	P48/ZTF	<i>r</i>	> 20.23
AT2022abfc	20221210 07:04	16	P48/ZTF	<i>g</i>	> 19.60
AT2022abfc	20221211 07:03	16	P48/ZTF	<i>g</i>	> 19.85
AT2022abfc	20221217 06:01	21	P48/ZTF	<i>g</i>	> 20.35
AT2022abfc	20221217 07:03	21	P48/ZTF	<i>r</i>	> 20.19
AT2022abfc	20221220 06:11	24	P48/ZTF	<i>r</i>	> 19.21
AT2022abfc	20221220 07:03	24	P48/ZTF	<i>g</i>	> 19.66
AT2023fhn	20230408 06:00	-3	P48/ZTF	<i>i</i>	> 19.54
AT2023fhn	20230408 06:29	-3	P48/ZTF	<i>g</i>	> 18.76
AT2023fhn	20230408 07:12	-3	P48/ZTF	<i>r</i>	> 19.17
AT2023fhn	20230410 04:53	-2	P48/ZTF	<i>r</i>	19.68 ± 0.09
AT2023fhn	20230411 04:35	-1	P48/ZTF	<i>i</i>	19.65 ± 0.1
AT2023fhn	20230412 03:51	0	P48/ZTF	<i>r</i>	19.13 ± 0.05
AT2023fhn	20230412 04:35	0	P48/ZTF	<i>g</i>	18.69 ± 0.03
AT2023fhn	20230412 05:22	0	P48/ZTF	<i>g</i>	18.63 ± 0.03
AT2023fhn	20230412 05:27	0	P48/ZTF	<i>g</i>	18.72 ± 0.03
AT2023fhn	20230417 05:05	4	P48/ZTF	<i>g</i>	20.09 ± 0.09
AT2023fhn	20230417 05:49	4	P48/ZTF	<i>r</i>	20.72 ± 0.15
AT2023fhn	20230419 04:40	6	P60/SEDM	<i>g</i>	> 19.30
AT2023fhn	20230419 04:44	6	P60/SEDM	<i>r</i>	> 19.93
AT2023fhn	20230419 05:20	6	P48/ZTF	<i>r</i>	20.57 ± 0.22
AT2023fhn	20230421 03:50	7	P48/ZTF	<i>i</i>	> 20.32
AT2023fhn	20230421 05:04	7	P48/ZTF	<i>r</i>	21.24 ± 0.31
AT2023fhn	20230421 06:36	7	P48/ZTF	<i>g</i>	20.86 ± 0.32
AT2023fhn	20230423 03:51	9	P48/ZTF	<i>r</i>	> 20.96
AT2023fhn	20230423 05:02	9	P48/ZTF	<i>g</i>	> 21.07
AT2023fhn	20230424 00:39	10	LT/IO:O	<i>g</i>	21.52 ± 0.14
AT2023fhn	20230424 00:44	10	LT/IO:O	<i>r</i>	21.57 ± 0.20

Table 10 *continued*

Table 10 (*continued*)

Object	UTC Time	<i>t</i> _{rest} (days)	Facility	Filter	mag
AT2023fhn	20230424 03:52	10	P48/ZTF	<i>i</i>	> 20.24
AT2023fhn	20230425 04:07	10	P48/ZTF	<i>g</i>	> 20.76
AT2023fhn	20230425 04:36	10	P48/ZTF	<i>r</i>	> 20.52
AT2023fhn	20230427 04:00	12	P48/ZTF	<i>g</i>	> 20.66
AT2023fhn	20230427 04:47	12	P48/ZTF	<i>r</i>	> 20.58
AT2023fhn	20230501 07:59	15	P48/ZTF	<i>g</i>	> 19.08
AT2023fhn	20230509 04:26	22	P48/ZTF	<i>r</i>	> 20.85
AT2023hkw	20230423 03:54	-5	P48/ZTF	<i>r</i>	> 21.05
AT2023hkw	20230423 05:10	-5	P48/ZTF	<i>g</i>	> 21.16
AT2023hkw	20230423 05:46	-5	P48/ZTF	<i>i</i>	> 20.4
AT2023hkw	20230425 04:11	-4	P48/ZTF	<i>g</i>	> 20.97
AT2023hkw	20230425 04:51	-4	P48/ZTF	<i>r</i>	> 20.91
AT2023hkw	20230427 04:13	-2	P48/ZTF	<i>g</i>	> 20.84
AT2023hkw	20230427 04:43	-2	P48/ZTF	<i>r</i>	> 20.75
AT2023hkw	20230427 07:12	-2	P48/ZTF	<i>r</i>	> 20.67
AT2023hkw	20230427 09:17	-2	P48/ZTF	<i>i</i>	> 20.35
AT2023hkw	20230429 04:10	-1	P48/ZTF	<i>g</i>	20.64 ± 0.27
AT2023hkw	20230429 05:44	-1	P48/ZTF	<i>r</i>	20.94 ± 0.34
AT2023hkw	20230430 04:08	0	P48/ZTF	<i>g</i>	19.50 ± 0.19
AT2023hkw	20230430 04:19	0	P48/ZTF	<i>g</i>	19.57 ± 0.12
AT2023hkw	20230501 04:46	1	P48/ZTF	<i>r</i>	19.94 ± 0.16
AT2023hkw	20230501 07:42	1	P48/ZTF	<i>g</i>	19.71 ± 0.16
AT2023hkw	20230502 20:47	2	LT/IO:O	<i>r</i>	19.88 ± 0.25
AT2023hkw	20230502 20:50	2	LT/IO:O	<i>i</i>	20.16 ± 0.30
AT2023hkw	20230502 20:52	2	LT/IO:O	<i>z</i>	19.77 ± 0.38
AT2023hkw	20230503 08:09	2	P60/SEDM	<i>g</i>	> 19.06
AT2023hkw	20230503 14:26	3	GITCamera	<i>g</i>	20.36 ± 0.05
AT2023hkw	20230503 14:37	3	GITCamera	<i>r</i>	> 21.23
AT2023hkw	20230503 14:45	3	GITCamera	<i>i</i>	> 20.58
AT2023hkw	20230503 14:59	3	GITCamera	<i>z</i>	> 19.94
AT2023hkw	20230503 20:48	3	LT/IO:O	<i>g</i>	19.92 ± 0.23
AT2023hkw	20230503 20:51	3	LT/IO:O	<i>r</i>	> 19.75
AT2023hkw	20230503 20:54	3	LT/IO:O	<i>i</i>	19.38 ± 0.36
AT2023hkw	20230503 20:56	3	LT/IO:O	<i>z</i>	20.20 ± 0.38
AT2023hkw	20230509 06:15	7	P48/ZTF	<i>g</i>	> 20.77
AT2023hkw	20230509 07:58	7	P48/ZTF	<i>r</i>	> 20.27
AT2023hkw	20230510 20:54	8	LT/IO:O	<i>r</i>	21.05 ± 0.36
AT2023hkw	20230510 20:56	8	LT/IO:O	<i>i</i>	> 20.81
AT2023hkw	20230511 21:19	9	LT/IO:O	<i>g</i>	22.48 ± 0.31
AT2023hkw	20230511 21:23	9	LT/IO:O	<i>r</i>	> 22.14
AT2023hkw	20230511 21:23	9	LT/IO:O	<i>r</i>	> 22.00
AT2023hkw	20230511 21:26	9	LT/IO:O	<i>i</i>	22.38 ± 0.41
AT2023hkw	20230512 21:50	10	LT/IO:O	<i>g</i>	> 22.57
AT2023hkw	20230512 22:00	10	LT/IO:O	<i>r</i>	22.23 ± 0.25
AT2023hkw	20230512 22:11	10	LT/IO:O	<i>i</i>	> 22.22
AT2023hkw	20230513 04:13	10	P48/ZTF	<i>r</i>	> 20.96
AT2023hkw	20230513 06:54	10	P48/ZTF	<i>g</i>	> 20.90

Table 10 *continued*

Table 10 (*continued*)

Object	UTC Time	t_{rest} (days)	Facility	Filter	mag
AT2023hkw	20230513 21:17	10	LT/IO:O	<i>g</i>	22.47 ± 0.22
AT2023hkw	20230513 21:27	10	LT/IO:O	<i>r</i>	22.81 ± 0.32
AT2023hkw	20230513 21:37	10	LT/IO:O	<i>i</i>	22.68 ± 0.34
AT2023hkw	20230515 07:22	11	P48/ZTF	<i>r</i>	> 20.81
AT2023hkw	20230517 05:27	13	P48/ZTF	<i>g</i>	> 20.85
AT2023hkw	20230517 05:43	13	P48/ZTF	<i>r</i>	> 20.74
AT2023hkw	20230519 04:54	14	P48/ZTF	<i>g</i>	> 21.20
AT2023hkw	20230521 05:20	16	P48/ZTF	<i>g</i>	> 21.11
AT2023hkw	20230525 04:20	19	P48/ZTF	<i>i</i>	> 20.18
AT2023hkw	20230528 05:55	21	P48/ZTF	<i>g</i>	> 20.50
AT2023hkw	20230528 06:05	21	P48/ZTF	<i>g</i>	> 20.49
AT2023hkw	20230528 06:08	21	P48/ZTF	<i>g</i>	> 20.61
AT2023hkw	20230528 06:26	21	P48/ZTF	<i>r</i>	> 20.51
AT2023hkw	20230528 06:39	21	P48/ZTF	<i>r</i>	> 20.63
AT2023hkw	20230528 06:42	21	P48/ZTF	<i>r</i>	> 20.62
AT2023hkw	20230530 05:20	22	P48/ZTF	<i>i</i>	> 20.21
AT2023hkw	20230602 05:18	25	P48/ZTF	<i>r</i>	> 20.12
AT2023hkw	20230604 05:19	26	P48/ZTF	<i>g</i>	> 19.58
AT2023hkw	20230604 05:46	26	P48/ZTF	<i>r</i>	> 19.98
AT2023vth	20231014 02:54	-6	P48/ZTF	<i>g</i>	> 20.12
AT2023vth	20231014 03:06	-6	P48/ZTF	<i>r</i>	> 20.15
AT2023vth	20231014 03:26	-6	P48/ZTF	<i>r</i>	> 20.33
AT2023vth	20231016 03:05	-4	P48/ZTF	<i>r</i>	19.58 ± 0.23
AT2023vth	20231016 03:22	-4	P48/ZTF	<i>r</i>	> 19.91
AT2023vth	20231018 02:46	-2	P48/ZTF	<i>r</i>	17.38 ± 0.02
AT2023vth	20231020 03:08	0	P48/ZTF	<i>g</i>	16.84 ± 0.02
AT2023vth	20231020 03:37	0	P48/ZTF	<i>r</i>	17.15 ± 0.02
AT2023vth	20231022 02:28	2	P60/SEDM	<i>r</i>	> 16.78
AT2023vth	20231022 02:51	2	P48/ZTF	<i>r</i>	17.32 ± 0.06
AT2023vth	20231022 03:38	2	P48/ZTF	<i>g</i>	17.03 ± 0.03
AT2023vth	20231025 03:14	5	P48/ZTF	<i>g</i>	17.55 ± 0.05
AT2023vth	20231025 03:37	5	P48/ZTF	<i>g</i>	> 19.21
AT2023vth	20231028 02:46	7	P48/ZTF	<i>g</i>	> 19.04
AT2023vth	20231028 03:44	7	P48/ZTF	<i>r</i>	> 19.10
AT2023vth	20231101 02:09	11	P48/ZTF	<i>r</i>	19.36 ± 0.22
AT2023vth	20231101 02:15	11	P48/ZTF	<i>r</i>	19.36 ± 0.23
AT2023vth	20231101 02:21	11	P48/ZTF	<i>r</i>	19.39 ± 0.31
AT2023vth	20231101 02:26	11	P48/ZTF	<i>r</i>	19.15 ± 0.17
AT2023vth	20231101 02:32	11	P48/ZTF	<i>r</i>	19.40 ± 0.27
AT2023vth	20231101 02:44	11	P48/ZTF	<i>g</i>	> 19.52
AT2023vth	20231101 02:45	11	P48/ZTF	<i>g</i>	19.60 ± 0.33
AT2023vth	20231101 03:45	11	P48/ZTF	<i>r</i>	> 17.88
AT2023vth	20231102 02:11	12	P48/ZTF	<i>r</i>	19.76 ± 0.25
AT2023vth	20231102 02:17	12	P48/ZTF	<i>r</i>	19.62 ± 0.22
AT2023vth	20231102 02:23	12	P48/ZTF	<i>r</i>	19.70 ± 0.22
AT2023vth	20231102 02:28	12	P48/ZTF	<i>r</i>	19.53 ± 0.21
AT2023vth	20231102 02:34	12	P48/ZTF	<i>r</i>	19.40 ± 0.20

Table 10 *continued*

Table 10 (*continued*)

Object	UTC Time	t_{rest} (days)	Facility	Filter	mag
AT2023vth	20231103 02:10	13	P48/ZTF	<i>r</i>	19.77 ± 0.21
AT2023vth	20231103 02:16	13	P48/ZTF	<i>r</i>	> 19.94
AT2023vth	20231103 02:22	13	P48/ZTF	<i>r</i>	> 19.65
AT2023vth	20231103 02:27	13	P48/ZTF	<i>r</i>	19.97 ± 0.34
AT2023vth	20231103 02:33	13	P48/ZTF	<i>r</i>	19.61 ± 0.25
AT2023vth	20231103 03:13	13	P48/ZTF	<i>g</i>	> 19.48
AT2023vth	20231104 02:09	14	P48/ZTF	<i>r</i>	20.13 ± 0.31
AT2023vth	20231104 02:15	14	P48/ZTF	<i>r</i>	19.99 ± 0.25
AT2023vth	20231104 02:21	14	P48/ZTF	<i>r</i>	> 19.78
AT2023vth	20231104 02:27	14	P48/ZTF	<i>r</i>	19.57 ± 0.19
AT2023vth	20231104 02:32	14	P48/ZTF	<i>r</i>	19.69 ± 0.20
AT2023vth	20231105 02:09	15	P48/ZTF	<i>r</i>	19.98 ± 0.32
AT2023vth	20231105 02:14	15	P48/ZTF	<i>r</i>	20.12 ± 0.28
AT2023vth	20231105 02:20	15	P48/ZTF	<i>r</i>	19.98 ± 0.26
AT2023vth	20231105 02:26	15	P48/ZTF	<i>r</i>	19.95 ± 0.26
AT2023vth	20231105 02:32	15	P48/ZTF	<i>r</i>	19.92 ± 0.33
AT2023vth	20231105 02:45	15	P48/ZTF	<i>g</i>	> 19.53
AT2023vth	20231105 03:08	15	P48/ZTF	<i>r</i>	> 19.80
AT2023vth	20231106 02:09	16	P48/ZTF	<i>r</i>	> 20.01
AT2023vth	20231106 02:14	16	P48/ZTF	<i>r</i>	20.30 ± 0.31
AT2023vth	20231106 02:20	16	P48/ZTF	<i>r</i>	20.25 ± 0.27
AT2023vth	20231106 02:26	16	P48/ZTF	<i>r</i>	20.19 ± 0.28
AT2023vth	20231106 02:31	16	P48/ZTF	<i>r</i>	20.17 ± 0.29
AT2023vth	20231107 02:05	17	P48/ZTF	<i>r</i>	> 20.14
AT2023vth	20231107 02:08	17	P48/ZTF	<i>r</i>	> 20.01
AT2023vth	20231107 02:11	17	P48/ZTF	<i>r</i>	> 19.92
AT2023vth	20231107 02:14	17	P48/ZTF	<i>r</i>	> 19.91
AT2023vth	20231107 02:16	17	P48/ZTF	<i>r</i>	> 20.08
AT2023vth	20231107 02:20	17	P48/ZTF	<i>r</i>	> 19.93
AT2023vth	20231107 02:22	17	P48/ZTF	<i>r</i>	> 20.19
AT2023vth	20231107 02:25	17	P48/ZTF	<i>r</i>	19.91 ± 0.25
AT2023vth	20231107 02:27	17	P48/ZTF	<i>r</i>	> 20.16
AT2023vth	20231107 02:31	17	P48/ZTF	<i>r</i>	> 19.91
AT2023vth	20231107 03:11	17	P48/ZTF	<i>r</i>	> 19.71
AT2023vth	20231107 19:36	17	LT/IO:O	<i>g</i>	> 19.91
AT2023vth	20231107 19:41	17	LT/IO:O	<i>r</i>	> 19.86
AT2023vth	20231109 01:59	19	P60/SEDM	<i>g</i>	> 15.52
AT2023vth	20231109 02:07	19	P60/SEDM	<i>i</i>	> 15.54
AT2023vth	20231110 01:59	19	P60/SEDM	<i>g</i>	> 15.22
AT2023vth	20231110 02:03	19	P60/SEDM	<i>r</i>	> 18.69
AT2023vth	20231110 02:07	20	P60/SEDM	<i>i</i>	> 15.05
AT2024qfm	20240722 07:45	-4	P48/ZTF	<i>r</i>	> 19.63
AT2024qfm	20240722 09:35	-4	P48/ZTF	<i>g</i>	> 19.70
AT2024qfm	20240724 09:51	-2	P48/ZTF	<i>r</i>	19.45 ± 0.22
AT2024qfm	20240724 10:36	-2	P48/ZTF	<i>g</i>	19.32 ± 0.25
AT2024qfm	20240727 08:18	0	P48/ZTF	<i>r</i>	19.29 ± 0.1
AT2024qfm	20240727 09:37	0	P48/ZTF	<i>g</i>	19.31 ± 0.09

Table 10 *continued*

Table 10 (*continued*)

Object	UTC Time	t_{rest} (days)	Facility	Filter	mag
AT2024qfm	20240729 08:24	2	P48/ZTF	<i>g</i>	20.12 ± 0.15
AT2024qfm	20240729 09:21	2	P48/ZTF	<i>r</i>	19.98 ± 0.09
AT2024qfm	20240730 00:32	2	LT/IO:O	<i>g</i>	20.22 ± 0.10
AT2024qfm	20240730 00:34	2	LT/IO:O	<i>r</i>	20.32 ± 0.08
AT2024qfm	20240730 00:37	2	LT/IO:O	<i>i</i>	20.53 ± 0.09
AT2024qfm	20240731 00:33	3	LT/IO:O	<i>g</i>	20.65 ± 0.11
AT2024qfm	20240731 00:35	3	LT/IO:O	<i>r</i>	20.74 ± 0.1
AT2024qfm	20240731 00:37	3	LT/IO:O	<i>i</i>	20.60 ± 0.09
AT2024qfm	20240731 00:45	3	LT/IO:O	<i>i</i>	20.66 ± 0.08
AT2024qfm	20240731 00:47	3	LT/IO:O	<i>r</i>	21.00 ± 0.11
AT2024qfm	20240731 10:08	3	P48/ZTF	<i>g</i>	20.51 ± 0.15
AT2024qfm	20240803 08:24	6	P48/ZTF	<i>g</i>	> 20.78
AT2024qfm	20240805 07:37	7	P48/ZTF	<i>g</i>	21.33 ± 0.36
AT2024qfm	20240808 00:01	9	NOT/ALFOSC	<i>g</i>	22.04 ± 0.06
AT2024qfm	20240808 00:24	10	NOT/ALFOSC	<i>r</i>	21.98 ± 0.06
AT2024qfm	20240808 00:46	10	NOT/ALFOSC	<i>i</i>	22.35 ± 0.04
AT2024qfm	20240809 08:26	11	P48/ZTF	<i>g</i>	> 20.89
AT2024qfm	20240810 05:27	11	SOAR/GHTS	<i>g</i>	22.23 ± 0.04
AT2024qfm	20240810 05:55	11	SOAR/GHTS	<i>r</i>	22.61 ± 0.07
AT2024qfm	20240810 06:25	11	SOAR/GHTS	<i>i</i>	22.38 ± 0.16
AT2024qfm	20240810 07:26	11	P48/ZTF	<i>g</i>	> 21.07
AT2024qfm	20240811 04:35	12	Magellan/IMACS	<i>g</i>	22.73 ± 0.08
AT2024qfm	20240811 04:38	12	Magellan/IMACS	<i>g</i>	22.64 ± 0.07
AT2024qfm	20240811 04:42	12	Magellan/IMACS	<i>g</i>	22.51 ± 0.07
AT2024qfm	20240811 04:49	12	Magellan/IMACS	<i>g</i>	22.45 ± 0.07
AT2024qfm	20240811 05:00	12	Magellan/IMACS	<i>g</i>	22.58 ± 0.07
AT2024qfm	20240811 05:12	12	Magellan/IMACS	<i>r</i>	22.75 ± 0.11
AT2024qfm	20240811 05:24	12	Magellan/IMACS	<i>r</i>	22.41 ± 0.10
AT2024qfm	20240811 05:39	12	Magellan/IMACS	<i>i</i>	22.90 ± 0.08
AT2024qfm	20240811 05:51	12	Magellan/IMACS	<i>i</i>	23.15 ± 0.10
AT2024qfm	20240811 07:25	12	P48/ZTF	<i>g</i>	> 20.36
AT2024qfm	20240812 07:56	13	P48/ZTF	<i>r</i>	> 20.61
AT2024qfm	20240813 04:09	14	Magellan/IMACS	<i>g</i>	22.85 ± 0.07
AT2024qfm	20240813 04:21	14	Magellan/IMACS	<i>g</i>	22.99 ± 0.08
AT2024qfm	20240814 08:07	15	P48/ZTF	<i>g</i>	> 20.92
AT2024qfm	20240814 09:05	15	P48/ZTF	<i>r</i>	> 20.76
AT2024qfm	20240816 08:35	16	P48/ZTF	<i>g</i>	> 20.47
AT2024qfm	20240816 09:55	16	P48/ZTF	<i>r</i>	> 20.95
AT2024qfm	20240822 08:10	21	P48/ZTF	<i>r</i>	> 19.82
AT2024qfm	20240822 09:04	21	P48/ZTF	<i>g</i>	> 19.60
AT2024qfm	20240823 07:10	22	P48/ZTF	<i>i</i>	> 19.81
AT2024qfm	20240825 03:41	23	NOT/ALFOSC	<i>g</i>	> 23.81
AT2024qfm	20240825 04:03	23	NOT/ALFOSC	<i>r</i>	> 23.91
AT2024qfm	20240825 04:26	24	NOT/ALFOSC	<i>i</i>	> 24.06
AT2024qfm	20240825 07:57	24	P48/ZTF	<i>g</i>	> 20.51
AT2024qfm	20240827 07:54	25	P48/ZTF	<i>g</i>	> 20.87
AT2024qfm	20240829 07:37	27	P48/ZTF	<i>g</i>	> 21.13

Table 10 *continued*

Table 10 (*continued*)

Object	UTC Time	t_{rest} (days)	Facility	Filter	mag
AT2024qfm	20240831 05:55	28	SOAR/GHTS	<i>g</i>	> 24.07
AT2024qfm	20240831 06:08	28	SOAR/GHTS	<i>r</i>	> 23.98
AT2024qfm	20240831 07:20	28	P48/ZTF	<i>g</i>	> 20.89
AT2024qfm	20240901 07:08	29	P48/ZTF	<i>g</i>	> 20.78
AT2024qfm	20240902 07:12	30	P48/ZTF	<i>g</i>	> 21.08
AT2024qfm	20240903 09:50	31	P48/ZTF	<i>g</i>	> 20.94
AT2024qfm	20240903 09:51	31	P48/ZTF	<i>g</i>	> 20.95
AT2024qfm	20240905 06:56	33	P48/ZTF	<i>g</i>	> 21.00
AT2024qfm	20240907 08:06	34	P48/ZTF	<i>r</i>	> 20.65
AT2024qfm	20240908 05:01	35	Magellan/IMACS	<i>r</i>	25.06 ± 0.20
AT2024qfm	20240909 07:06	36	P48/ZTF	<i>g</i>	> 20.51
AT2024qfm	20240911 06:36	37	P48/ZTF	<i>g</i>	> 20.69
AT2024qfm	20240911 07:36	37	P48/ZTF	<i>r</i>	> 20.84
AT2024qfm	20240913 08:08	39	P48/ZTF	<i>g</i>	> 20.34
AT2024qfm	20240913 08:58	39	P48/ZTF	<i>r</i>	> 20.52
AT2024qfm	20240916 06:15	41	P48/ZTF	<i>g</i>	> 19.58
AT2024qfm	20240916 07:39	42	P48/ZTF	<i>r</i>	> 19.95
AT2024qfm	20240919 05:38	44	P48/ZTF	<i>i</i>	> 19.36
AT2024qfm	20240919 07:05	44	P48/ZTF	<i>r</i>	> 19.82
AT2024qfm	20240922 06:41	46	P48/ZTF	<i>g</i>	> 20.31
AT2024qfm	20240923 06:10	47	P48/ZTF	<i>g</i>	> 20.65
AT2024qfm	20240924 08:55	48	P48/ZTF	<i>g</i>	> 20.33
AT2024qfm	20240925 09:30	49	P48/ZTF	<i>g</i>	> 20.43
AT2024qfm	20240926 08:12	50	P48/ZTF	<i>i</i>	> 19.95
AT2024aehp	20241215 10:10	-3	P48/ZTF	<i>r</i>	> 19.23
AT2024aehp	20241215 10:12	-3	P48/ZTF	<i>r</i>	> 19.09
AT2024aehp	20241219 08:34	0	P48/ZTF	<i>r</i>	19.59 ± 0.16
AT2024aehp	20241219 10:02	0	P48/ZTF	<i>g</i>	19.02 ± 0.09
AT2024aehp	20241219 11:39	0	P48/ZTF	<i>i</i>	19.31 ± 0.17
AT2024aehp	20241220 08:47	1	P48/ZTF	<i>g</i>	19.23 ± 0.07
AT2024aehp	20241220 09:09	1	P48/ZTF	<i>r</i>	19.46 ± 0.08
AT2024aehp	20241221 07:50	2	P48/ZTF	<i>i</i>	19.60 ± 0.14
AT2024aehp	20241221 09:08	2	P48/ZTF	<i>g</i>	19.52 ± 0.10
AT2024aehp	20241221 11:41	2	P48/ZTF	<i>r</i>	20.26 ± 0.25
AT2024aehp	20241222 09:02	3	P48/ZTF	<i>i</i>	> 18.97
AT2024aehp	20241222 09:44	3	P48/ZTF	<i>g</i>	19.73 ± 0.08
AT2024aehp	20241222 11:45	3	P48/ZTF	<i>r</i>	19.61 ± 0.15
AT2024aehp	20241223 11:31	3	P48/ZTF	<i>r</i>	20.05 ± 0.17
AT2024aehp	20241224 08:26	4	P48/ZTF	<i>r</i>	20.03 ± 0.13
AT2024aehp	20241224 09:38	4	P48/ZTF	<i>g</i>	19.98 ± 0.13
AT2024aehp	20241227 09:04	7	P48/ZTF	<i>r</i>	20.03 ± 0.13
AT2024aehp	20241227 09:40	7	P48/ZTF	<i>i</i>	> 18.68
AT2024aehp	20241227 11:08	7	P48/ZTF	<i>g</i>	> 20.22
AT2024aehp	20241229 10:32	9	P48/ZTF	<i>g</i>	19.83 ± 0.08
AT2024aehp	20241229 11:10	9	P48/ZTF	<i>r</i>	20.07 ± 0.11
AT2024aehp	20241229 12:34	9	P48/ZTF	<i>i</i>	20.07 ± 0.29
AT2024aehp	20241231 01:51	10	SWIFT/UVOT	<i>uvw2</i>	> 21.02

Table 10 *continued*

Table 10 (*continued*)

Object	UTC Time	t_{rest} (days)	Facility	Filter	mag
AT2024aehp	20241231 09:41	10	P60/SEDM	<i>g</i>	19.95 ± 0.08
AT2024aehp	20241231 09:47	10	P60/SEDM	<i>r</i>	20.09 ± 0.06
AT2024aehp	20241231 09:54	10	P60/SEDM	<i>i</i>	20.20 ± 0.08
AT2024aehp	20241231 10:28	10	P48/ZTF	<i>g</i>	19.94 ± 0.10
AT2024aehp	20241231 11:54	10	SWIFT/UVOT	<i>uvw1</i>	20.67 ± 0.21
AT2024aehp	20241231 11:56	10	SWIFT/UVOT	<i>u</i>	20.21 ± 0.29
AT2024aehp	20241231 11:57	10	SWIFT/UVOT	<i>b</i>	> 19.15
AT2024aehp	20241231 12:00	10	SWIFT/UVOT	<i>uvw2</i>	21.13 ± 0.19
AT2024aehp	20241231 12:06	10	SWIFT/UVOT	<i>uvm2</i>	21.01 ± 0.23
AT2024aehp	20250101 06:46	11	P60/SEDM	<i>g</i>	19.98 ± 0.06
AT2024aehp	20250101 06:53	11	P60/SEDM	<i>r</i>	20.23 ± 0.08
AT2024aehp	20250101 06:59	11	P60/SEDM	<i>i</i>	20.26 ± 0.08
AT2024aehp	20250101 07:46	11	P48/ZTF	<i>i</i>	20.37 ± 0.29
AT2024aehp	20250101 07:58	11	P48/ZTF	<i>i</i>	20.00 ± 0.18
AT2024aehp	20250101 08:07	11	P48/ZTF	<i>g</i>	20.33 ± 0.2
AT2024aehp	20250102 04:49	12	P60/SEDM	<i>g</i>	20.16 ± 0.09
AT2024aehp	20250102 04:56	12	P60/SEDM	<i>r</i>	20.18 ± 0.08
AT2024aehp	20250102 05:02	12	P60/SEDM	<i>i</i>	20.22 ± 0.11
AT2024aehp	20250102 23:44	12	LT/IO:O	<i>u</i>	20.47 ± 0.23
AT2024aehp	20250102 23:48	12	LT/IO:O	<i>g</i>	20.21 ± 0.05
AT2024aehp	20250102 23:52	12	LT/IO:O	<i>r</i>	20.31 ± 0.06
AT2024aehp	20250102 23:57	12	LT/IO:O	<i>i</i>	> 19.83
AT2024aehp	20250103 00:01	12	LT/IO:O	<i>z</i>	20.91 ± 0.19
AT2024aehp	20250103 05:08	13	P48/ZTF	<i>g</i>	20.05 ± 0.22
AT2024aehp	20250103 05:26	13	P48/ZTF	<i>g</i>	> 19.50
AT2024aehp	20250104 09:13	14	P48/ZTF	<i>i</i>	20.14 ± 0.27
AT2024aehp	20250105 05:52	14	P48/ZTF	<i>r</i>	> 18.62
AT2024aehp	20250105 07:49	14	P48/ZTF	<i>g</i>	20.73 ± 0.28
AT2024aehp	20250105 07:50	14	P48/ZTF	<i>g</i>	20.13 ± 0.13
AT2024aehp	20250106 07:40	15	Deveny/LMI	<i>r</i>	20.34 ± 0.09
AT2024aehp	20250106 07:48	15	Deveny/LMI	<i>g</i>	20.23 ± 0.12
AT2024aehp	20250106 07:56	15	Deveny/LMI	<i>i</i>	20.32 ± 0.09
AT2024aehp	20250106 22:04	16	LT/IO:O	<i>u</i>	> 19.34
AT2024aehp	20250106 22:09	16	LT/IO:O	<i>g</i>	20.69 ± 0.17
AT2024aehp	20250106 22:13	16	LT/IO:O	<i>r</i>	20.39 ± 0.19
AT2024aehp	20250106 22:17	16	LT/IO:O	<i>i</i>	> 20.67
AT2024aehp	20250106 22:21	16	LT/IO:O	<i>z</i>	> 20.03
AT2024aehp	20250106 22:21	16	LT/IO:O	<i>z</i>	> 19.84
AT2024aehp	20250107 09:22	16	P48/ZTF	<i>i</i>	> 20.13
AT2024aehp	20250107 09:28	16	P48/ZTF	<i>i</i>	19.95 ± 0.33
AT2024aehp	20250107 22:16	17	LT/IO:O	<i>u</i>	> 18.72
AT2024aehp	20250107 22:16	17	LT/IO:O	<i>u</i>	> 17.96
AT2024aehp	20250107 22:21	17	LT/IO:O	<i>g</i>	> 20.12
AT2024aehp	20250107 22:25	17	LT/IO:O	<i>r</i>	20.63 ± 0.24
AT2024aehp	20250107 22:29	17	LT/IO:O	<i>i</i>	20.52 ± 0.26
AT2024aehp	20250107 22:33	17	LT/IO:O	<i>z</i>	> 20.57
AT2024aehp	20250108 08:10	17	P48/ZTF	<i>r</i>	> 17.81

Table 10 *continued*

Table 10 (*continued*)

Object	UTC Time	t_{rest} (days)	Facility	Filter	mag
AT2024aehp	20250108 22:33	18	LT/IO:O	<i>u</i>	> 20.25
AT2024aehp	20250108 22:37	18	LT/IO:O	<i>g</i>	20.45 ± 0.26
AT2024aehp	20250108 22:42	18	LT/IO:O	<i>r</i>	20.61 ± 0.15
AT2024aehp	20250108 22:46	18	LT/IO:O	<i>i</i>	20.66 ± 0.13
AT2024aehp	20250108 22:50	18	LT/IO:O	<i>z</i>	> 21.33
AT2024aehp	20250109 07:02	18	P48/ZTF	<i>g</i>	> 20.27
AT2024aehp	20250109 07:36	18	P48/ZTF	<i>r</i>	> 20.51
AT2024aehp	20250111 06:38	20	P48/ZTF	<i>g</i>	> 19.16
AT2024aehp	20250111 06:38	20	P48/ZTF	<i>g</i>	> 19.27
AT2024aehp	20250111 08:36	20	P48/ZTF	<i>r</i>	> 20.15
AT2024aehp	20250111 09:07	20	P48/ZTF	<i>i</i>	> 19.88
AT2024aehp	20250111 09:39	20	P48/ZTF	<i>r</i>	> 19.90
AT2024aehp	20250113 05:19	21	P48/ZTF	<i>r</i>	> 19.16
AT2024aehp	20250116 06:49	24	P48/ZTF	<i>g</i>	> 19.50
AT2024aehp	20250116 06:50	24	P48/ZTF	<i>g</i>	> 19.66
AT2024aehp	20250116 07:13	24	P48/ZTF	<i>r</i>	> 19.46
AT2024aehp	20250116 09:11	24	P48/ZTF	<i>r</i>	> 19.94
AT2024aehp	20250118 06:11	25	P48/ZTF	<i>g</i>	> 20.12
AT2024aehp	20250118 06:11	25	P48/ZTF	<i>g</i>	20.52 ± 0.27
AT2024aehp	20250118 08:05	26	P48/ZTF	<i>i</i>	> 20.53
AT2024aehp	20250118 08:09	26	P48/ZTF	<i>i</i>	> 20.56
AT2024aehp	20250118 08:37	26	P48/ZTF	<i>r</i>	20.96 ± 0.29
AT2024aehp	20250118 08:38	26	P48/ZTF	<i>r</i>	> 20.64
AT2024aehp	20250120 06:07	27	P48/ZTF	<i>g</i>	21.38 ± 0.33
AT2024aehp	20250120 06:28	27	P48/ZTF	<i>g</i>	20.97 ± 0.23
AT2024aehp	20250120 07:10	27	P48/ZTF	<i>r</i>	> 20.72
AT2024aehp	20250120 07:11	27	P48/ZTF	<i>r</i>	20.86 ± 0.25
AT2024aehp	20250123 05:20	30	P48/ZTF	<i>g</i>	> 20.14
AT2024aehp	20250123 05:23	30	P48/ZTF	<i>g</i>	> 20.65
AT2024aehp	20250123 05:49	30	P48/ZTF	<i>r</i>	> 20.85
AT2024aehp	20250123 05:52	30	P48/ZTF	<i>r</i>	> 20.72
AT2024aehp	20250130 07:08	36	P48/ZTF	<i>r</i>	21.24 ± 0.36
AT2024aehp	20250203 04:39	39	P48/ZTF	<i>r</i>	20.98 ± 0.23
AT2024aehp	20250204 04:46	40	P48/ZTF	<i>r</i>	21.05 ± 0.26
AT2024aehp	20250218 06:11	52	P48/ZTF	<i>r</i>	21.48 ± 0.24
AT2024aehp	20250218 06:35	52	P48/ZTF	<i>g</i>	22.14 ± 0.25
AT2024aehp	20250219 05:40	53	P48/ZTF	<i>r</i>	20.98 ± 0.26
AT2024aehp	20250223 06:10	56	P48/ZTF	<i>r</i>	21.15 ± 0.28
AT2024aehp	20250325 07:26	82	P48/ZTF	<i>r</i>	20.89 ± 0.28
AT2024aehp	20250514 21:25	125	LT/IO:O	<i>g</i>	> 21.61
AT2024aehp	20250514 21:36	125	LT/IO:O	<i>r</i>	> 21.69
AT2024aehp	20250520 05:14	130	P60/SEDM	<i>g</i>	> 21.61
AT2024aehp	20250520 05:14	130	P60/SEDM	<i>g</i>	> 21.29
AT2024aehp	20250520 05:21	130	P60/SEDM	<i>r</i>	> 20.50
AT2024aehp	20250520 05:21	130	P60/SEDM	<i>r</i>	> 21.23
AT2024aehp	20250521 03:47	130	Deveny/LMI	<i>r</i>	21.86 ± 0.12
AT2024aehp	20250521 03:50	130	Deveny/LMI	<i>i</i>	21.58 ± 0.11

Table 10 *continued*

Table 10 (*continued*)

Object	UTC Time	t_{rest} (days)	Facility	Filter	mag
--------	----------	--------------------------	----------	--------	-----

NOTE—Photometry for all six LFBOTs obtained from Fritz marshal. We omit all observations prior to six days before t_0 and all ZTF non-detections more than fifty days after t_0 . For non-detections, we provide 3σ upper limits.